



DIGITAL ACCESS TO SCHOLARSHIP AT HARVARD

Novel technologies for high-throughput and high-content studies on zebrafish larvae

The Harvard community has made this article openly available.
[Please share](#) how this access benefits you. Your story matters.

| | |
|--------------|--|
| Citation | Pardo, Carlos. 2013. Novel technologies for high-throughput and high-content studies on zebrafish larvae. Doctoral dissertation, Harvard University. |
| Accessed | April 17, 2018 4:17:36 PM EDT |
| Citable Link | http://nrs.harvard.edu/urn-3:HUL.InstRepos:11156677 |
| Terms of Use | This article was downloaded from Harvard University's DASH repository, and is made available under the terms and conditions applicable to Other Posted Material, as set forth at http://nrs.harvard.edu/urn-3:HUL.InstRepos:dash.current.terms-of-use#LAA |

(Article begins on next page)

© 2013 – *Carlos Pardo*
All rights reserved.

*Novel technologies for high-throughput and high-content studies on zebrafish larvae***Abstract**

The zebrafish larva is an ideal candidate for *in vivo* high-throughput screening: it is a small vertebrate, it is optically transparent, possesses complex organs, and is easy to culture. In addition, genetic mutants and models of human diseases are widely available. Despite these attractive features there are no tools capable of screening at sufficient throughput and resolution to fully exploit the zebrafish. Here, I present a collection of technologies that enable high-throughput studies on zebrafish larvae at cellular resolution.

I first present a microfluidic-based platform, *VAST*, that is capable of loading individual zebrafish larvae into a thin-walled capillary and positioning it under the field-of-view of a microscope. Loading is achieved through fluidic-tubing, valves, and computerized syringe-pumps. Positioning of the larvae is automated by detecting their passage through the capillary with a custom-made photodetector-based device and a robust feedback mechanism between *VAST*'s imaging system and syringe-pumps. Enclosing the zebrafish in a capillary allows for high-NA, short working-distance objectives that permit cellular imaging. Two stepper-motors rotate the capillary allowing the larvae to be imaged from any angle. Larvae are automatically oriented by comparing live images acquired from multiple angles of rotation with reference templates of larvae orientated dorsally and laterally. *VAST* allows screening cycles of 9.6 seconds, improving previous manual throughputs by two orders of magnitude.

We next demonstrate an improved optical projection tomography (OPT) system that images zebrafish larvae at high-speed video frame-rates while rotating them 360 degrees. Algorithms are used to improve the image-quality by correcting for non-uniform illumination, non-rectilinear ray-paths, capillary vibrations, movements of the sample, and non-axial capillary rotation. These corrections allow us to simplify our OPT system and acquire 3D volumes of an entire larva in 2.5 seconds, two orders of magnitude faster than previously described OPT systems.

Lastly, we developed algorithms to extract hundreds of morphometric measurements from 3D reconstructions of the craniofacial skeleton of 5 days-old larvae. By segmenting each bone and quantifying their morphological features, we create hyperdimensional phenotypic signatures that exhaustively describe the craniofacial morphology. By performing hierarchical clustering analysis on these we are able to classify teratogen compounds by their chemical class.

Table of Contents

| | | |
|-------|--|----|
| 1 | Introduction | 1 |
| 1.1 | Summary | 1 |
| 1.2 | Background..... | 2 |
| 1.2.1 | Drug Discovery | 2 |
| 1.2.2 | The Zebrafish Larvae..... | 6 |
| 1.3 | General Problem..... | 10 |
| 1.3.1 | Low throughput | 11 |
| 1.3.2 | Low content | 12 |
| 1.4 | Specific Research Goals | 12 |
| 1.5 | Organization of the dissertation | 14 |
| 2 | Technologies for manipulating and imaging zebrafish larvae | 17 |
| 2.1 | Technologies for phenotypic screening of zebrafish inside microtiter plates | 17 |
| 2.2 | Technologies for phenotypic screening outside microtiter plates..... | 18 |
| 2.3 | Flow cytometry..... | 19 |
| 2.4 | Use of capillaries for phenotyping and husbandry | 19 |
| 2.4.1 | Microfluidics for zebrafish embryo culture | 20 |
| 2.5 | Rapid injection of zebrafish embryos..... | 20 |
| 2.6 | Optical manipulation of zebrafish | 21 |
| 2.6.1 | Laser ablation | 21 |
| 2.6.2 | Spatially- and temporally-controlled in vivo release of chemicals and oligonucleotides by photouncaging in zebrafish..... | 23 |

| | | |
|-------|---|----|
| 2.6.3 | Photo-labeling with photoconvertible proteins | 23 |
| 2.7 | Technologies for the imaging of zebrafish larvae | 24 |
| 2.7.1 | Confocal imaging systems..... | 25 |
| 2.7.2 | Two-photon microscopy..... | 26 |
| 2.7.3 | Light-sheet microscopy for high-speed imaging of zebrafish | 27 |
| 2.7.4 | Whole animal blood-flow imaging | 28 |
| 2.7.5 | Measuring neural activity using calcium imaging | 29 |
| 2.7.6 | Label-free nonlinear microscopy | 30 |
| 3 | A novel high-throughput in vivo vertebrate screening platform for zebrafish larvae..... | 31 |
| 3.1 | Introduction | 31 |
| 3.2 | Results | 33 |
| 3.2.1 | Description of the Vertebrate Automated Screening Technology | 33 |
| 3.2.2 | Proof-of-concept screen: axon misguidance by point mutations in the robo2 gene . | 34 |
| 3.2.3 | Laser ablation of single neuron fibers..... | 35 |
| 3.2.4 | Timings for each screening step..... | 37 |
| 3.2.5 | Health Assessment..... | 37 |
| 3.3 | Methods | 39 |
| 3.3.1 | Components of the high-throughput screening platform | 39 |
| 3.3.2 | Components of the imaging system | 39 |
| 3.3.3 | Animals | 40 |
| 3.3.4 | Axon guidance screen | 40 |
| 3.3.5 | Laser axotomy | 40 |
| 3.3.6 | Assessment of animal health..... | 41 |

| | | |
|-------|---|----|
| 3.3.7 | System architecture and operation: | 42 |
| 3.4 | Discussion and Summary | 46 |
| 4 | Improved and fully automated vertebrate screening platform with parallel animal processing | 47 |
| 4.1 | Introduction | 47 |
| 4.2 | Results | 48 |
| 4.2.1 | Multi-thread Vertebrate Automated Screening Technology | 48 |
| 4.2.2 | Multi-thread Operation | 50 |
| 4.2.3 | Fluorescence/bright-field automated zebrafish discriminator | 51 |
| 4.2.4 | Automated identification of zebrafish orientation and position | 52 |
| 4.2.5 | Analysis of capillary materials for high- quality imaging | 55 |
| 4.3 | Methods | 57 |
| 4.4 | Discussion and Summary | 58 |
| 5 | A novel rapid optical projection tomography system for hyperdimensional in vivo phenotyping | 59 |
| 5.1 | Introduction | 59 |
| 5.2 | Results | 60 |
| 5.2.1 | High-throughput optical projection tomography | 60 |
| 5.2.2 | Assessment of craniofacial abnormalities | 66 |
| 5.2.3 | Hyperdimensional in vivo phenotyping | 71 |
| 5.3 | Methods | 77 |
| 5.3.1 | Sample handling and image acquisition | 78 |
| 5.3.2 | Tomographic reconstruction | 78 |
| 5.3.3 | Image segmentation and bone identification | 79 |

| | | |
|--------|---|-----|
| 5.3.4 | Maintenance of fish, embryo collection, and staging of larvae | 80 |
| 5.3.5 | Cartilage staining | 80 |
| 5.3.6 | Assay design and chemical treatment | 81 |
| 5.3.7 | Test chemicals | 81 |
| 5.3.8 | Timings | 81 |
| 5.3.9 | Statistics | 82 |
| 5.3.10 | Components of the system | 82 |
| 5.3.11 | Image alignment | 82 |
| 5.3.12 | Image artifact corrections | 85 |
| 5.3.13 | Light ray simulation | 87 |
| 5.3.14 | Software | 87 |
| 5.4 | Discussion and Summary | 87 |
| 6 | Conclusion | 90 |
| 6.1 | Summary | 90 |
| 6.2 | Concluding remarks | 92 |
| 7 | Appendix A – Protocol for the construction of a femtosecond laser microsurgery system | 93 |
| 7.1 | Introduction | 93 |
| 7.2 | Materials | 94 |
| 7.2.1 | Reagents | 94 |
| 7.2.2 | Equipment | 95 |
| 7.3 | Procedure | 99 |
| 7.3.1 | Laser Safety Section | 99 |
| 7.3.2 | Setting up the optical table, laser, power meter, microscope, and optical isolator:.. | 101 |

| | | |
|-------|---|-----|
| 7.3.3 | Installing the equipment to control the laser power: | 102 |
| 7.3.4 | Assembly of the dichroic mounting adapter:..... | 104 |
| 7.3.5 | Assembly of the periscope..... | 106 |
| 7.3.6 | Assembly of the laser beam expander: | 107 |
| 7.3.7 | Coarse alignment of the laser..... | 110 |
| 7.3.8 | Fine alignment of the laser and image focal planes | 113 |
| 7.3.9 | Laser axotomy on in-vivo and in-vitro samples | 115 |
| 7.4 | Anticipated results | 117 |
| 7.4.1 | Characterization of the femtosecond laser surgery system | 117 |
| 7.4.2 | Femtosecond axotomy of <i>C. elegans</i> mechanosensory neurons | 117 |
| 7.5 | Timings | 119 |
| 8 | Acknowledgements | 121 |
| 8.1 | Advising | 121 |
| 8.2 | Research Funding | 121 |
| 8.3 | Graduate Funding..... | 121 |
| 8.4 | Zebrafish Husbandry and Lines..... | 121 |
| 8.5 | Other Authors Contributions | 122 |
| | References | 123 |

Table of Figures

| | |
|--|----|
| Figure 1.1: Steps in common drug discovery pipelines. | 2 |
| Figure 1.2: Number of citations containing “zebrafish” in the PUBMED database. The zebrafish community has experienced an exponential growth since the ‘90s. Source: http://www.ncbi.nlm.nih.gov/pubmed - last access 03/07/2013 | 6 |
| Figure 1.3: Steps of a typical zebrafish screen. Embryos are collected from adults mating and dechorionated. In case of a drug or toxicity screen animals are treated with compounds. In knock-out or gain-of-function experiments larvae are microinjected with morpholinos or mRNA. At the experimental end-point animals are stained with an appropriate protocol. Animals are then prepared for imaging by fixing them in agarose gels. Animals are subsequently imaged using high-resolution microscopes. The images are analyzed for phenotyping or scoring for predefined read-outs. After all data is collected it is analyzed to validate or refute the screen hypothesis. Red blocks represent the current rate-limiting steps and the target steps for the technologies presented in this dissertation. | 13 |
| Figure 2.1: Schematic representation of an automated injection system of zebrafish eggs. The zebrafish embryo is captured in an agar mold. A micro-pipette with a micro-force measurement system is optically guided into the embryo. The force measurement system is used to detect the puncture of the pipette of both the chorion and cell membrane. Punctures are identified by a sharp peak in the force profile as represented in the force-time graph. ... | 21 |
| Figure 2.2: Schematic representation of light-sheet microscopy. The sample is illuminated from the side and imaged from an orthogonal plane. A thin plane of fluorescence excitation is achieved by a cylindrical lens, which prevents out-of-focus excitation and emission. | 27 |
| Figure 3.1: Schematic of zebrafish manipulation and imaging platform. Larvae are automatically loaded to the system from either reservoirs or multiwell plates. Reservoirs are connected to the system via fluidic valves and a bubble mixer prevents the larvae from settling. The multiwell plate is located on a motorized x–y stage, which positions individual wells below larva-loading (red arrow) and water-supply (blue arrow) tubes, both held by a silicone rubber block. The block seals the well surfaces as a piston moves the tubes into the wells. A photodetection system including two LEDs and one high-speed photodiode (PD) discriminates the passage of a larva from air bubbles and debris. Two stepper motors hold a capillary along its axis of rotation; this assembly is mounted on a three-axis position stage (not shown) and held between an upright microscope for confocal imaging and an inverted microscope for brightfield imaging. A multifocal confocal head with a cooled electron-multiplying charge-coupled device (CCD) camera and a second large-area CCD connected to the upright port are used for high-speed confocal and widefield fluorescence imaging. A high-speed CCD camera connected to the inverted port allows rapid brightfield detection and positioning of larvae. A femtosecond laser beam used for microsurgery is directed to the upper beam path by a dichroic filter and focused on the sample through the objective. | 32 |
| Figure 3.2: Flow diagram for chemical and genetic screens. (a) Genetic screen: Mutagenized animals are loaded from a reservoir to the imaging platform. After imaging, the mutants are sorted into multiwell plates by phenotype. (b) Chemical screen: Animals are loaded from a reservoir to the imaging platform, which can be used either to count the number of animals and/or to perform optical manipulations such as laser microsurgery. The animals are then dispensed into multiwell plates containing chemicals to be tested. After incubation within chemicals, the animals are loaded back into the imaging platform to check phenotypes. ... | 34 |
| Figure 3.3: Orientation, imaging and screening of zebrafish larvae. (a) Schematic showing the midline crossing of Mauthner axons (left) and confocal images of GFP-expressing Mauthner cells at 0° and 15° (right). Magnified versions of boxed areas are shown to the right of each | |

image. (b) Widefield fluorescence images illustrating the phenotypes distinguished in a small-scale test screen. Representative images showing GFP-labeled axons of retinal ganglion neurons projecting to the optic tectum in larvae of the indicated genotypes. Arrows point to the misguided projections. Scale bars, 150 μ m (50 μ m in magnified images in a). . 35

Figure 3.4: Laser microsurgery and neuronal regeneration. (a) Widefield fluorescence images of enhanced GFP (EGFP)-expressing lateral-neuron axon fibers in a 3-d.p.f. larva are shown at the indicated times before and after axotomy. Scale bar, 75 μ m. (b) Distributions of laser cut sizes (n=30). 36

Figure 3.5: Quantitative assessment of zebrafish health. (a) Survival and abnormality of larvae as a function of initial flow rate (n = 150 for each rate). (b) Appearance time of swim bladder in screened and control fish (one way ANOVA, p = 0.94, average of three independent experiments with 50 fish analyzed in each; error bars, s.d.; n = 3). 38

Figure 3.6: Representative images of zebrafish larvae with wild-type ($ast^{+/+}$) versus astray ($ast^{+/a}$) phenotype. Genotypically homozygous $ast^{-/-}$ and $ast^{+/a}$ fish were crossed to generate the $ast^{+/a}$ larvae shown. 42

Figure 3.7: Flowchart showing the algorithm for the operation sequence of the system. See supplementary text for further details. 45

Figure 4.1: Multi-thread Vertebrate Automated Screening Technology (VAST). The platform consists of three subsystems that operate simultaneously: loading, imaging, and unloading. Larvae are automatically loaded to the platform from individual wells of a mesh-filter multiwell plate positioned by a motorized x-y stage. The mesh-filter insert allows easy transfer of larvae into the system. In order to avoid a drop in the fluid level (while larva is being aspirated by the loading nozzle), a circulator is set nearby the loading nozzle (inset A) that consists of a fluid source and an aspirator where the tip of the aspirator is slightly elevated than the tip of the fluid source. A zebrafish discriminator with a brightfield and a fluorescence photodetection system (inset B) discriminates the passage of fluorescent larvae from non-fluorescent ones, air bubbles and debris. Two step motors hold a capillary immersed in a water bath along its axis of rotation; this assembly is mounted on a three-axis position stage (not shown) and held between an upright microscope and an inverted microscope. A multifocal confocal head with a cooled electron-multiplying charge-coupled device (EM-CCD) camera and a second large-area charge-coupled device (CCD) are used for high-speed confocal and wide-field fluorescence imaging, respectively. A high-speed CCD camera connected to the inverted microscope allows rapid bright-field imaging for positioning and orienting the larvae. 49

Figure 4.2: Timings of multi-thread processing of zebrafish. Blue, red, and green bars indicate the processes comprising loading, imaging, and unloading, respectively. (a) The time required for each handling step (n = 192). Multiwell plate loading process includes positioning the multiwell plate and the nozzle, and aspirating a larva into the tube from the multiwell plate. Transportation time is the duration it takes to move a larva within the fluidic tube from one point to another. (b) Multi-thread operation: The system simultaneously performs loading, imaging, and unloading operations with three different larvae. As a result, the overall processing time is dictated solely by the duration of the slowest process (i.e. imaging; 9.6 sec), not by the total duration of all processes. 51

Figure 4.3: Zebrafish discriminator. (a) Schematic representation of the zebrafish discriminator. The system is composed of a bright-field discrimination system and a fluorescence-activated zebrafish sorter. (b) Schematic representation of the mechanism of action of the bright-field discrimination system. By combining both the refracted/scattered and transmitted signals the system distinguishes a zebrafish larva from air bubbles and debris. (c) Detection and discrimination reliabilities at increasing flow rates. The reliability is near 100 % at normal operating speeds of 330 μ L/s. (n=150). 52

Figure 4.4: Identification of the angle and position of larvae. (a) Dorsally and ventrally oriented larvae. Red arrows indicate the dominant morphological features for distinguishing dorsally

vs. ventrally views. It is too difficult to reliably determine the larva's orientation based solely on comparisons with dorsal and ventral reference images. (b) The larva is rotated along its longitudinal axis through a full 360° and snapshots are acquired at two degree increments at 180 frames per second. (c) The system then correlates the images with a library of prerecorded dorsal and lateral images from stage-matched control larvae (inset). The blue and red curves in the radar chart are results of the image correlations with the dorsal and lateral templates. The blue, green, and red arrows indicate the orientations of maximum correlations with the dorsally, ventrally and laterally orientated templates, respectively. The reliability of the algorithm is 99 % (n=100 larvae) 55

Figure 4.5: Analysis of capillary materials for distortion-free low-background high-resolution imaging. (a) From left to right, the point-spread functions (PSF) with different materials/conditions; no capillary, PTFE capillary, FEP capillary, borosilicate glass capillary, and ultra-thin borosilicate glass capillary. The wall thicknesses of capillaries are 250 µm, 150 µm, 170 µm and 10 µm, respectively. The ultra-thin glass capillary produces the least image distortion. Scale bar is 1 µm. (b) Radial (blue) and axial (red) resolutions of candidate materials. PTFE was not included due to the significant non-Gaussian PSF it produces. (c) Autofluorescence analysis of candidate materials. PTFE and FEP capillaries cause significant autofluorescence. 57

Figure 5.1: High-throughput optical projection tomography. (a) Tomographic reconstruction of the craniofacial cartilage after image processing. Insets show details of the hypobranchial bone. The resolution of the 3D reconstruction is sufficient to distinguish bones with dimensions of ~10 µm and gaps of ~5 µm between bones. (b) Schematic representation of the OPT platform. A fluidic system composed of a pump, valves, and tubing is used to load larvae from multiwell plates into an glass capillary located within the FOV of a macrozoom microscope. The capillary is held at two ends by stepper motors with hollow shafts that sit on a position stage. Several dynamic image artifact correction steps are performed prior to reconstruction. (c) Non-uniformity of illumination due to the capillary walls is corrected. (d) The light path through the capillary is simulated and is fed to the reconstruction algorithm to correct for the refraction of light by the capillary. (e) Small movements of the larva along the capillary axis and radial vibrations of the capillary are detected and corrected. The box-plots quantify the wobbling of the capillary (top plot) and the motion of the larva along the capillary axis (bottom plot) prior to correction. (f) Identifying the center of rotation (COR) for reconstruction. Reconstructing a cross-section using different COR estimates allows us to identify the true rotation axis with micron precision. The bottom panels show reconstructions using two different CORs. The reconstruction on the left corresponds to a COR estimated solely from the boundaries of the capillary sidewalls. The reconstruction on the right has sharper boundaries and lower entropy, and is therefore selected as the best estimate for true COR. Graphs show 1D intensity profiles across the dashed lines. Entropy of each image is shown on the bottom right corner. (g) Each step of image artifact correction produces increasingly accurate tomographic reconstructions. Images show 3D reconstructions from 320 images of a 5 dpf zebrafish larvae stained with Alcian blue. Insets show zoomed views of the most posterior region of the basihyal cartilage (red). 62

Figure 5.2: Compensation for the refraction of light rays by the capillary walls. (a) The path of light rays (blue) passing through the capillary as modeled using the Snell laws. Solid red lines indicate the outer surface of the capillary, dashed red lines indicate the inner surface of the capillary. (b) To estimate which CCD pixels the outgoing rays will reach to, we back-project (green) the previously computed outgoing rays (blue) without undergoing refraction deviations until they reach a virtual image of the CCD on the focus plane (black). This eliminates the need to model the optical lens by assuming that it is focused on the center of the capillary. (c) Image segmentation of the hyosymplectic bones before and after compensating for the index of refraction mismatch. After correction, the fine details of the bones are visible in the reconstructions. 65

Figure 5.3: Quantification of complex skeletal phenotypes induced by teratogenic chemicals. (a) Three-dimensional reconstructions allow visualization of complex phenotypes. Images show

representative tomographic renderings of fully segmented craniofacial skeletons from 5 dpf larvae treated with three different teratogens: retinoid acid, cyclopamine, and flusilazole. Representative reconstructions are shown for all chemicals at low, medium, and high doses (relative to the calculated LC_{50}) from left to right. (b) Quantitative analysis of the ethmoidal plate (orange), trabeculae (pink), and Meckel's cartilage (blue) in larvae treated with increasing concentrations of cyclopamine. Phenotypes are concentration-dependent and not all bones are altered in the same manner or to the same degree. (c) Quantitative analysis of the trabeculae in larvae treated with increasing concentrations of all-trans-retinoic acid (atRA; blue), cyclopamine (orange), and flusilazole (red). (d) Ratiometric analysis of the relationship between the ethmoidal plate and the ceratohyal cartilage in larvae treated with increasing concentrations of all-trans-retinoic acid (atRA; blue), cyclopamine (orange), and flusilazole (red). Taken together, panels (b) through (d) show that individual metrics reveal distinct phenotypic changes in response to different chemicals and exhibit distinct dependencies on chemical concentrations. (e) Representative reconstructions of the samples used to generate the data points in (b-d). Bones colors match corresponding data points. For reconstructions of (c) and (d) green bones indicate untreated (WT) controls (n=4-6 for each treatment condition, n=53 for WT, \pm s.e.m). 70

Figure 5.4: Analysis on repeatability of reconstruction and segmentation. (a) Representative reconstruction and segmentations of a single untreated control larva loaded and imaged multiple times. (b) Bar plot showing normalized values for the ethmoidal volume, meckel's angle to the coronal plane, and meckel's length. Values are shown for different untreated control larvae (blue), a single untreated control larva loaded and imaged multiple times (red) and for larvae treated with 10 nM of all-trans-retinoid acid (green) (n=5 for each treatment condition, \pm s.e.d). 71

Figure 5.5: Independence of Phenotype Metrics Used. (a) Correlation matrix for metrics across all samples. Bones on which the metrics are based are indicated along the x- and y-axes. White indicates correlation coefficient values above 0.95. High correlations are primarily constrained to the main diagonal, indicating that most metrics behave in an uncorrelated manner. (b) Principal component analysis shows that each metric contributes non-redundant information to the phenotypic signatures. Plot shows the cumulative normalized contribution of each metric to the eigenvalues of the most significant principal components obtained through principal component analysis (red). Black dotted line indicates the cumulative sum if all metrics contributed equally. Green line shows the same analysis with random reordering of all metrics. The blue line shows the same analysis performed on white noise. The small inset shows the histogram of the correlation coefficients across metrics for all samples. These values are centered at a low correlation value of 0.3. 73

Figure 5.6: Hyperdimensional in vivo phenotyping. (a) Schematic representation of the analysis process. Following 3D reconstruction (left) Individual bones are segmented and separated by bone type (center). Morphological image analysis is then used to compute metrics for each bone segment (e.g. volume, length, angles, surface area, and location). These values are stored as a hyperdimensional phenotypic signature for each larva (right). (b) Phenotypic signature array (shown log 10 scale of p-values). Each row represents individual larvae treated with a compound. Measurements are color-coded to indicate a reduction (red) or an increase (green) with respect to untreated controls. Phenotype metrics and compound treated larvae are ordered by hierarchical clustering based on correlation. (c) Dendrogram computed on linkage by correlation of the mean standard score for chemicals applied beginning at 9 hpf. Teratogens known to cause developmental bone abnormalities are grouped based on similarities in their hyperdimensional phenotype signature. Retinol and the retinoids (red) and the triazole derivatives (green) cluster together in groups that are distinct from cyclopamine (a steroidal alkaloid). 75

Figure 5.7: Mechanism of action of the screened teratogen compounds. Compounds labeled in red are from the retinoids family, compounds in green are from the triazole-derivative class and Cyclopamine belongs to the steroidal-alkaloid family. 76

Figure 5.8: Compensation for wobbling of the ultrathin capillary and longitudinal movement of the larva. (a-b) Sinograms (i.e. single column (y-axis) of pixels obtained from the collection 2D images acquired at all angles through rotation (x-axis)) of 4 μm large beads attached to capillary walls. (a) Sinogram prior to correcting for wobbling of the ultrathin capillary. Black arrows point to angles at which the capillary experiences significant motion orthogonal to capillary axis. (b) Sinogram image after automatically correcting for wobbling. The large movements are compensated for and the capillary sidewalls remain stationary at all angles of rotation. (c) Five frames before and after compensating for the longitudinal sliding of the larva along the capillary axis (x-axis). Prior to artifact correction, the tip of the larva's head is not aligned across all images. Red dashed lines are straight reference lines that have been added to aid visualization of the corrections of the artifacts. 84

Figure 5.9: Image processing is used to estimate the true center of rotation (COR). Plot shows the measured entropy values for multiple images that have been reconstructed using COR estimates shifted from the original COR estimate (distances represent displacement from the original COR estimate located at $x=0$). Arrows indicate representative reconstructed images for various COR estimates. Images show single transverse slices through the larva using a filtered back-projection algorithm. The reconstruction at the bottom, corresponding to a COR at $-12.5 \mu\text{m}$ from the original estimate, has the lowest entropy and is therefore used as the true COR for the complete 3D reconstruction. 86

Figure 7.1: Optical system layout. List of components in Table 9. 100

Figure 7.2: An exploded view of the dichroic mounting adapter. The dichroic mounting adapter is composed of a metal filter cube (A), which contains an IR dichroic mirror (B). The filter cube is attached to a BA1 standard base (C) using glue. The opposite face of the BA1 standard base attaches to a 2-axis compact kinematic mount (D) also using glue. The compact kinematic mount is attached to a $\varnothing 1"$ ($1"$) pedestal pillar post (E) with a #8-32 x $1/4"$ set screw. The assembly comprising components A through E mounts to a Nikon adapter plate from a 70 mm stage-up kit (F) so that the dichroic mirror sits in the beam path. This is accomplished by drilling a hole (G) and using a #8-32 x $1/4"$ screw (H) to position the dichroic mirror over the opening in the adapter plate. The entire assembly is affixed to the microscope using screws (I) included in the 70 mm stage-up kit. Figure 7.1 shows the location of the dichroic mounting adapter on the microscope. 105

Figure 7.3: An exploded view of the beam expander. Lenses L1 and L2 (A and B, respectively) sit in their mounts which are attached to $\varnothing 1/2"$ posts. Two $\varnothing 1"$ irises (C) are also attached to $\varnothing 1/2"$ posts. All four posts sit securely in $\varnothing 1/2"$ post holders (D), one of which is attached to a single-axis stage with rotatable micrometer (E) and $\varnothing 1.5"$ post clamp adapter plate (F) while the remaining three are attached to rail carriers (G). These four assemblies firmly attach to the 12" optical rail (H) which is mounted to the two $\varnothing 1.5"$ posts via two $\varnothing 1.5"$ post mounting clamps (I). The entire assembly is mounted using BA2 standard bases. 108

Figure 7.4: Optical path for simultaneous epi-fluorescence imaging and laser axotomy. The femtosecond laser, indicated by the red line, passes through beam conditioning optics before being directed up by the NIR dichroic mirror into the back aperture of the objective lens. The epi-fluorescence excitation, indicated by the blue line, is simultaneously directed into the back aperture of the objective lens by the filter cube. The fluorescence emission, indicated by the green line, passes through multiple filters and is captured by the camera. 109

Figure 7.5: Use of the IR alignment tool. The IR alignment tool is composed of a RMS IR-aligning disk and a RMS 45 to CFI 60 objective adapter. Without lenses L1 and L2, the transmitted beam is directed to the center of the dichroic mirror resulting in a glowing spot on the field of the disk (a). Adjusting the dichroic mirror causes the transmitted beam to pass through the center hole and an additional spot caused by the reflection of the beam from the cover glass appears on the field of the disk (b). The reflected spot is caused by the non-normal incidence of the transmitted beam on the cover glass. Moving the transmitted spot half-way towards the initial location of the reflected spot by adjusting the upper periscope mirror and

then moving the transmitted spot back to the center hole by adjusting the angle of the dichroic mirror, achieves normal incidence of the beam on the cover glass. Normal incidence is indicated by both reflected and transmitted beams passing through the center (c). Inserting both lenses L1 and L2 into the beam path (Steps 68-70), results in a large, symmetric circular illumination on the IR alignment tool (d). 111

Figure 7.6: Ablated patterns in permanent marker on cover glass under different alignment conditions. When the image plane is focused on the boundary of the marked and unmarked glass surfaces (a), and when the system is properly-aligned, the resulting cutting pattern is narrow and symmetric, while the firing pattern is relatively small and also symmetric (b). If the beam is clipped and/or lenses L1 and L2 are misaligned, the cutting pattern is wider in one direction than the orthogonal direction. Additionally the firing pattern becomes asymmetric (c). If the laser is out of focus, the cutting pattern is blurred and the firing pattern is larger (d). Scale bar is 50 μm 115

Figure 7.7: Point spread function of the laser at the focal plane. The system described in this protocol generates a circular laser spot at the sample with a full-width-half-maximum of 1.7 μm 117

Figure 7.8: Femtosecond laser microsurgery. (a) A highly localized region (arrow) of a mechanosensory neuron is ablated using the system described in this protocol. (b) Following surgery at point 1, the ablated process first retracts to point 2, and then regenerates to point 3. Scale bar 10 μm 119

Table of Tables

| | |
|--|-----|
| Table 1: Costs and savings from the reduction in number of compounds for each stage of the drug discovery pipeline. Source: Leading pharmaceutical innovation, 2 nd ed..... | 5 |
| Table 2: Genetic techniques available to the zebrafish community. Modified from: (Tropepe and Sive 2003). | 10 |
| Table 3: Comparison of current manual screening characteristics and requirements for HTS. ... | 12 |
| Table 4: Average duration of screening steps for VAST. | 37 |
| Table 5: Timings for larva handling and image acquisition n=96 | 66 |
| Table 6: Chemicals and catalog numbers employed in teratogen screen | 67 |
| Table 7: Concentrations and LC ₅₀ for test chemicals | 68 |
| Table 8: Complete list of metrics employed for HIP in the teratogen screen. | 77 |
| Table 9: List of components as shown in Figure 7.1 | 101 |
| Table 10: Troubleshooting table for each step of the protocol for the construction of a femtosecond laser surgery system..... | 120 |

Table of Equations

| | |
|--|----|
| Equation 1: Centre of mass | 53 |
| Equation 2: Decision rule for animal orientation | 53 |
| Equation 3: Cross correlation of images to the reference template | 54 |
| Equation 4: Entropy of a gray scale image from the histogram of its intensity values | 86 |
| Equation 5: Snell laws | 87 |

There are many people without whom this work would not be possible. Firstly I wanted to thank and dedicate this thesis to my family, who has always given me the love and support to follow my academic dreams. Secondly I want to thank my advisor Dr. Yanik, and my mentors Dr. Ortiz-de-Solorzano, Dr. Eimon and Dr. Romero for their time, support, friendship and advice. I am also indebted to my co-authors over the years, especially Amin Allalou and Tsung-Yao Chang; thanks to their friendship and collaborations this document is complete. I want to thank my colleagues and friends from our research group for their help, support and friendship, and my friends and roommates from Windsor for always being there when needed.

1 Introduction

1.1 Summary

Large-scale screening of phenotypes induced by drugs, environmental toxicants, gene mutations, and other agents is essential for modern biology, medical research, and environmental risk assessment. Although cell-based assays are amenable to high-throughput screening (HTS), results often fail to correlate with animal models or clinical outcomes. Even the most sophisticated *in vitro* models cannot fully preserve the complexity of intact organs or accurately replicate *in vivo* processes such as organogenesis, disease pathology, and toxicity. To address these limitations, chemical screens are increasingly being conducted using zebrafish (*Danio rerio*), a small vertebrate model organism that has been extensively used in forward genetic screens and is amenable to high-throughput methodologies.

However, current handling of zebrafish as of this date either relies on manual and low throughput approaches that do not permit large scale studies, or on screening techniques typically present in *in vitro* screening, such as screening in microtiter plates, that does not permit taking full advantage of the complexity of the *in vivo* model. Moreover, to date, screens in zebrafish have typically relied on manual assessment of morphology and often ignored phenotypes not encompassed by more than a small number of pre-defined read-outs. Similarly, morphological phenotyping is often non-quantitative and limited to features only easily observable. Due to these constraints, phenotyping remains a subjective process that can vary greatly between labs and lacks the systematization and throughput required for HTS and high-content screening (HCS).

To fully realize the potential of both genetic and small molecule screens in zebrafish, we have here developed technologies capable of rapidly and quantitatively handling, imaging and phenotyping whole animals at unprecedented throughputs. We first demonstrate a novel high-throughput screening system capable of handling zebrafish larvae at unmatched speeds. We

then demonstrate an optical projection tomography system to rapid image the larvae in 3D. Lastly we present a novel analysis tool that extracts of hundreds of morphometric measurements from the 3D volumetric images through image segmentation and analysis.

1.2 Background

1.2.1 Drug Discovery

Historically, drugs were discovered through identifying the active ingredient from traditional remedies or by fortunate unplanned discoveries during many years. In modern science, drug discovery is performed in a more systematic way (Figure 1.1).

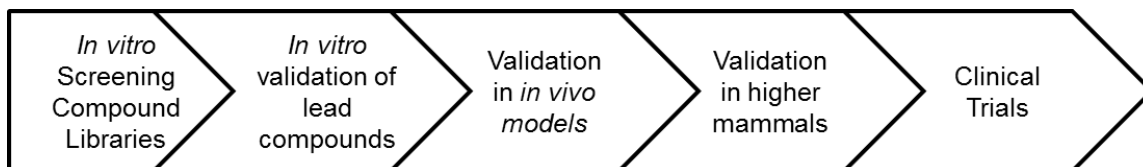


Figure 1.1: Steps in common drug discovery pipelines.

The first step in the drug discovery pipeline consists in the screening of a large library of compounds in simplified *in vitro* models. Libraries often include small molecules, natural products or extracts and are usually screened in intact cells to identify substances that have a desirable therapeutic effect. These libraries are compiled by renowned institutions like the *National Institute of Health* or the *Broad Institute of Harvard & MIT* and are frequently designed for specific assays (e.g. hormone receptor inhibitors). Since the sequencing of the human genome, which allowed rapid cloning and synthesis of large quantities of purified proteins, it has become more common to initially screen large compounds libraries against isolated biological targets which are hypothesized to be disease-modifying instead of against the more complete but more time consuming cell culture model.

The lead compounds arising from the initial screening steps are validated *in vitro* using similar or more complex models as those used in the initial drug screen. The compounds that endure this

step are then validated using *in vivo* models, commonly mice, before moving to more expensive, time-consuming bigger mammals and ultimately into clinical trials.

Advances in the initial drug screening have historically been centered in the development and refinement of high-throughput screening and high-content screening tools that increase the speed and complexity of these assays. More recently, with the rise in popularity of small model organisms, these are being incorporated into the early screening steps of the drug discovery pipeline. In the next paragraphs, I will succinctly introduce these techniques.

1.2.1.1 High-throughput screening

High-throughput screening (HTS) is a method for scientific experimentation especially used in drug discovery and toxicology assays in the initial screening step (Figure 1.1). It consist in taking a “brute force” approach to testing a large number of drugs by incorporating automation, using small volumes and operating with parallel platforms to rapidly increase screening throughput (i.e. the number of conditions tested per unit of time).

Using robotics, data processing algorithms, control software, liquid handling devices, and sensitive detectors, HTS allows researchers to quickly conduct thousands to millions of chemical, genetic and pharmacological tests in a reasonable amount of time (e.g. months). Through this process researchers can rapidly identify active compounds, antibodies or genes that modulate a pathway of interest. The results of these experiments provide starting points for drug design and for the understanding of the interaction or role of a particular biochemical process in biology before continuing the studies in more complex *in vitro* and *in vivo* models (Figure 1.1).

The key testing vessel for HTS is the microtiter plate. Initially based on a 12x8-well configuration, and now reaching conformations as dense as 72 x 48-well configurations, these plates handle small volumes of compounds in very defined and compact reservoirs that significantly simplify the robotic handling and imaging of the samples. Although HTS is based either on the interaction between large molecules and *in vitro* cell culture models, there are also groups that have studied *in vivo* models of small model organisms inside microtiter plates (see section 2.1 - Technologies

for phenotypic screening of zebrafish inside microtiter plates – page 17). However, HTS has largely relied on simplified models that result in simple read-outs that can accommodate the throughputs commonly present in HTS.

1.2.1.2 High-content screening

High-content screening (HCS) is a method that is used in biological research and drug discovery to identify compounds that alter the phenotype of a cell or sample through the analysis of multiple read-outs at high-resolution, typically single cell resolution in *in vitro* cell culture models (Abraham, Taylor et al. 2004).

HCS is frequently performed in microtiter plates and is typically part of a HTS study design. In a typical HCS study cells are first treated with compounds and after a period of time, structures and molecular components of these are analyzed by labeling proteins and structures of interest with fluorescent tags. Through the use of fluorescent markers with different absorption and emission spectra, it is possible to image each marker separately, thus allowing imaging several different cell components in parallel. Furthermore, through the use of high numerical aperture (NA) and high-magnification objectives, and ultra-thin glass bottom microtiter plates, it is possible to achieve high-resolution imaging while maintaining sufficient throughput and content. Thus, in a typical HCS design it is possible to detect phenotypes at a cellular and subcellular level. Therefore a large number of data points can be collected per cell, and complex and subtle features can be captured for analysis.

HCS is based on the combination of two techniques: image analysis for feature extraction and bioinformatics techniques for the interpretation of the large amounts of data usually recovered in HCS studies. Although these techniques have primarily come together in HCS for the study of *in vitro* cell culture models, similar techniques could be applied to more complex *in vivo* models where the ability to capture complex phenotypes is required to study these models in their complexity.

1.2.1.3 Small Model Organism

Up to recent years, the initial drug screening has been based on HTS and more recently on HCS of *in vitro* cell-culture models. Although cell-based assays are ideal for techniques such as HTS and HCS, results often fail to correlate with animal models or clinical outcomes. Even the most sophisticated *in vitro* models cannot fully preserve the complexity of intact organs or accurately replicate *in vivo* processes such as organogenesis, disease pathology, and toxicity.

The failure to replicate *in vivo* characteristics results in false negatives and false positives in the initial screening step. Compounds that are metabolized into active form by the liver, for instance, will appear as inactive in a simplified *in vitro* model and would present as a false negative. The presence of false negatives causes researchers to ignore compounds that could otherwise be lead candidates for subsequent studies. More commonly, simplified *in vitro* models result in false positives that result in high costs (see Table 1). For instance, compounds that do not cross the blood brain barrier or that are rapidly filtered and secreted by the kidneys can be identified as optimal lead compounds. These are then moved to animal models or preclinical trials incurring in elevated costs that could be eliminated by increasing the complexity of the models in the initial screening step.

Table 1: Costs and savings from the reduction in number of compounds for each stage of the drug discovery pipeline. Source: Leading pharmaceutical innovation, 2nd ed.

| Stage | Total Cost (\$M) | # of compounds reaching this stage (out of ~10,000) | Cost single compound (\$M) | Savings from preventing 10% of false positive compounds (\$M) |
|------------------------|------------------|---|----------------------------|---|
| Screening & Validation | 40 | 30 | 1 | 4 |
| Preclinical Trials I | 160 | 20 | 8 | 16 |
| Preclinical Trials II | 250 | 10 | 25 | 25 |
| Clinical Trials | 500 | ~5 | 100 | 50 |

The need to improve the complexity of the initial screen has prompted researchers to identify new models that are amenable to HTS and HCS. Small Model Organisms (SMO), such as the nematode *C. elegans*, the *Drosophila* or fruit fly, and the zebrafish present a unique combination of both complexity in physiology and simplicity of culture and have been recently shown to be

compatible with screening tools such as microfluidics (Hwang and Lu 2012) or culture in microtiter plates (Zon and Peterson 2005).

1.2.2 The Zebrafish Larvae

The zebrafish (*Danio rerio*) is a vertebrate small model organism that is widely used for *in vivo* chemical and genetic screens. Several desirable attributes contribute to the popularity of zebrafish larvae, including their small size, optical transparency, and rapid *ex vivo* growth in aqueous medium. Zebrafish models of many important human diseases have been developed (Zon and Peterson 2005, Lieschke and Currie 2007, Meeker and Trede 2008). Lead compounds discovered in zebrafish assays have been useful for drug development because of the high level of conservation of drug activity between mammals and zebrafish (Kari, Rodeck et al. 2007). There are also large numbers of zebrafish mutants available, facilitating the study of gene functions and the identification of cellular targets of new compounds. Due to these and other compelling advantages, zebrafish studies have grown at an exponential rate during the last two decades (Figure 1.2).

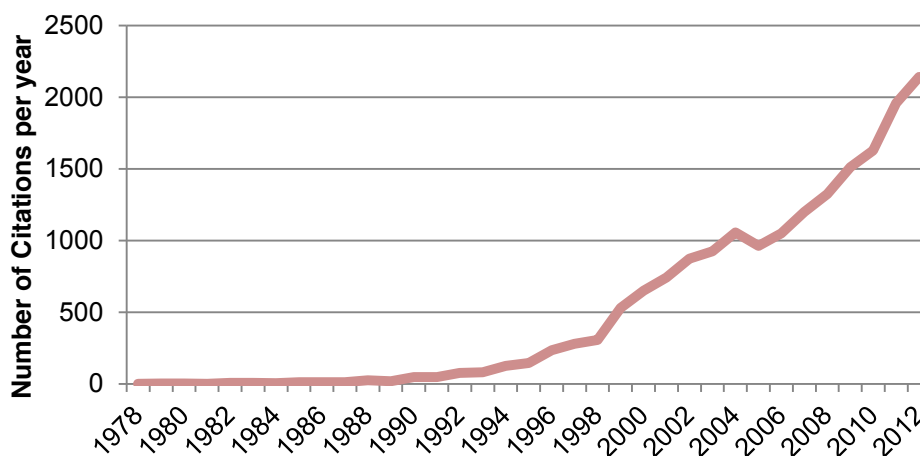


Figure 1.2: Number of citations containing “zebrafish” in the PUBMED database. The zebrafish community has experienced an exponential growth since the ‘90s. Source: <http://www.ncbi.nlm.nih.gov/pubmed> - last access 03/07/2013

1.2.2.1 Key features in the zebrafish larvae for HTS

Several features make the zebrafish larva an ideal candidate for HTS in the early stages of the drug discovery pipeline (Barut and Zon 2000, Rubinstein 2003, Zon and Peterson 2005):

1. **Small size:** At 5 days post fertilization zebrafish larvae only measure ~500 µm in diameter and ~4 mm in length. Their small length allows culture in microtiter plates and their small diameter allows visualization of their internal organs without the need of deep-tissue imaging techniques.
2. **Transparency:** zebrafish larvae are optically transparent in their early weeks of development. Only darkly pigmented melanophores in their outer skin absorb significant amounts of light, and simple chemical treatments and mutants have been developed to inhibit melanophore formation. The zebrafish's optical transparency allows for microscopy to visualize the internal organs *in vivo* without the need of clearing the tissue or histological slicing. Therefore, many imaging techniques developed for conventional HTS and HCS in cell-cultures can be adapted to the screening of zebrafish.
3. **Vertebrate:** zebrafish, like all members of the teleost family, are vertebrates and therefore are anatomically and genetically much more similar to mammals than other model organisms commonly used for HTS (e.g. *Drosophila*, *C. elegans*).
4. **Complex neuronal structures:** despite some differences in the size of particular structures, the overall organization of major brain components is highly conserved between zebrafish and human (Tropepe and Sive 2003), allowing researchers to study neurodegenerative diseases in an anatomical and physiologically relevant model.
5. **High conservation of compound activity with humans:** most drugs and other biologically active compounds have similar activity in zebrafish and humans (Shin and Fishman 2002, Rubinstein 2003, Zon and Peterson 2005, Lieschke and Currie 2007, McGrath and Li 2008), a key requirement for *in vivo* models of human pathology for drug discovery.

6. **Ease of culture:** zebrafish larvae can be cultured in a simple saline solution and are sustained by the nutrients in their yolk sac throughout the first 5-7 days of development, a few days later than typical end-point experiments. This allows larvae to be cultured in small volumes of medium (i.e.~50 μ l/ embryo) inside microtiter plates. A second advantage of the liquid medium is that stock solutions of test compounds can be added directly to the medium using protocols similar to cell-based assays.
7. **High number of progeny:** a single male and female can produce an average of ~200 viable embryos per week. This allows large and sustainable numbers of samples for screening for both wildtype and embryos from parents carrying known mutations.
8. **Ex vivo development:** zebrafish embryos are fertilized externally. This allows for quick collection of embryos as early as in the single cell stage. As we will discuss in the following chapter, collecting the embryos during this very early stage allows for microinjection of both mRNA and antisense oligonucleotides.
9. **Rapid development:** Embryonic development in the zebrafish larva is very rapid. After 5-6 days post-fertilization, all major organs are present in the larvae, and after 3-4 months they are able to produce progeny. Rapid development of the zebrafish embryo makes it ideal for the study of both normal and pathological development. Because early development is so rapid, gain- and loss-of-function studies can easily be performed throughout organogenesis by microinjection of mRNA or antisense oligonucleotides at the single-cell stage.
10. **Genome fully sequenced:** the zebrafish genome has been fully sequenced and annotated.
11. **Large array of genetic tools:** the zebrafish community has developed a wide array of genetic tools that permits generation and genotyping of a large number of mutants as well as analysis of gene expression.

1.2.2.2 Genetic tools in zebrafish larvae

One of the features fueling the exponential growth of the zebrafish field (Figure 1.2) is the array of genetic tools available to the community. Many of these techniques were born from the large-scale chemical mutagenesis screens carried out in the 1990s (Driever, Solnica-Krezel et al. 1996) (Haffter, Granato et al. 1996) and have been further refined as zebrafish have become a leading model of early vertebrate development.

These tools now allow rapid generation of new transgenics and mutants for most of the genes in the zebrafish. Community-wide initiatives such as the '*Zebrafish International Resource Center*' (ZIRC), the '*Zebrafish International Network*' (ZFIN) and the '*Zebrafish Mutation Project*' (ZMP) allow for wide distribution of the mutants, morpholino sequences and genome resources. Of particular interest to generating *in vivo* zebrafish models of complex phenotypes is the ZMP project. ZMP aims to create a knockout allele of every protein coding gene in the zebrafish genome by chemically mutating adults and characterizing the mutations using a combination of whole-exome enrichment and next generation sequencing (Howe, Bradford et al. 2013). Each allele they generate is sequenced and published online and the mutant is made available to the community through ZIRC. To date, ZMP has generated mutants for over 8,530 coding genes in the zebrafish genome, representing 32% of the 26,163 known coding genes in the entire genome. These initiatives are expected to lead to the development of innovative models of human genetic disorders or degenerative disorders with genetic predispositions.

Another useful tool that is widely used by zebrafish researchers is microinjection of genetic material during early development. Zebrafish embryos are collected immediately after fertilization (at the 1-4 cell stage) and a manual or automated microinjection system is used to deliver synthetic nucleic acids to the yolk cell, where they are rapidly and uniformly taken up by the developing blastomeres (Lu, Chen et al. 2007). This allows systemic delivery of both antisense morpholino oligonucleotides (Nasevicius and Ekker 2000) and mRNAs (Hyatt and Ekker 1999) to transiently knockdown or overexpress a target gene during the first 3-5 days of development. These two techniques can be combined to simultaneously knockdown the endogenous

transcript and overexpress a mutant variant of interest to test whether the mutant version is capable of rescuing the loss-of-function phenotype (Kim, Zaghloul et al. 2011, Singh, De Rienzo et al. 2011, Manzini, Tambunan et al. 2012, Mochida, Ganesh et al. 2012). Microinjection on early embryos is not a time consuming step, and trained technicians are capable of generating transient ‘mutants’ at rates of 300 in a single hour. Zebrafish researchers can thus examine the activity of both endogenous genes and human orthologs on a complex *in vivo* model at throughputs amenable to large-scale screening.

Table 2 shows a list of genetic techniques commonly used by the zebrafish community (Trophepe and Sive 2003).

Table 2: Genetic techniques available to the zebrafish community. Modified from: (Trophepe and Sive 2003).

| Goal | Technique | | References |
|-------------------|---|-----------------------|---|
| Lineage tracing | Caged fluorescein dextran | | (Goldstein and Fishman 1998) |
| Loss of function | Mutagenesis | Chemical | (Driever, Solnica-Krezel et al. 1996) |
| | | Insertional | (Amsterdam, Burgess et al. 1999) |
| | | Transposable elements | (Kawakami, Shima et al. 2000) |
| | | Targeted | (Wienholds, Schulte-Merker et al. 2002) |
| | Antisense morpholinos | | (Nasevicius and Ekker 2000) |
| Gain of function | mRNA microinjection | | (Hyatt and Ekker 1999) |
| | Caged RNAs | | (Ando, Furuta et al. 2001) |
| | Microelectroporation | | (Haas, Sin et al. 2001) |
| | Hormone inducible constructs | | (Bellipanni, Murakami et al. 2000) |
| Gene expression | <i>In situ</i> hybridization & <i>In situ</i> databases | | ZFIN |
| | Immunocytochemistry | | |
| Genomics | Annotated genome database | | www.ensembl.org - last access 02/04/13 |
| Promoter Analysis | Stable transgenic reporter lines | | (Thermes, Grabher et al. 2002) |
| | Sperm nuclear transplantation | | (Jesuthasan and Subburaju 2002) |

1.3 General Problem

As described in the previous section, the zebrafish larva is an ideal small model organism for screening as it has sufficient complexity to accurately model most complex physiologic or pathological phenotypes *in vivo* while maintaining simplicity in their husbandry and imaging.

Despite their potential as a candidate for high-throughput and high-content screening in both drug discovery and biomedical research, most groups that focus on studying zebrafish still rely on manual handling techniques such as pipetting anesthetized embryos manually with Pasteur pipettes and orienting them with tweezers, and on simple and often qualitative descriptions of the observed phenotypes which commonly focus on a small set of predefined read-outs (e.g. ventricle size – increased or reduced-).

1.3.1 Low throughput

Current handling of zebrafish as of this date either relies on manual and low throughput approaches that do not permit large scale studies, or on screening techniques typically present in *in vitro* screening, such as screening in microtiter plates. This second set of techniques however do not take full advantage of the complexity of the *in vivo* models because, in contrast to cell-culture models the zebrafish is not always located flatly against the bottom of the plate, and because imaging zebrafish requires previous orientation of the animals. Hence, the common approach to image zebrafish larvae at high-resolution has focused on manual approaches.

Visualizing most zebrafish organs requires manipulating and properly orienting the larvae. Even with confocal or two-photon microscopy, optical access is often impeded by pigmentation, by intervening organs such as eyes and heart or by the highly autofluorescent yolk sac. Current methods to address these challenges involve treatment with the toxic chemical phenylthiourea to suppress pigmentation (Karlsson, von Hofsten et al. 2001), manually transferring zebrafish from multiwell plates or reservoirs and manually orienting them in viscous media such as agar. These steps are frequently performed with tweezers while the agar solidifies and thus researchers can only handle larvae in small numbers. After orienting and immobilizing the larvae in solidified agar, the samples are moved to the microscope for imaging. Due to the involvedness of these processes, before the work presented here, there was no automated way to orient and prepare the larvae for imaging. The reduced throughput and manual nature of this approach limits its adoption in the drug-screening pipeline (Table 3).

Table 3: Comparison of current manual screening characteristics and requirements for HTS.

| Current Manual Screenings | Requirements for HTS |
|----------------------------------|-----------------------------|
| User biased | Computerized |
| Not capable of automation | Capable of Automation |
| Immobilization in agar | Fluidics |
| Single read-out | Multiple unbiased read-outs |

1.3.2 Low content

To date, screens in zebrafish have typically relied on manual assessment of morphology and often ignored phenotypes not encompassed by more than a small number of pre-defined read-outs. Similarly, although large-scale genetic screens have been carried out for decades in zebrafish, morphological phenotyping is often non-quantitative and limited to features only easily observable.

The ideal phenotyping platform should be capable of handling live or fixed zebrafish in a high-throughput manner and automatically acquiring three-dimensional (3D) images of structures encompassing large regions of the body at micron-level resolution. This will enable a HCS approach in which complex phenotypes are quantitatively profiled in great detail across large numbers of animals. This would allow the full diversity of phenotypes in a given genetic or chemical screen to be documented and subsequently analyzed using data mining and bioinformatics tools as is currently done in HCS of *in vitro* cell culture models.

1.4 Specific Research Goals

The goal of the work presented here is the development of technologies that will enable researchers to fully exploit the potential of the zebrafish larvae for high-throughput and high-content screenings.

To allow wide adoption of zebrafish screening, the first requirement is its feasibility in a large-scale screen environment where tens to hundreds of thousands of compounds are routinely

tested. Therefore, the technologies described in this work require **high-throughputs** to allow large volumes of samples to be examined. Similarly, to allow for long-term operation and objectivity it is necessary for the technologies to be **automatable**. To fully capture the potential as an *in vivo* model these technologies would require the capability of **high-resolution microscopy** and capacity to visualize the sample from **any predetermined angle**. Lastly, to allow HCS our technologies must be capable of acquiring multiple measurements to **extensively define the phenotype** caused by each condition.



Figure 1.3: Steps of a typical zebrafish screen. Embryos are collected from adults mating and dechorionated. In case of a drug or toxicity screen animals are treated with compounds. In knock-out or gain-of-function experiments larvae are microinjected with morpholinos or mRNA. At the experimental end-point animals are stained with an appropriate protocol. Animals are then prepared for imaging by fixing them in agarose gels. Animals are subsequently imaged using high-resolution microscopes. The images are analyzed for phenotyping or scoring for predefined read-outs. After all data is collected it is analyzed to validate or refute the screen hypothesis. Red blocks represent the current rate-limiting steps and the target steps for the technologies presented in this dissertation.

Figure 1.3 shows the typical steps of a typical zebrafish screen. With the appearance of large capacity mating tanks the mating of adults and the collection of the embryos have become trivial and not rate limiting for HTS. A combination of automated liquid handler and previously reported zebrafish sorters (Graf, Hotzel et al. 2011) is capable of automatically and rapidly handling the treatment step of the screening. The use of stable transgenic lines and automated *whole mount in situ* hybridization platforms significantly increase the throughput and minimize user involvement in the staining steps. We have therefore focused our attention in the three remaining screening steps before the data analysis: **sample preparation**, **imaging** and **scoring/phenotyping** prior to analysis.

Based on the need to increase throughput for wide adoption of zebrafish into the drug screening pipeline we have selected the following aims for the thesis work presented here:

Aim 1: The development of an automated microfluidic-based screening platform capable of loading zebrafish larvae from microtiter plates or reservoirs into the field of view of a microscope and that allows imaging the larvae at high-resolution from multiple angles.

Aim 2: The development of a system capable of imaging zebrafish larvae at a high-throughput (i.e. less than five seconds per animal), at micrometer resolution in 3D to allow phenotyping of complex organs and features.

Aim 3: The development of a collection of algorithms capable of extracting a large number of phenotypic features from the imaging data obtained from the system described in Aims 1 and 2 to allow HCS of entire larvae.

1.5 Organization of the dissertation

In **Chapter I**, I briefly outline the general methodology and current challenges in drug discovery, mainly the gap between simplified *in vitro* models and the complexity of *in vivo* models. I then describe the use of small model organisms as a bridge between both, and how the zebrafish presents itself as an ideal small model organism for high-throughput screening. Lastly I outline the research aims on which this work is based. The rest of the thesis is organized as follows.

In **Chapter II**, I give a review of the prior technologies for manipulating and imaging zebrafish larvae. These techniques include both the golden standard and recent technologies when the work presented in this thesis was initiated.

In **Chapter III**, I demonstrate a microfluidic system capable of handling zebrafish larvae at throughputs of approximately three samples per minute. In contrast to other previously described high-throughput systems, our instrument is capable of acquiring images at cellular and even subcellular resolutions, which signifies several order of magnitudes of throughput above previous techniques with similar imaging and phenotyping capabilities. This chapter describes our technique and device with sufficient detail for it to be replicated in other labs. In this chapter I also demonstrate that by using our system we are able to employ high-NA lenses that require short working distances. The use of these lenses permits high-precision imaging and optical

manipulation techniques, which we demonstrate by performing subcellular resolution femtosecond laser axotomy of the zebrafish's lateral line and tracking its growth with confocal microscopy.

In **Chapter IV**, I present a collection of improvements over the screening system described in Chapter III. I first present a modified system capable of parallelizing various processes in the screening procedures. This allows the system to handle multiple larvae simultaneously. I demonstrate that through this improvement we are able to significantly reduce the screening type and thus double the throughput of the platform. To further improve on our previous work I here also present a novel collection of algorithms to automate the positioning and orientation of the larvae inside the system. This allows for fully automated handling of the system. Finally, I present results from tests on different materials for the imaging capillary and scores based on their autofluorescence and their optical properties which are quantified by computing point-spread-function of sub-micron fluorescence beads using confocal microscopy. We quantitatively demonstrate the use of ultrathin borosilicate to be an adequate imaging material as compared with other materials proposed by different groups.

In **Chapter V** I present two novel tools for high-content and high-throughputs screening of zebrafish larvae. I first introduce an improved set of algorithms for rapid optical projection tomography. I show that through a set of computer algorithms designed to correct for imperfect conditions in the sample preparation, we can acquire tomographic reconstructions in approximately 2.5 seconds while maintaining micrometer resolution reconstructions. This improvement reduces the imaging time by approximately three orders of magnitude – previous work showed image acquisition times of approximately 30 minutes. This increase in throughput allows for the first time the use of optical-projection-tomography in a high-throughput framework and allows for large scale studies to operate in complete volumetric reconstructions of the samples. In the second part of this chapter, I demonstrate algorithms to fully exploit the data from the volumetric reconstructions obtained through our improved optical-projection-tomography system. An algorithm extracts hundreds of morphometrical measurements of each sample and

constructs an array of values that defines the phenotype of the sample. This signature is then used to compute a hierarchical clustering that allows the user to infer similarities and differences in the samples in an objective fashion. I have named this approach 'hyperdimensional *in vivo* phenotyping'. I demonstrate both these tools by performing a proof-of-concepts screen on the effect of teratogens in the craniofacial development of zebrafish larvae. Our hyperdimensional phenotyping framework allows us to successfully classify the teratogens by their compound class and indicates similarities in classes that are backed by their known mechanisms of actions *in vivo* and *in vitro*.

Finally, in **Chapter VI**, I present a summary and concluding remarks on the work presented in this dissertation.

2 Technologies for manipulating and imaging zebrafish larvae

In the next pages I will present prior art in technologies for phenotypic screening, for both microtiter and stand alone, for rapid injection, for optical manipulations and for novel imaging techniques designed to work with the zebrafish larvae. These technologies are designed to exploit the complexities of the zebrafish and reduce the complexity of its imaging and phenotyping.

2.1 Technologies for phenotypic screening of zebrafish inside microtiter plates

One of the key advantages of using zebrafish for screening is its simple culture. Due to their small size and ability to develop without food during their first week, zebrafish embryos can be raised inside 96- and 384-multiwell plates, allowing the use of standard liquid handling techniques. Early screenings methods have been based on in-well techniques where embryos are manipulated and imaged inside their respective wells. Multiwell screens have been used to study drug-induced toxicity to analyze hepatotoxicity, cardiotoxicity and toxicity affecting development (McGrath and Li 2008). Similar techniques have also been developed to identify compounds that produce models of human-related diseases such as Long QR syndrome (Milan and Macrae 2008), hair cell toxicity from heavy metals (Ton and Parng 2005, Hernandez, Moreno et al. 2006) and developmental neurotoxicity (Parng, Roy et al. 2007). Other in-well screens have been aimed at chemically suppressing genetic mutations. In 2004 Peterson *et al.* chemically suppressed the genetic mutation gridlock (*grl*), which serve as a model for human aortic-coarction (Peterson, Shaw et al. 2004). More recent advances have enabled behavioral assays on larvae in wells. In 2010, Kokel *et al.* identified a series of small neuroactive molecules capable of modifying the photomotor response, i.e. a set of motor behaviors elicited by the larvae following high-intensity light stimulus (Kokel, Bryan et al. 2010), and Rihel *et al.* identified a set of drugs involved in the

regulation of rest and wake responses by monitoring larvae for long periods of light and darkness (Rihel, Prober et al. 2010).

2.2 Technologies for phenotypic screening outside microtiter plates

Although in-well screening allows toxicity, genetic, chemical and behavior-based screenings there are significant limitations in the complexity of assays that can be conducted inside wells. Firstly, zebrafish are localized and oriented arbitrarily in the well. Visualization of key organs in the zebrafish is thus blocked by organs such as the eyes and the yolk sac or the skin pigmentations. This lack of optical access to the entire animal seriously limits the type, quality, and quantity of phenotypes that can be scored in multiwell plates (Pardo-Martin, Chang et al. 2010). Secondly, standard methods for manipulation of the larvae in the wells are limited to manual techniques such as orientation and movement of the larvae using forceps or similar tools. Recently, special multiwell plates with 45° mirrors in each well have been developed for imaging zebrafish larvae at multiple angles inside these wells; however larvae still needs to be manually positioned inside. In addition, due to the large distance between the sample and objective, only air objective lenses with long working distance can be used. Such objective lenses have too low numerical apertures (NA) to be used for high-resolution imaging or for confocal microscopy. Optical manipulation techniques such as photo-uncaging (Ando, Furuta et al. 2001, Ando, Kobayashi et al. 2005, Dmochowski and Tang 2007, Shestopalov, Sinha et al. 2007, Tang, Maegawa et al. 2007, Neveu, Aujard et al. 2008, Ouyang, Shestopalov et al. 2009, Tomasini, Schuler et al. 2009, Deiters, Garner et al. 2010), photo ablation (Serbedzija, Chen et al. 1998, Liu and Fetcho 1999, Roeser and Baier 2003, Yang, Sengelmann et al. 2004) and femtosecond laser surgery (O'Brien, Rieger et al. 2009, Pardo-Martin, Chang et al. 2010, Steinmeyer, Gilleland et al. 2010) are similarly not feasible. These limitations have motivated the development of new imaging and screening tools to handle the animals outside multi-well plates.

2.3 Flow cytometry

The small size of early-stage zebrafish permits the use of flow cytometry techniques. The makers of the COPAS Biosort also make a product, the COPAS XL, with larger bore fluidics that enable rapid 1-D fluorescence profiling and sorting of zebrafish eggs, embryos and hatchlings.

2.4 Use of capillaries for phenotyping and husbandry

Small capillaries are also used to immobilize zebrafish larva outside of microtiter plates. This facilitates optical access to the entire fish, since the region of interest can be positioned closer to the objective by rotating the capillary. This orientation also allows imaging of regions that might otherwise be obscured by intervening organs or skin pigmentations (e.g. the hindbrain is blocked laterally by the eyes and anteriorly by the heart). Buckley *et al.* used of capillaries to orient zebrafish in order to visualize *olig2* positive cells responsible for myelination (Buckley, Goldsmith *et al.* 2008). In this setup, the capillary is anchored to movable stage and is submerged in water to reduce optical aberrations from refractive index mismatch. A more recent paper Petzold *et al.* used a similar system and tested different materials for their capillaries in order to further reduce the index mismatch (Petzold, Bedell *et al.* 2010), although image quality was low due to autofluorescence and distortion by the type of capillaries used in this study.

Capillaries can also be used for animal husbandry. Funfak *et al.* used a long Teflon capillary to house embryos for long durations (5 days) (Funfak, Brösing *et al.* 2007). By inserting a bubble of air between each embryo they were able to divide the tube into fluid segments where embryos could be raised independently. Creating such separations also allows the use of different chemicals in each segment and permitted study the effects of chemicals using small volumes. Using this technique they raised 260 larvae in a single tube. Fluid-segment techniques offer a compact means to store larvae, but also limit access to the animals and prevent exchange of media/chemicals.

2.4.1 Microfluidics for zebrafish embryo culture

Although zebrafish embryos/larvae are small relative to most model organisms, they are still much larger than single cells or *C. elegans*. This larger size precludes the use of most microfabrication techniques, and to date there are few examples of microfluidic devices for zebrafish. One example is the work of Shen *et al.*, who developed a simple microfluidic chip to expose a single zebrafish embryo to a variety of cytokines and growth factors and analyze their effects on development (Shen, Li et al. 2009). Their device consisted of a bilayered PDMS chip with a thick layer and a thin layer. The thick layer had a funnel-shaped feature that stably held the embryo, while the thin layer contained a microfluidic channel to expose larvae to chemicals.

2.5 Rapid injection of zebrafish embryos

An advantage of zebrafish is the relatively large size of its single cell embryo. The zebrafish embryo measures approximately 700 μm in diameter and is in the single cell stage for approximately 45 minutes following fertilization (Kimmel, Ballard et al. 1995). This gives a window of opportunity to inject genetic material using a micropipette in order to generate mutant and transgenic animals. Microinjection is commonly performed manually by an experienced researcher using a micromanipulator and a stereo microscope. This limits the use of injection in large-scale assays.

In 2007 Lu *et al.* developed an automatic system for batch microinjection of zebrafish embryos (Lu, Chen et al. 2007). Image-processing methods allowed the system to automatically guide the micropipette needle to the center of the embryos. A piezo-resistive material was used to measure the micro-forces generated by the entrance of the pipette through the chorion and the cell-wall (Figure 2.1). The authors were able to rapidly guide the needle into the single cell embryo and inject genetic material automatically. Other groups have also developed systems with variations in both the capture of the eggs and the image processing algorithms, achieving speeds up to 15 embryos per minute with a success rate of 98.5% (Wang, Liu et al. 2007, Huang, Sun et al. 2009).

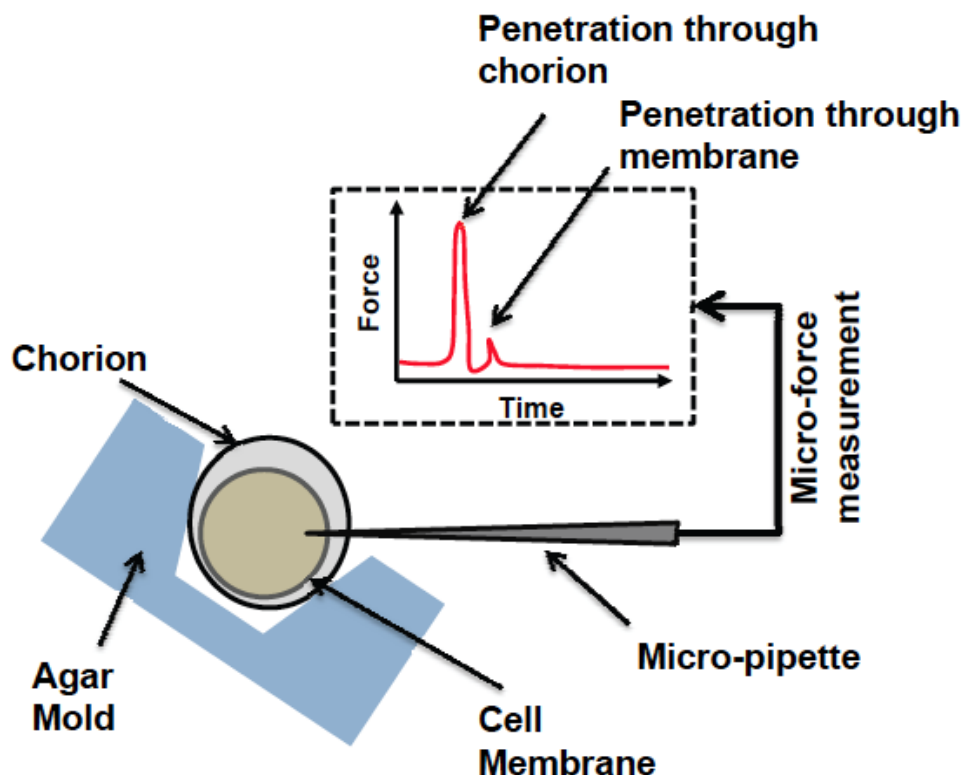


Figure 2.1: Schematic representation of an automated injection system of zebrafish eggs. The zebrafish embryo is captured in an agar mold. A micro-pipette with a micro-force measurement system is optically guided into the embryo. The force measurement system is used to detect the puncture of the pipette of both the chorion and cell membrane. Punctures are identified by a sharp peak in the force profile as represented in the force-time graph.

2.6 Optical manipulation of zebrafish

The optical transparency of zebrafish larvae allows a variety of optical manipulations to be performed. With the high-throughput zebrafish screening technology I will present in subsequent chapters, these techniques can also be performed on a large scale for complex genetic and chemical screens, for instance, on tissue development and regeneration.

2.6.1 Laser ablation

Ablation of single cells or an area of cells using UV light is a widespread technique in the zebrafish field. By pulsing a UV-laser focused on a particular region of the fish, sufficient energy can be delivered to either eliminate a cell or group of cells (Serbedzija, Chen et al. 1998, Liu and

Fetcho 1999, Roeser and Baier 2003, Yang, Sengemann et al. 2004) or to locally heat them (Halloran, Sato-Maeda et al. 2000). The systems are usually composed of a ~440 nm pulsed UV laser coupled to a conventional microscope. In early embryonic stages, UV-laser ablation can eliminate a particular set of progenitor cells for developmental studies (Serbedzija, Chen et al. 1998). Laser ablation has been used in developed larvae for various purposes. Yang *et al.* damaged melanocytes at the surface of the embryo with a Q-switched neodymium:yttrium-aluminum-garnet dermatology laser and later visualized their regrowth and regeneration ((Yang, Sengemann et al. 2004)). Other studies have combined the use of laser ablation and functional assays to investigate neural pathways by studying loss-of-function after precise ablation of neurons in fully developed larvae. In 1999 Liu *et al.* ablated Mauthner cells (Liu and Fetcho 1999, Zottoli and Faber 2000) in the hindbrain to demonstrate their functional role in rapid escape response. Similarly, in 2003 Roeser *et al.* ablated the optical tectum of developed larvae to investigate its role in the optokinetic and optomotor behavioral responses (Roeser and Baier 2003). UV lasers have also been used to locally heat regions of zebrafish to locally induce genes under the control of a *hsp70* promoter (Halloran, Sato-Maeda et al. 2000).

Femtosecond laser surgery has also been used on zebrafish for higher resolution ablation deeper within the tissue while eliminating out-of-focus tissue damage (Pardo-Martin, Chang et al. 2010, Steinmeyer, Gilleland et al. 2010). The local nature of this process enables its use for dissections and surgery on *in vivo* samples with high repeatability and low collateral damage, and has been used in the zebrafish community to sever individual branches of peripheral axons as well as nerves in larvae. In 2009, O'Brien *et al.* used two-photon imaging together with femtosecond laser ablation of peripheral axons (O'Brien, Rieger et al. 2009). Combining imaging with axotomy using multi-photon microscopy can be achieved using commercial systems, but the cost of a commercial multi-photon system is limiting for many laboratories. Another approach is to introduce a femtosecond laser beam in the optical path of a standard fluorescence microscope and align the planes of focus to simultaneously image and target the region of interest as we described previously in a protocol manuscript (Steinmeyer, Gilleland et al. 2010) (see Appendix). Zebrafish is a powerful model for regenerative biology, and we recently showed that femtosecond

laser microsurgery can be used in a high-throughput platform for large-scale genetic and chemical studies of *in vivo* regeneration in zebrafish (Pardo-Martin, Chang et al. 2010).

2.6.2 Spatially- and temporally-controlled in vivo release of chemicals and oligonucleotides by photouncaging in zebrafish

Optical uncaging of DNA and/or RNA by means of precise UV illumination to control local gene expression in zebrafish is another useful technique (Ando, Furuta et al. 2001, Ando, Kobayashi et al. 2005, Dmochowski and Tang 2007, Shestopalov, Sinha et al. 2007, Tang, Maegawa et al. 2007, Neveu, Aujard et al. 2008, Ouyang, Shestopalov et al. 2009, Tomasini, Schuler et al. 2009, Deiters, Garner et al. 2010). In 2001, Ando *et al.* first demonstrated photo-uncaging of RNA in zebrafish. The RNA had been previously chemically caged by 6-bromo-4-diazomethyl-7-hydroxycoumarin (Bhc-diazo) (Ando, Furuta et al. 2001). The authors showed that the Bhc-caged mRNA underwent photolysis (i.e. became uncaged) when the molecules were excited with UV light (~350 nm) and that the uncaged RNA strands became translationally active in comparison with their Bhc-caged counterparts. By injecting Bhc-caged mRNA encoding GFP in the one-cell embryo the authors were able to keep the GFP expression silent until it was stimulated locally by UV light. In 2005, the same authors used photo-uncaging-based gene expression to study the local effects of *Lhx2* and *Six3* in the development and growth of the zebrafish embryo's forebrain (Ando, Kobayashi et al. 2005). Using similar techniques several groups have reported the uncaging of morpholinos demonstrating spatially controlled gene silencing (Shestopalov, Sinha et al. 2007, Ouyang, Shestopalov et al. 2009, Tomasini, Schuler et al. 2009, Deiters, Garner et al. 2010) as well as uncaging of small molecules such as signaling factors (Neveu, Aujard et al. 2008).

2.6.3 Photo-labeling with photoconvertible proteins

In 2002 Ando *et al.* showed the first use of the photoconvertible protein Kaede. This protein undergoes photoconversion from green to red fluorescence under stimulation with UV light (Ando, Hama et al. 2002). Selective photoconversion can tag Kaede-labeled cells so they can later be

distinguished. This enables identification specific cells during development, simplifying tracking of cell lineages. In 2006 Sato *et al.* generated a transgenic zebrafish line which expressed the Kaede fluorophore in neurons using the pan-neuronal promoter *HuC* (Sato, Takahoko et al. 2006). The photoconverted Kaede diffused through the axons, marking them red and enabling their tracking (Sato, Takahoko et al. 2006). Kimura *et al.* used *alx:kaede* to study spinal cord development and determined that early born *alx* type neurons are located more dorsally than those born later (Kimura 2004). Exposure of cells to UV only during development causes any new Kaede proteins expressed after the illumination period to preserve their original green color. Thus, cells without any red protein showed those that differentiated into *alx* neurons after the time of illumination. Scott *et al.* performed an enhancer trap screen using *GAL4* to drive expression of Kaede linked to the upstream activator sequence (UAS) (McLean and Fetcho 2008). This allowed labeling of specific tissues with the unconverted Kaede, and by photoconverting Kaede the morphologies of individual neurons within the tissue were identifiable. Similarly, McLean *et al.* studied the development of the spinal cord processes in the developing larvae (Mckinney, Murphy et al. 2009). Another photoconvertible protein, Eos, has also been used to analyze cell lineages emanating from the zebrafish neural crest (Curran, Lister et al. 2010).

2.7 Technologies for the imaging of zebrafish larvae

The optical transparency of zebrafish larvae allows visualization of complex processes both superficially and in deep tissues. Standard optical fluorescence microscopy suffers from out-of-focus fluorescence and is limited for most imaging purposes. Examples of complex phenotypes requiring advanced imaging methods include measuring variations in the number of cells in specific populations (Pisharath, Rhee et al. 2007, Wen, Wei et al. 2008), variations in axon guidance (Fricke, Lee et al. 2001), dendritic formation (Jontes, Buchanan et al. 2000), or neurogenesis (Das, Payer et al. 2003). In addition, high-throughput screens require high-speed imaging technologies. In this section we outline a selection of imaging techniques capable of meeting these challenges.

2.7.1 Confocal imaging systems

Laser scanning confocal microscopy (LSCM) is commonly used for high-resolution three-dimensional *in vivo* imaging. A laser is scanned through the specimen to excite fluorophores, and the emitted fluorescence signal is filtered by a pinhole located in front of the detector which rejects the out-of-focus signal by selectively letting through only the photons emitted from the imaging plane. This allows imaging with high axial and depth resolution, however LSCM typically suffers from low frame rates. The frame rate of LSCM can also be increased by using resonance scanners that reach scanning frequencies up to 16 kHz, however image quality significantly degrades due to reduced signal-to-noise ratio.

Spinning disk confocal microscopy permits faster imaging through the use of a spinning disk with multiple pinholes arranged in a rotating array. This creates multiple scanning points in the specimen plane that together completely scan the sample with each turn (i.e. multifocal excitation). Sensitive electron-multiplying charge-coupled detector (EMCCD) cameras are typically used to detect the light emitted back through the pinholes, which image the entire field of view at once. Conventional spinning-disk confocal microscopy suffers from the lack of sufficient laser power per focal spot of the multifocal excitation beam. The Yokogawa spinning disk confocal microscopy overcomes this problem in excitation efficiency by using another disk with microlenses in parallel to the pinhole disk to efficiently collect and collimate laser excitation. Although spinning disk confocal microscopes have high frame rates, they suffer from decreased axial resolution due to the use of large pinholes. To overcome this challenge, new confocal technologies have been recently introduced that use variable pinhole arrays in combination with laser scanners. This configuration allows video frame rates while achieving depth resolutions similar to LSCM in weakly scattering media. A common challenge with all of these multifocal excitation strategies with respect to LSCM is the crosstalk between adjacent pinholes, which becomes a significant problem particularly in scattering tissues.

Structured illumination can be used to achieve optical sectioning as well (Juskaitis, Wilson et al. 1996, Neil, Juskaitis et al. 1997). This technique allows high-resolution video-frame-rate confocal

imaging at low cost. However, the post-processing required to generate the optically sectioned images is sensitive to saturation and noise and can introduced unwanted aberrations that make image quantification difficult.

2.7.2 Two-photon microscopy

In zebrafish larvae, beyond depths of a few hundred micrometers, optical scattering becomes significant. As a result of this, both the resolution and the image quality of confocal microscopes rapidly deteriorate. Two-photon microscopy has a deeper penetration and imaging depth than confocal microscopy, which makes it a powerful tool for imaging the zebrafish nervous system. Two-photon microscopy requires the use of ultrafast pulsed lasers to achieve the photon densities necessary for efficient multi-photon absorption. As in LSCM the laser beam is scanned over the sample and the emitted photons are collected by a photomultiplier tube (PMT). Because it is a multiphoton process, the fluorescence excitation occurs only at the point of focus and therefore most of the emitted light can be collected. However, there are two disadvantages to two-photon microscopy in general: lower scan speeds and high cost, which is a significant limitation for high-throughput assays as well as for imaging fast processes such as neuronal activity by Ca^{2+} imaging. The scan speed is limited by the ratio of single photon absorption (which heats the sample) and the two-photon absorption (which produces the fluorescence signal). This ratio can be improved by increasing the laser pulse repetition rate. One technique to increase pulse rate uses passive pulse splitters that divide, delay and recombine each laser pulse, subdividing each pulse into a pulse train. This method has been shown to increase the overall intensity of the fluorescence signal without compromising the thermal integrity of the sample to achieve a higher signal-to-noise ratio, enabling faster imaging rates in small organisms like *C. elegans* (Ji, Magee et al. 2008). Another approach uses multifocal laser excitation to scan the sample rapidly while collecting the light onto a PMT array or an EMCCD camera (Bewersdorf, Pick et al. 1998). This can significantly increase the frame rate but sacrifices the signal-to-noise and imaging depth due to the crosstalk between adjacent PMTs or CCD pixels.

2.7.3 Light-sheet microscopy for high-speed imaging of zebrafish

Light-sheet microscopy is a technique that enables rapid imaging of whole zebrafish and that eliminates the out-of-focus signal by selectively imaging individual planes rather than eliminating it through optics (Voie, Burns et al. 1993, Fuchs, Jaffe et al. 2002, Mauch, Dodt et al. 2007). The sample is illuminated from the side using a plane-sheet of light and the fluorescence signal is detected with an objective located orthogonally (Figure 2.2). By decoupling the excitation and collection of light, the axial resolution can be increased to 6 μm from the 20 μm resolution of conventional fluorescence microscopy. Furthermore, out-of-plane photobleaching was also reduced, since only the plane of interest was illuminated at once.

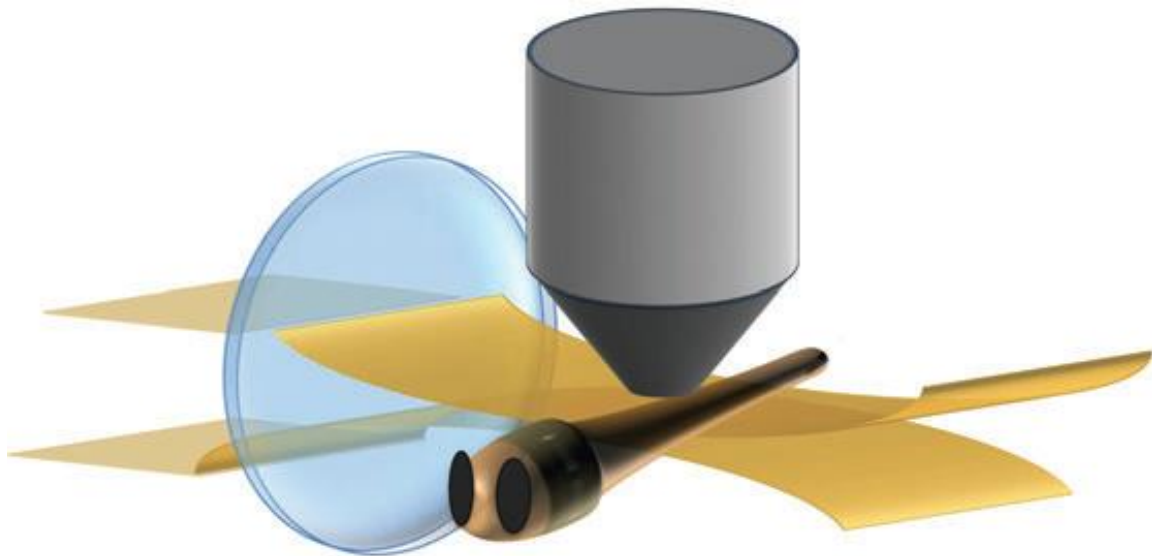


Figure 2.2: Schematic representation of light-sheet microscopy. The sample is illuminated from the side and imaged from an orthogonal plane. A thin plane of fluorescence excitation is achieved by a cylindrical lens, which prevents out-of-focus excitation and emission.

A possible disadvantage of this method is that, when dealing with scattering samples, the illumination, and hence the axial resolution, is not homogeneous throughout the imaging plane. Huisken *et al.* solved this issue by embedding the sample in a rotating capillary and acquiring image stacks at a variety of orientations (Huisken, Swoger et al. 2004). Image processing enabled a tomographic reconstruction that compensated for such aberrations and the loss of

signal that occurred with increasing penetration depths. The authors also demonstrated the effectiveness of this technique for imaging opaque internal organs, such as those of *Drosophila* embryos and zebrafish larvae.

The same group later described advancements of the technology that allowed rapid scanning of the light-sheet using galvo scanners (Keller, Schmidt et al. 2008). Keller *et al.* used this method to follow the development of the zebrafish embryo by simultaneously imaging and tracking 16,000 cells with their system, imaging the entire embryo every 90 seconds. Image resolution was improved by the use of structured-illumination, achieved by modulating the plane illumination using three different phases by a moving micro-grid (Breuninger, Greger et al. 2007). The combination of light-sheet microscopy and structured illumination yielded higher resolution due to the elimination of the specimen-related scattering signal but increased the acquisition time three-fold. In 2010 Keller *et al.* improved this method, allowing the selection of multiple phases by replacing the micro-grid with an electronic modulator (Keller, Schmidt et al. 2010), thus increasing both the acquisition speed and imaging resolution.

2.7.4 Whole animal blood-flow imaging

Zebrafish is well-suited for studying cardiovascular development and pathologies. The zebrafish heart starts beating 22 hours-post-fertilization (hpf) and the cardiovascular system is fully developed and functioning at 36 hpf (while the larvae are still highly transparent). Due to their small size, zebrafish larvae do not require circulation for several days. This allows researchers to test drugs and compounds that lethally affect the cardiovascular system without killing the animals. Conventional methods to measure blood flow involve high-speed imaging and single cell tracking; however these are too unreliable and computationally intensive for large-scale genetic and chemical screens. This has prompted use of other imaging technologies such as speckle imaging and optical Doppler tomography (Vennemann, Lindken et al. 2007).

Laser speckle contrast imaging uses the statistics of image speckle. A laser reflected on stationary particles creates high contrast speckles, and when the particles reflecting the laser are

moving the speckle pattern changes. In images with long exposure times, the contrasts of the speckles reflect how stationary the particles are at that location. This allows direct quantification of the flow at the image plane at any orientation (Fercher and Briers 1981), which significantly reduces the computational cost for image analysis and also reduces the speed requirements for image acquisition by the camera.

Another technique recently developed for the study of blood flow in the zebrafish larvae is Fourier Domain Optical Doppler tomography (FD-ODT) (Iftimia, Hammer et al. 2008), which is based on the principles of optical Doppler tomography (Ding, Zhao et al. 2002). Using a FD-ODT system with two beams Iftimia *et al.* were able to measure *in vivo* the blood flow in zebrafish larvae independently of the vessel orientation. Using this method they measured the blood flow in different regions of the larvae, including the telencephalon, the notochord, the branchial arches, the retina and both chambers of the heart, demonstrating the viability of their technology for accurately measuring blood-flow with high-resolution, a key requirement for studies of cardiovascular pathologies (Iftimia, Hammer et al. 2008).

2.7.5 Measuring neural activity using calcium imaging

Neural activity in zebrafish can be measured *in vivo* by imaging calcium transients using injected or genetically-encoded calcium indicators. Higashijima *et al.* expressed the calcium indicator cameleon in zebrafish sensory and spinal cord neurons (Li, Mack et al. 2005). This was the first demonstration of the use of a genetically-encoded calcium indicator in a behaving vertebrate. Calcium imaging has been used to study zebrafish olfaction using both transgenic animals (Li, Mack et al. 2005) and injected calcium indicators (Yaksi, Judkewitz et al. 2007). Niell *et al.* used a miniature LCD to provide high-resolution visual stimuli and simultaneously measured calcium transients in the tectal neurons using two-photon imaging. This allowed the authors to measure the rate of development of several characteristics of vision in zebrafish (Niell and Smith 2005).

2.7.6 Label-free nonlinear microscopy

Label-free non-linear microscopy (LNM) offers another method for whole-animal *in vivo* imaging (Olivier, Luengo-Oroz et al. 2010). LNM takes advantage of the non-linear optical properties of the sample, specifically the second harmonic generation (SHG) efficiency of microtubules and third harmonic generation (THG) efficiency of lipid-water interfaces. In LNM the sample is illuminated by the scan of an infrared laser beam (~1,200 nm). As the laser light passes through the specimen some photons enter harmonic resonance at the positions where SHG and THG are high and exit the sample with their frequency doubled or tripled (i.e. at the locations of microtubules and lipid-water interfaces respectively). The location of these structures can be thus located by filtering and detecting photons via multiple detectors. As this approach is only dependent on the intrinsic optical properties of the specimen, there is no need for fluorescence labeling, and it therefore makes LNM a useful technology for *in vivo* imaging of embryos without the need to produce transgenics. In 2010, Olivier *et al.* first used LNM to study the development of the zebrafish. They imaged the first 10 cell-divisions during embryogenesis and, by segmenting the cells, they were able to track cell lineages (Olivier, Luengo-Oroz et al. 2010). Using LNM they were able to image entire embryos with $2 \times 2 \times 4 \mu\text{m}$ resolution within 80 sec, without the use of fluorescence markers.

Another label-free imaging technique used for zebrafish larvae is Coherent Anti-Stokes Raman Spectroscopy (CARS). CARS is a point-scanning technique that can detect the vibrational emission frequencies of the molecules within the specimen by exciting their vibrational states and stimulating their emission via a third-order nonlinear process (Zumbusch, Holtom et al. 1999). CARS microscopy can therefore be used to visualize, without labels, molecules with particular vibrational signatures such as lipids (Enejder, Brackmann et al. 2010). The cellular storage of lipids *in vivo* in both zebrafish (Höltkä-Vuori, Salo et al. 2010) and *C. elegans* (Hellerer, Axäng et al. 2007) have been visualized using this technique. In 2010, Johnston *et al.* used CARS microscopy to image the uptake of metal nanoparticles in zebrafish, demonstrating the use of this technique for toxicology studies (Johnston, Scown et al. 2010).

3 A novel high-throughput in vivo vertebrate screening platform for zebrafish larvae

3.1 Introduction

Small size, optical transparency of complex organs and ease of culture make the zebrafish (*Danio rerio*) larva an ideal organism for large-scale in vivo genetic and chemical studies of many processes that cannot be replicated in vitro. Zebrafish models of several human diseases have been developed (Shin and Fishman 2002, Rubinstein 2003, Zon and Peterson 2005, Lieschke and Currie 2007, McGrath and Li 2008). Lead compounds discovered by screening chemical libraries for efficacy in zebrafish disease models have been useful for pharmaceutical discovery owing to the high level of conservation of drug activity between humans and zebrafish (Shin and Fishman 2002, Rubinstein 2003, Zon and Peterson 2005, Lieschke and Currie 2007, McGrath and Li 2008).

Visualizing most zebrafish organs requires manipulating and properly orienting the larvae. Even with confocal or two-photon microscopy, optical access is often impeded by pigmentation, by intervening organs such as eyes and heart or by the highly autofluorescent yolk sac. Current methods to address these challenges involve treatment with the toxic chemical phenylthiourea to suppress pigmentation (Karlsson, von Hofsten et al. 2001), manually transferring zebrafish from multiwell plates or reservoirs and manually orienting them in viscous media such as agar. These processes are too slow and unreliable for high-throughput screens. Molded agar plates can also be used to orient zebrafish (Gehrig, Reischl et al. 2009). However, this is also a relatively coarse process, and it can be done rapidly only for the lateral orientation, whereas imaging many organs (such as brain) requires other orientations. The thick agar molds also prevent high-resolution three-dimensional microscopy and optical manipulations. To improve the throughput and complexity of zebrafish screens, we developed the vertebrate automated screening technology

(VAST) that automatically manipulates and images zebrafish at cellular resolution in three dimensions (Figure 3.1 and Additional Methods).

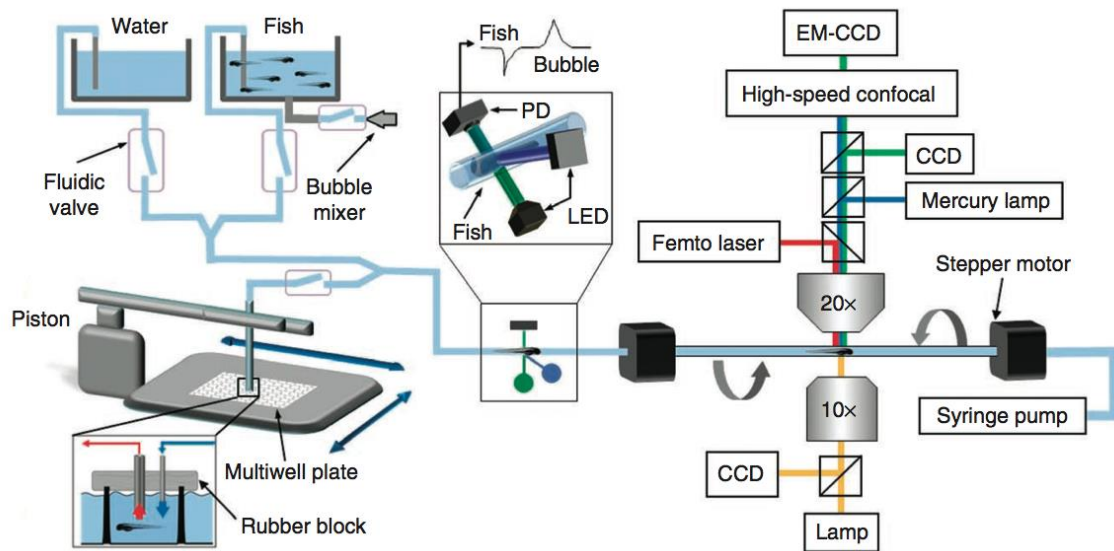


Figure 3.1: Schematic of zebrafish manipulation and imaging platform. Larvae are automatically loaded to the system from either reservoirs or multiwell plates. Reservoirs are connected to the system via fluidic valves and a bubble mixer prevents the larvae from settling. The multiwell plate is located on a motorized x-y stage, which positions individual wells below larva-loading (red arrow) and water-supply (blue arrow) tubes, both held by a silicone rubber block. The block seals the well surfaces as a piston moves the tubes into the wells. A photodetection system including two LEDs and one high-speed photodiode (PD) discriminates the passage of a larva from air bubbles and debris. Two stepper motors hold a capillary along its axis of rotation; this assembly is mounted on a three-axis position stage (not shown) and held between an upright microscope for confocal imaging and an inverted microscope for brightfield imaging. A multifocal confocal head with a cooled electron-multiplying charge-coupled device (CCD) camera and a second large-area CCD connected to the upright port are used for high-speed confocal and widefield fluorescence imaging. A high-speed CCD camera connected to the inverted port allows rapid brightfield detection and positioning of larvae. A femtosecond laser beam used for microsurgery is directed to the upper beam path by a dichroic filter and focused on the sample through the objective.

3.2 Results

3.2.1 Description of the Vertebrate Automated Screening Technology

Each cycle of VAST includes the following steps: loading, detection, positioning, rotation, focusing, imaging, laser manipulation and dispensing. Such capabilities enable both genetic and pharmaceutical cellular-resolution whole-organism screens (Rohde, Zeng et al. 2007) (Figure 3.2). During loading, the system extracts larvae either from a multiwell plate or a reservoir. A high-speed photodetection system composed of a photodiode and two LEDs discerns the entry of larvae into the loading tube. The photodiode senses transmitted light from one LED and scattered light from the other LED. By simultaneously monitoring both the transmission and scattering signals, the system discriminates larva from air bubbles and debris with 100% reliability ($n = 1,000$). After loading and photodetection, the larva moves from the larger loading tube into a capillary (Funfak, Brösing et al. 2007, Buckley, Goldsmith et al. 2008) positioned in the field of view of an optical imaging and manipulation system. The capillary has a refractive index similar to that of water, allowing the use of high-numerical-aperture water-immersion objectives. Using a fast camera and an automated image-processing algorithm, the syringe pump coarsely positions the larva. Next, a three-axis stage automatically moves the capillary assembly to precisely position the larva's head at the center of the field of view. Two stepper motors then orient the larva. Thus, larvae can be positioned and oriented to allow access from any angle. They can also be rapidly reoriented, allowing visualization of organs from multiple angles. At the end of the cycle, larvae can be dispensed back into either individual wells or larger containers by executing the loading process in reverse (Figure 3.7).

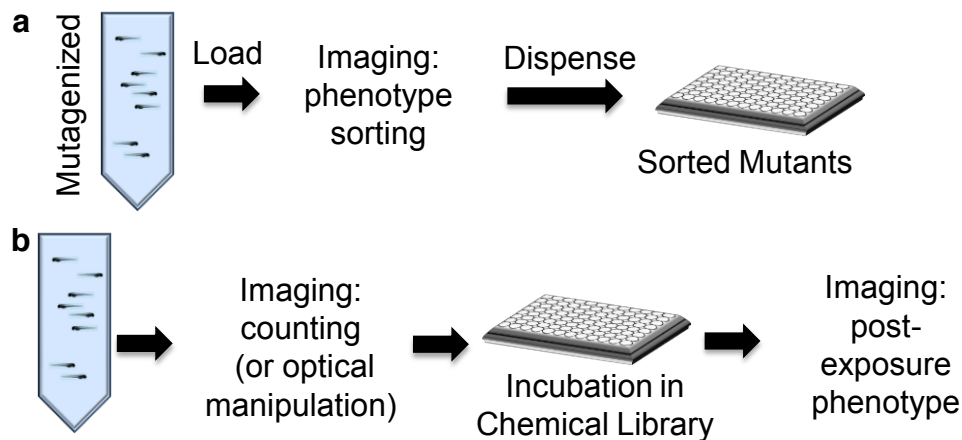


Figure 3.2: Flow diagram for chemical and genetic screens. (a) Genetic screen: Mutagenized animals are loaded from a reservoir to the imaging platform. After imaging, the mutants are sorted into multiwell plates by phenotype. **(b) Chemical screen:** Animals are loaded from a reservoir to the imaging platform, which can be used either to count the number of animals and/or to perform optical manipulations such as laser microsurgery. The animals are then dispensed into multiwell plates containing chemicals to be tested. After incubation within chemicals, the animals are loaded back into the imaging platform to check phenotypes.

Larvae are imaged through two objective lenses: an upright, high-resolution water-immersion objective and an inverted air objective. This allows both widefield fluorescence imaging and high-resolution confocal microscopy. Imaging most phenotypes requires larvae to be oriented at specific angles. For instance, the midline crossing of the Mauthner motor neuron axons that project into the spinal cord is visible only when directly observed from the hindbrain (Figure 3.3a). At less favorable orientations, this structure is obscured.

3.2.2 Proof-of-concept screen: axon misguidance by point mutations in the *robo2* gene

We performed a small-scale test screen on zebrafish with a similar midline-crossing phenotype, the midline crossing of retinal axon projections to the optic tectum (Figure 3.3b and Figure 3.6).

Screening for retinal axon misguidance mutants had previously led to the discovery of astray mutant alleles in the *robo2* gene (Fricke, Lee et al. 2001). Homozygous *robo2*^{ti272z/ti272z} (*ast/ast*) zebrafish do not exhibit proper midline crossing, but the projections are normal in heterozygous *robo2*^{ti272z/+} (*ast/+*) zebrafish. Using our system, we could distinguish wild-type larvae from *robo2* mutants (Xiao, Roeser et al. 2005) with a sensitivity of 100% and specificity of 98.8% for a 96-well plate with 83 randomly seeded mutants. The 1.20% false negative error in identification of *ast/ast* zebrafish was due to the rare cases of mutants with strong phenotypic similarity to the wild type. The system could thus be used for large-scale chemical screens for small molecules that rescue such misguidance.

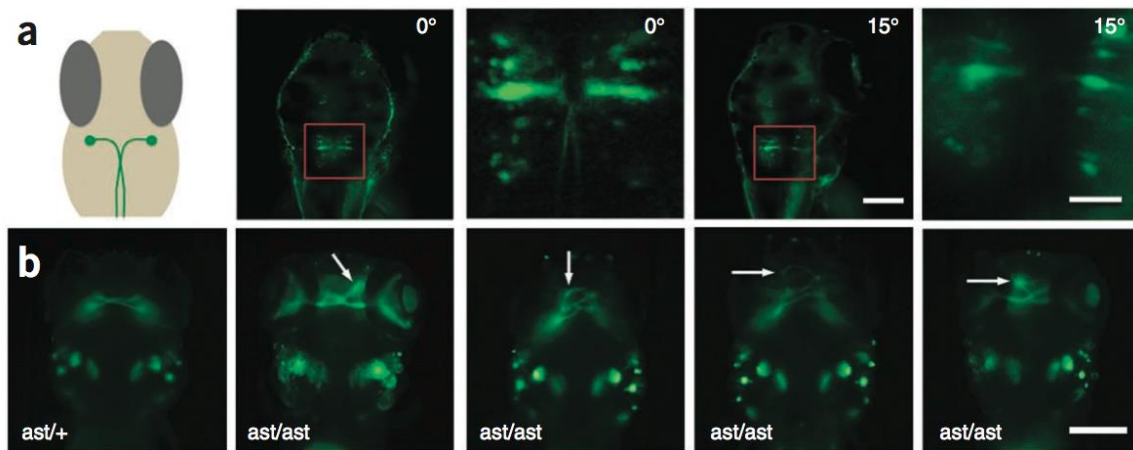


Figure 3.3: Orientation, imaging and screening of zebrafish larvae. (a) Schematic showing the midline crossing of Mauthner axons (left) and confocal images of GFP-expressing Mauthner cells at 0° and 15° (right). Magnified versions of boxed areas are shown to the right of each image. (b) Widefield fluorescence images illustrating the phenotypes distinguished in a small-scale test screen. Representative images showing GFP-labeled axons of retinal ganglion neurons projecting to the optic tectum in larvae of the indicated genotypes. Arrows point to the misguided projections. Scale bars, 150 μ m (50 μ m in magnified images in a).

3.2.3 Laser ablation of single neuron fibers

In conjunction with sample positioning and orientation, VAST also allows *in vivo* optical manipulations such as localized activation of fluorescent reporters and ion channels, uncaging of compounds and femtosecond laser microsurgery (Steinmeyer, Gilleland et al. 2010) with

subcellular precision. We used this system to monitor neuronal regeneration (Bhatt, Otto et al. 2004) after injury by laser microsurgery (Yanik, Cinar et al. 2004) (Figure 3.4). The lateral-neuron axon fiber bundle projecting along the trunk of a larva is visible when the larva is laterally oriented. We axotomized the bundle by focusing near-infrared femtosecond laser pulses using the following semiautomatic process: A user selected a cell body by clicking on a graphical user interface; an algorithm then measured the user-specified distance from the cell body to the point of axotomy along the axon; and the position stage automatically moved the selected axonal region to the focal spot of the laser for axotomy. We imaged regenerating axonal fibers at 18 h and 24 h after axotomy (Figure 3.4a). The laser pulses were delivered with high precision (1.7 μm) (Steinmeyer, Gilleland et al. 2010), and the subsequent response of the tissue to the laser (immediate retraction of nerve fibers) showed some variability, leading to a distribution of cut sizes (8.1 \pm 5.5 μm , \pm s.d., $n = 30$; Figure 3.4b). All zebrafish recovered from surgery within 30 min with no apparent morphological abnormality, and 100% of the zebrafish survived 24 h after surgery ($n = 30$).

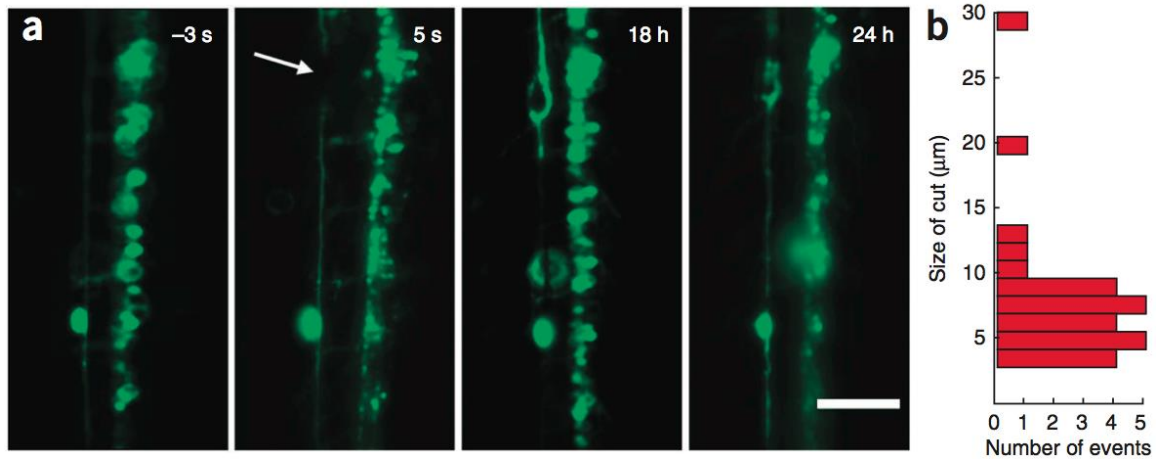


Figure 3.4: Laser microsurgery and neuronal regeneration. (a) Widefield fluorescence images of enhanced GFP (EGFP)-expressing lateral-neuron axon fibers in a 3-d.p.f. larva are shown at the indicated times before and after axotomy. Scale bar, 75 μm . (b) Distributions of laser cut sizes ($n=30$).

3.2.4 Timings for each screening step

A complete cycle of loading, positioning, cellular-resolution imaging and dispensing a zebrafish took less than 16 s (Table 4). Axotomy required an additional 2.1 s on average. Screening an entire multiwell plate took 31.85 min with an average of 19.9 s per well, which included the additional interval for retracting, moving and inserting the loading apparatus, and sealing the wells. Zebrafish could also be loaded and imaged multiple times for time-lapse assays. Performed manually, assays of similar complexity require about 10 min per zebrafish, and the assays are error-prone.

Table 4: Average duration of screening steps for VAST.

| Step | Time (sec) |
|--|---------------|
| Loading | |
| from multiwell plate | 2.1 ± 0.4 |
| from reservoir | 2.2 ± 0.3 |
| From photodetector to field-of-view | 2.7 ± 0.3 |
| Positioning | 2.9 ± 0.6 |
| Orienting & focusing | 5.6 ± 1.7 |
| Microsurgery | 2.1 ± 0.5 |
| Unloading | 2.5 ± 0.1 |
| <i>Accumulative time calculated for loading and unloading from a multiwell plate. Values in parenthesis include microsurgery time. n = 150 in total.</i> | |

3.2.5 Health Assessment

Zebrafish larvae are delicate and particularly susceptible to injury by tearing at sharp edges or by deformation. The most substantial potential for damaging larvae occurred as they entered the loading tube at the high aspiration rates needed to achieve the desired throughput. To lessen this risk, we started the flow at a low initial rate and increased it at an acceleration of $42 \mu\text{l s}^{-2}$ until a larva was detected by the high-speed photodetector. The maximum flow rate was limited to $330 \mu\text{l s}^{-1}$. At this maximum rate, no injury occurred while larvae were traveling in the tubing. After a larva was detected by the photodetector, the control software decreased the aspiration rate to $83 \mu\text{l s}^{-1}$ to allow automated recognition of the zebrafish by the camera.

We assessed the health of 450 larvae screened at 2 days post-fertilization (d.p.f.) at three different initial aspiration rates (Figure 3.5a). The assessment was based on both functional and morphological criteria. At all flow rates, heartbeat and touch response matched those of controls. We never observed yolk tearing ($n = 450$). At the highest initial flow rate of $330 \mu\text{l s}^{-1}$, 2% of zebrafish exhibited morphological abnormalities. With a slightly slower initial aspiration rate (increasing the screening time by approximately 1 s), all health criteria matched those of controls (Figure 3.5a). We measured postmanipulation developmental delay by monitoring the time of appearance of the swimming bladder. There was no significant difference between the development of larvae that were manipulated by the system and control zebrafish ($p = 0.94$), even at the highest flow rates (Figure 3.5a). Among the different larval age groups tested (2–7 d.p.f., $n > 100$ per age), we observed no difference in health.

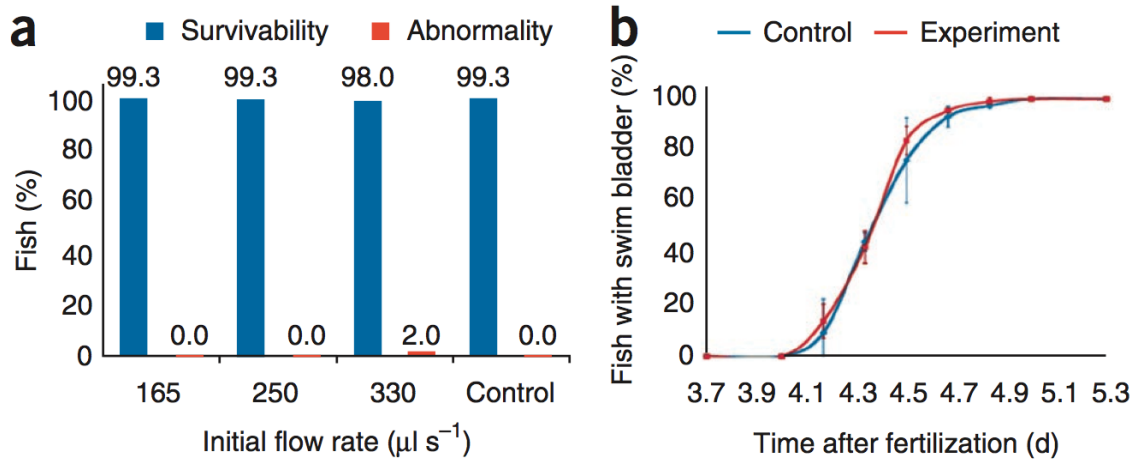


Figure 3.5: Quantitative assessment of zebrafish health. (a) Survival and abnormality of larvae as a function of initial flow rate ($n = 150$ for each rate). (b) Appearance time of swim bladder in screened and control fish (one way ANOVA, $p = 0.94$, average of three independent experiments with 50 fish analyzed in each; error bars, s.d.; $n = 3$).

3.3 Methods

3.3.1 Components of the high-throughput screening platform

The system can load larvae from reservoirs or multiwell plates (Figure 3.1). The multiwell plate loading stage consists of 3 linear precision motors (RCA2, Intelligent Actuators). The motors are controlled by RACON 20/30 drivers (Intelligent Actuators). The loading head consists of a larva-loading and a water-supply metal tubes with inner diameters of 1.0 and 0.2 mm, respectively (New England Small Tubing Inc.) inserted into a silicone rubber block. The silicon rubber block is pressed (by the loading stage motor) against the top of the multiwell plate to seal the wells. One tube aspirates the larva from the sealed well while the other tube injects water. Two fluidic valves (075P2NC12, Bio-Chem Fluidics) are used to switch the flow between the reservoirs and multiwell plate by pinching the silicone tubing (1/32" ID x 3/32" OD, Bio-Chem Fluidics). Larvae are driven through the system using a syringe pump (Carvo XLP6000, Tecan Systems). The photodetection system consists of a photodiode IC (OPT301, Texas Instruments) and two LEDs (Cree Inc) aligned in transmission and reflection configurations as shown. The photodiode IC contains an integrated amplifier. Two precision stepping motors (KP35FM2-044, Japan Servo Co.) hold a capillary of diameter 800 μ m along its axis of rotation. The motors are controlled by a microstepping driver (BSD-02LH, Interinar Electronics). The motor and capillary assembly is mounted on a 3-axis precision stage (MP-200, Sutter Instrument) with 0.04 μ m resolution along each axis. Two NiDAQ input/output data cards (PCI-6512 and PCI-6259, National Instrument) installed in a DELL OptiPlex computer control the fluidic valves, stepping motors, and read out the voltage across the photodetector.

3.3.2 Components of the imaging system

The imaging system consists of a dual (upright/inverted) microscope (Eclipse Ti, Nikon (inverted), Nikon 90i Digital Imaging Head (upright)) with two light sources (Mercury lamp, Nikon). The top port of the upright microscope is equipped with a multi-beam laser confocal scanning head (Infinity 3, VisiTech) with a 1004 x 1002 pixel EMCCD camera (iXon+885, Andor Technology) for

high-speed confocal imaging. For high-speed image sectioning, a piezo actuator with 400 μm travel distance (P-725 PIFOC, Physik Instrumente) holds either a 10x (NA = 0.5), 16x (NA = 0.8), or 20x (NA = 1.0) water immersion lens (Nikon). A high-speed CCD camera (GX-1050, Prosilica) is connected to the inverted microscope equipped with 10 \times air objective lens for larva detection, position, and rotation.

3.3.3 Animals

The fluorescent retinal ganglion line (*astray*^{ti272z} with *brn3c:gap43-gfp*), the fluorescent lateral neuron line, and the fluorescent mauthner line (*ETj1282b:GFP*) were maintained and crossed using standard techniques. All animal experiments were approved by MIT's Committee on Animal Care under protocol numbered 0309-025-12.

3.3.4 Axon guidance screen

Genotypically homozygous *+/+* and *ast/ast* fish were crossed to generate *ast/+* larvae. A 96-well plate was randomly and partially populated with the heterozygous *ast/+* progeny. The rest of the wells were populated with the homozygous progeny of *ast/ast* fish. A blind screen was performed by loading the animals from multi-well plates and orienting them to visualize midline crossing as in part (a) by a 10 \times (NA = 0.5) objective lens with long depth-of-focus in wide-field fluorescence imaging mode. Animals were blindly classified according to the observed phenotype.

3.3.5 Laser axotomy

A tunable femto-second laser (Mai Tai, Spectra-Physics Lasers) is guided to the upright microscope for laser axotomy as we previously described (Steinmeyer, Gilleland et al. 2010). The axon fiber of GFP-expressing lateral neuron is cut 850 μm distance from the soma using ultrashort laser pulses with 780 nm wavelength, 100 fs duration, 12.7 nJ pulse energy, 80 MHz repetition rate, and 10 ms long pulse train focused by a 20 \times (NA = 1.0) objective lens. Statistics of laser cut sizes were quantified with 40 \times (NA = 0.8) objective lens. Surgeries were repeated on $n = 30$ animals with 100% success rate.

3.3.6 Assessment of animal health

The syringe was operated at three different initial aspiration rates of 165, 250, and 330 $\mu\text{l}\cdot\text{s}^{-1}$ for loading 2 dpf larvae from multiwells. $n = 450$ larvae in total were anesthetized with 0.20 $\text{mg}\cdot\text{ml}^{-1}$ Tricaine, loaded, and dispensed from the platform. A control group of $n = 150$ larvae from the same breed were similarly anesthetized. Health assessment was based on both functional and morphological criteria measured at $t = 0, 12, 16, 20, 24, 28, 32$ and 36 hours post screening. Functional criteria included visual confirmation of normal heartbeat, and reflex response to touch stimuli. Morphology criteria included bending (i.e. lordosis, kyphosis, and scoliosis) and craniofacial abnormalities. The criteria included those injuries even if the animals regenerated later.

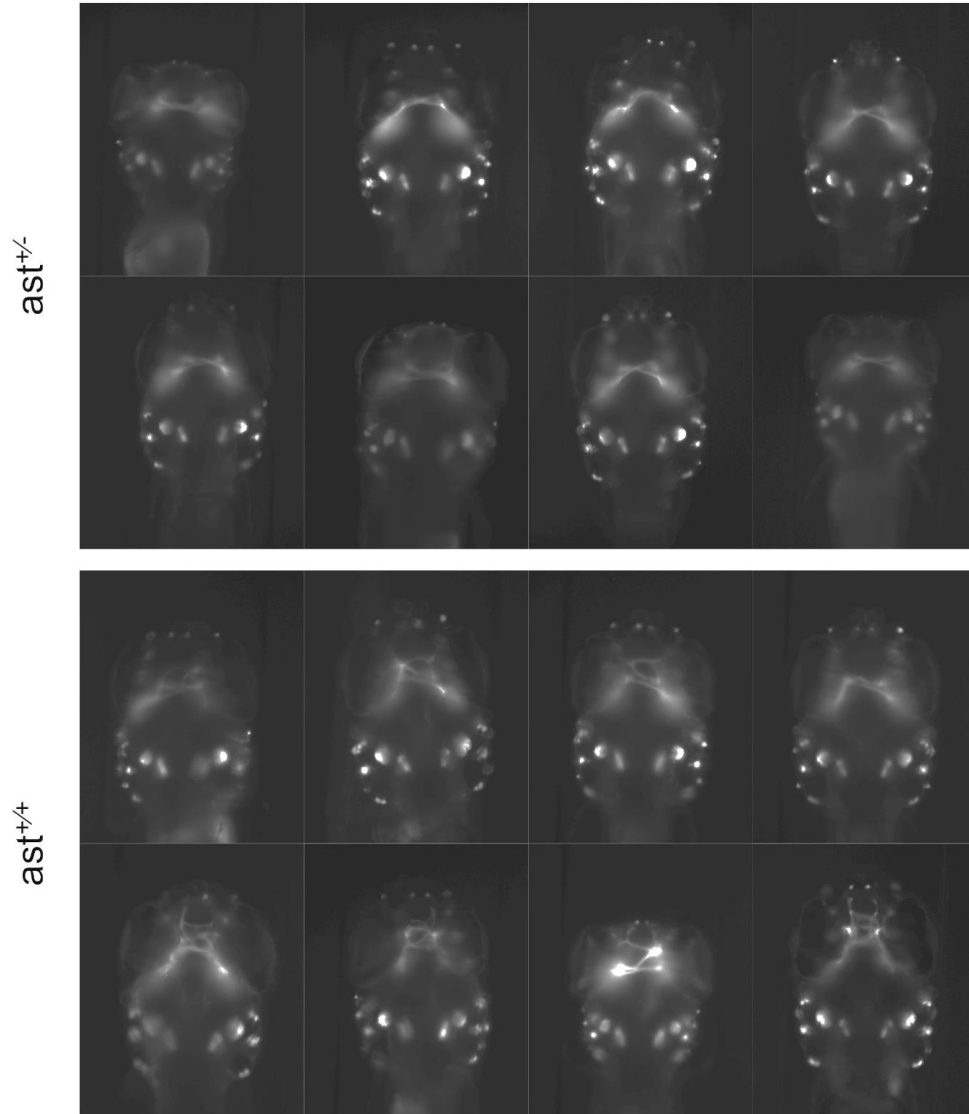


Figure 3.6: Representative images of zebrafish larvae with wild-type ($ast^{+/+}$) versus astray ($ast^{+/+}$) phenotype. Genotypically homozygous $ast^{+/+}$ and $ast^{+/+}$ fish were crossed to generate the $ast^{+/+}$ larvae shown.

3.3.7 System architecture and operation:

3.3.7.1 Imaging and laser axotomy

The imaging system (Figure 3.1) consists of a dual (upright/inverted) microscope (Eclipse Ti, Nikon (inverted), Nikon 90i Digital Imaging Head (upright)) with two light sources (Mercury lamp, Nikon). The upright microscope's top port is equipped with a multi-beam laser confocal scanning

head (Infinity 3, VisiTech) with a 1004 x 1002 pixel EMCCD camera (iXon+885, Andor Technology) for high-speed confocal imaging. For high-speed image sectioning, a piezo actuator with 400 μm travel distance (P-725 PIFOC, Physik Instrumente) holds either a 10x (NA = 0.5), 16x (NA = 0.8), or 20x (NA = 1.0) water immersion lens (Nikon). A tunable femto-second laser (Mai Tai, Spectra-Physics Lasers) is guided to the upright microscope for laser axotomy as we previously described (Steinmeyer, Gilleland et al. 2010). A high-speed CCD camera (GX-1050, Prosilica) is connected to the side port of the inverted microscope for larva detection, position, and rotation.

3.3.7.2 Capillary stage

Two precision stepping motors (KP35FM2-044, Japan Servo Co.) hold a capillary along its axis of rotation (Figure 3.1). The motors are controlled by a microstepping driver (BSD-02LH, Interinar Electronics). The motor and capillary assembly is mounted on a 3-axis precision stage (MP-200, Sutter Instrument) with 0.04 μm resolution along each axis.

3.3.7.3 High-speed photodetection

The photodetection system (Figure 3.1) consists of a photodiode IC (OPT301, Texas Instruments) and two LEDs (Cree Inc) aligned in transmission and reflection configurations as shown. The photodiode IC contains an integrated amplifier.

3.3.7.4 Multiwell plate/ reservoir loading

The system can load larvae from reservoirs or multiwell plates (Figure 3.1). The multiwell plate loading stage is comprised of 3 linear precision motors (RCA2, Intelligent Actuators). The motors are controlled by RACON 20/30 drivers (Intelligent Actuators). The loading head consists of two tubes (New England Small Tubing Inc.) inserted into a silicone rubber block. The silicon rubber block is pressed (by the loading stage motor) against the top of the multiwell plate to seal the wells. One tube aspirates the larva from the sealed well, while the other tube injects water.

3.3.7.5 Fluidic pumps and switches

Larvae are delivered to the capillary under the objective lens through a syringe pump (Carvo XLP6000, Tecan Systems). Two fluidic valves (075P2NC12, Bio-Chem Fluidics) are used to switch the flow between the reservoirs and multiwell plate by pinching the silicone tubing (1/32" ID x 3/32" OD, Bio-Chem Fluidics).

3.3.7.6 Computer interface and control

Two NiDAQ input/output data cards (PCI-6512 and PCI-6259, National Instrument) are mounted in a DELL OptiPlex computer to control the fluidic valves, stepping motors, and to read out the voltage across the photodetector. The control software is written in Matlab.

3.3.7.7 Algorithm for Operation Sequence

The detailed algorithm for operation sequence of the system is shown in the flowchart of Figure 3.7. The rectangles, parallelogram, and rhomboids represent the actions, measurements, and conditionals, respectively.

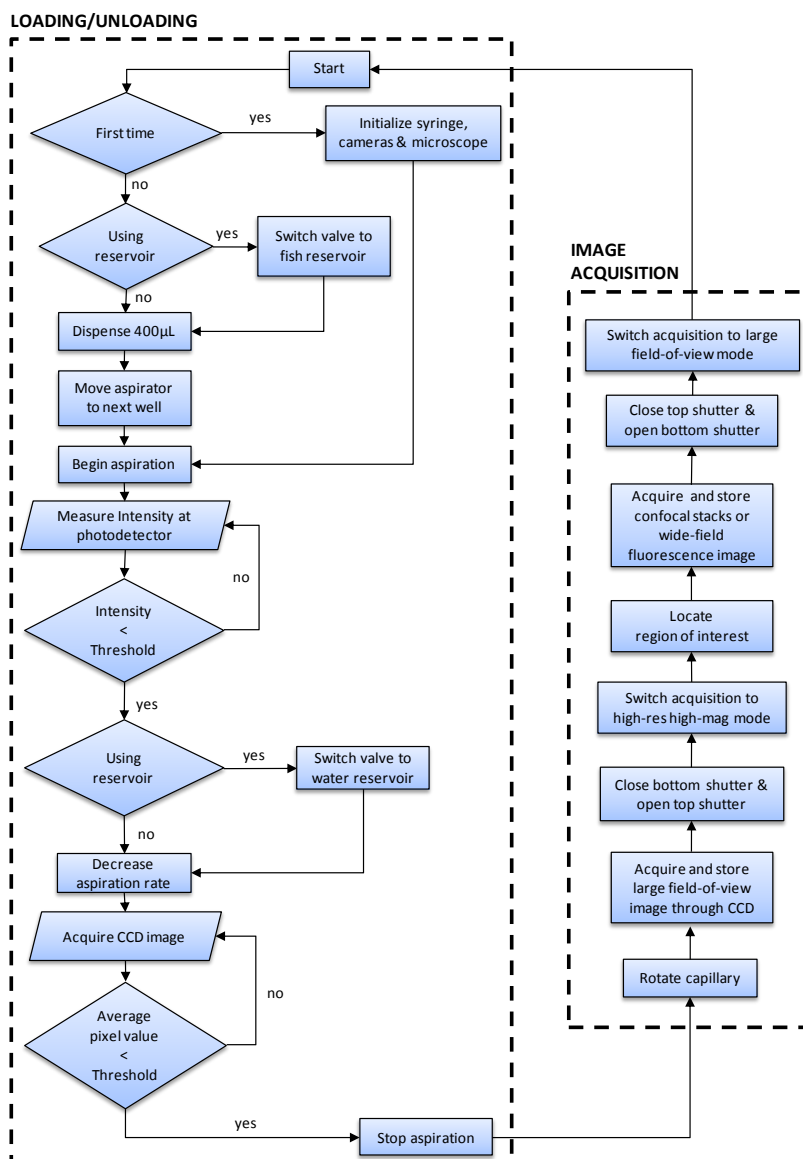


Figure 3.7: Flowchart showing the algorithm for the operation sequence of the system. See supplementary text for further details.

The system starts by initializing syringe pumps, cameras, lamps, shutters, position stages, and motors. The fluidic valves (Figure 3.1) are switched to the source of fish i.e. either multiwell plate or fish reservoir. The larva is aspirated from the selected source at a constant rate of acceleration of $42 \mu\text{l s}^{-2}$ up to a maximum speed of $330 \mu\text{l s}^{-1}$. The photodetector is continuously sampled at 2 kHz rate via the NiDAQ PCI-6259 card until the intensity reading crosses a pre-determined threshold (the value of threshold is calibrated in advance by trial and error). Upon detection of the

larva the fluidic valve is switched to the water reservoir if the larva is being loaded from the fish reservoir. The aspiration rate is subsequently decreased to $83 \mu\text{l s}^{-1}$ to avoid damaging the larva at the entrance of the capillary. The high-speed CCD at the bottom port is continuously reading at $100 \text{ frames s}^{-1}$. The pixel intensity is averaged over the entire field-of-view, and compared to a pre-determined threshold (value of threshold is calibrated in advance by trial and error). When average pixel intensity drops below the threshold, the aspiration is stopped.

The capillary is then rotated via the motors until the larva is at the desired orientation. A large field-of-view image of the gross morphology of the larva is acquired and stored by the CCD at the bottom port. The motorized shutter of the inverted microscope (i.e. bottom shutters) is closed while that of upright microscope (top shutters) is opened. The image acquisition is switched from the bottom CCD to either the top CCD or the high-speed scanning confocal head equipped with EMCCD. Guided by fluorescence imaging, the region of interest is located. Either confocal stacks or wide-field fluorescence images are acquired. The top shutter is closed, and the bottom shutter opened. The image acquisition is switched to the bottom port. The system is now ready for the next cycle of operation.

3.4 Discussion and Summary

We have here demonstrated a high-throughput vertebrate screening platform with cellular-resolution imaging and manipulation capabilities that should permit large-scale in vivo study of complex processes such as organ development, neural degeneration and regeneration, stem cell proliferation, cardiovascular, immune, endocrine and nervous system functions, pathogenesis, cancer and tissue specificity and toxicity of drugs.

4 Improved and fully automated vertebrate screening platform with parallel animal processing

4.1 Introduction

The most fundamental challenge limiting the scale of zebrafish studies and screens has been the absence of methodologies for rapid manipulation and imaging. High-resolution imaging requires researchers to immobilize and manually orient each individual larva. Typically this is done by mounting specimens in methylcellulose or low-melting-point agarose, a cumbersome process that takes 5-15 minutes per animal depending on the complexity of the experiment. Although some published screens have involved large numbers of animals (Tran, Sneed et al. 2007, Gehrig, Reischl et al. 2009, Kokel, Bryan et al. 2010, Rihel, Prober et al. 2010, Carvalho, de Sonneville et al. 2011), these have been limited to highly specific or low-content assays.

In the last chapter we described the vertebrate automated screening technology (VAST) that allows, for the first time, high-speed screening of zebrafish larvae at cellular resolution (Pardo-Martin, Chang et al. 2010). As described in the previous chapter VAST can process each larva within 20 seconds and an entire multiwell plate within 35 minutes. This technology, thus presents a significant increase over previous art and enables, for the first time, to exploit the complexities of the zebrafish larvae at sufficient throughputs. However, there are considerable advantages to further accelerating zebrafish assays and fully automating the screening process (Tamplin and Zon 2010).

In this chapter, I will describe novel technologies that significantly increase the throughput of VAST by simultaneously processing multiple fish. Under these conditions, the system throughput becomes limited only by the image acquisition speed rather than by the fluidic and mechanical processes. We also demonstrate image recognition algorithms that fully automate zebrafish manipulation steps such as positioning and orienting animals. In addition, we have analyzed

several capillary materials in order to identify the one with the best optical properties for distortion-free, low-background, cellular-resolution imaging of zebrafish.

This chapter thus builds on the previous one to present a more robust and improved screening system. By limiting the throughput to image acquisition we trivialized the sample preparation steps.

4.2 Results

4.2.1 Multi-thread Vertebrate Automated Screening Technology

The multi-thread VAST system loads larvae automatically from a 96-well nylon mesh plate that fits into a matching 96-well tray (MultiScreen-Mesh Plate, Millipore Inc.). The multiwell plate is brought into position by a three-axis motor stage (RCA2, Intelligent Actuators). The mesh-filter insert allows easy transfer of larvae. In order to keep the water level constant, two tubes separately aspirate and dispense water (Figure 4.1 insert A) via the syringe pump. Larvae are detected as they pass through the high-speed zebrafish discriminator, which distinguishes larvae from air bubbles and debris and also differentiates fluorescent from non-fluorescent larvae. The design of the zebrafish discriminator is discussed in detail below. Two high-precision step motors (KP35FM2-044, Japan Servo Co.) hold an ultra-thin glass capillary along its axis of rotation. The capillary has an outer diameter of 700 μm and a wall thickness of 10 μm (BGCT 0.7, Capillary Tube Supplies) and is immersed in a water bath to minimize the index of refraction mismatch. The assembly (i.e. motors, capillary and water bath) is mounted on a three-axis position stage (MPC-200, Sutter Instrument) and held between an upright microscope for epi-fluorescence (and confocal) imaging and an inverted microscope for bright-field imaging. The inverted microscope is connected to a high-speed CCD (GX-1050, Prosilica) and is primarily used to detect, position, and rotate the larvae. A high-speed confocal head (Infinity 3, VisiTech Inc.) with a cooled EM-CCD (iXon+885, Andor Technology) is used for confocal imaging. The fluidic elements are controlled by three pinch valves (075P2NC12, Bio-Chem Fluidics) and three computerized syringe pumps (XLP 6000, Tecan). Fluidic components are connected through silicone tubing

(0.8 mm inner diameter, Bio-Chem Fluidics). The entire system is controlled via a code written in MATLAB.

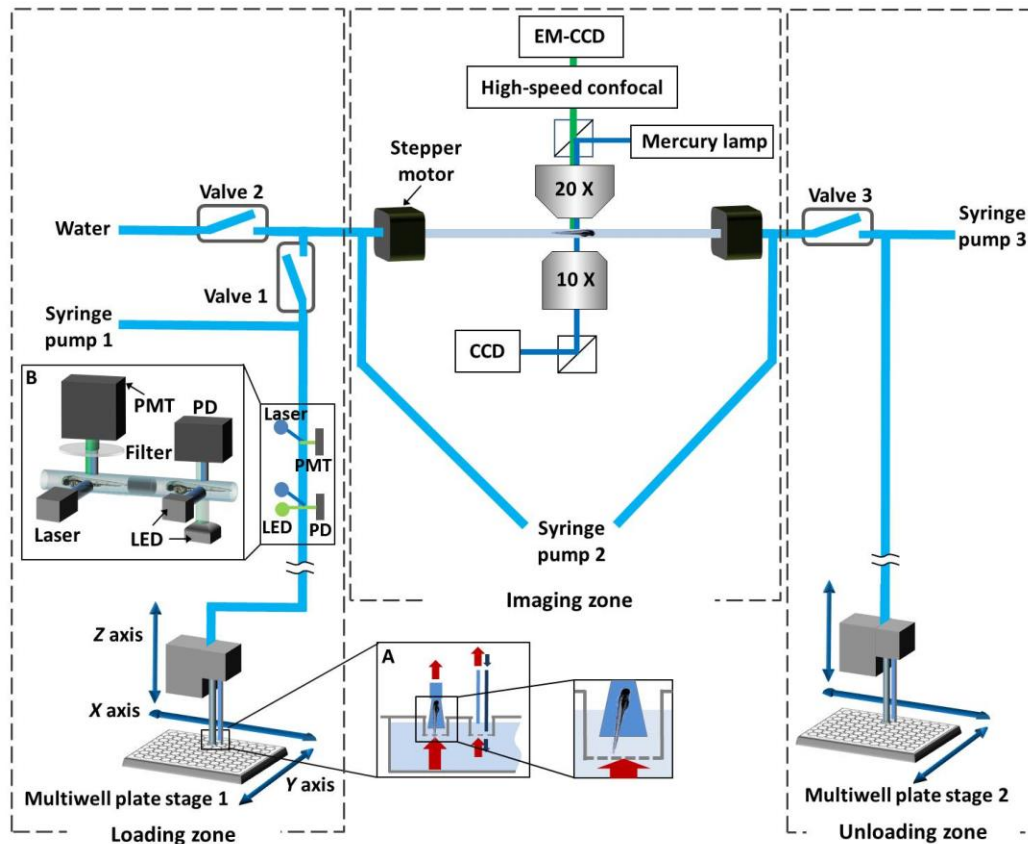


Figure 4.1: Multi-thread Vertebrate Automated Screening Technology (VAST). The platform consists of three subsystems that operate simultaneously: loading, imaging, and unloading. Larvae are automatically loaded to the platform from individual wells of a mesh-filter multiwell plate positioned by a motorized x–y stage. The mesh-filter insert allows easy transfer of larvae into the system. In order to avoid a drop in the fluid level (while larva is being aspirated by the loading nozzle), a circulator is set nearby the loading nozzle (inset A) that consists of a fluid source and an aspirator where the tip of the aspirator is slightly elevated than the tip of the fluid source. A zebrafish discriminator with a brightfield and a fluorescence photodetection system (inset B) discriminates the passage of fluorescent larvae from non-fluorescent ones, air bubbles and debris. Two step motors hold a capillary immersed in a water bath along its axis of rotation; this assembly is mounted on a three-axis position stage (not shown) and held between an upright microscope and an inverted microscope. A multifocal confocal head with a cooled electron-multiplying charge-coupled device (EM-CCD) camera and a second large-area charge-coupled device (CCD) are used for high-speed confocal and wide-field fluorescence imaging, respectively. A high-speed CCD camera connected to the inverted microscope allows rapid bright-field imaging for positioning and orienting the larvae.

4.2.2 Multi-thread Operation

The multi-thread VAST system simultaneously performs three independent operations to enable parallel processing of multiple fish; loading, imaging, and unloading. At the beginning of each cycle, a larva is acquired from a multiwell plate by syringe pump 1 and the zebrafish discriminator is activated to distinguish the contents of the flow (i.e. larvae versus debris or bubbles). After the discriminator detects a larva, pinch valve 1 is opened and syringe pump 1 is stopped, allowing the larva to transit from the loading module to the imaging module. The larva is transported into the imaging module via syringe pump 2 after the flow direction is changed by switching pinch valves 2 and 3. The loading module continuously repeats these steps and each loading cycle takes 4 seconds to complete. In the imaging module, the larva is automatically positioned, rotated, and imaged inside the capillary, which takes 9.6 seconds on average. The timing for imaging was calculated for a single wide-field fluorescence acquisition with a 300 ms exposure time. The larva is then moved to the unloading module and a new larva is transported into the capillary from the loading module. The larva in the unloading module, (held between valve 3 and the imaging module), is then transferred into its corresponding well of the output multiwell plate. Each unloading cycle takes 3.4 seconds and dispenses 500 μL of medium with a flow rate of 165 $\mu\text{L}/\text{sec}$. Timing analysis is based on trials of $n=192$ animals. As reported previously, over 98% of larvae imaged by VAST survive and develop without noticeable morphological abnormalities (Pardo-Martin, Chang et al. 2010). By multi-threading the loading, imaging and unloading operations, throughput becomes limited only by the slowest operation (i.e. the imaging step; 9.6 seconds), rather than by the total time required to carry out all processes (Figure 4.2).

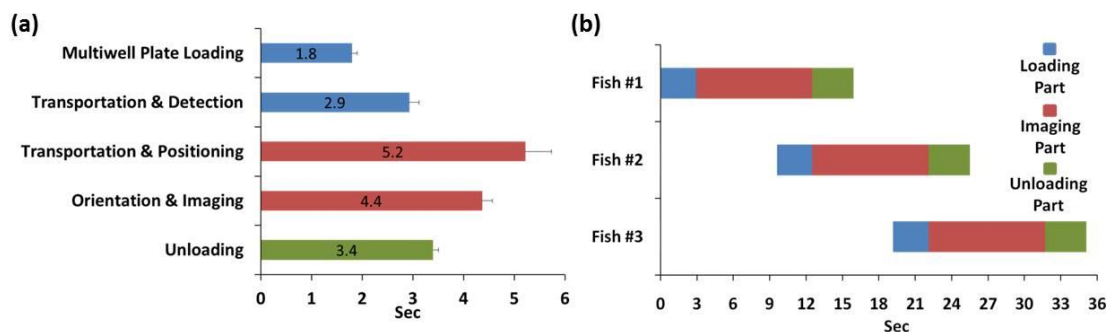


Figure 4.2: Timings of multi-thread processing of zebrafish. Blue, red, and green bars indicate the processes comprising loading, imaging, and unloading, respectively. (a) The time required for each handling step ($n = 192$). Multiwell plate loading process includes positioning the multiwell plate and the nozzle, and aspirating a larva into the tube from the multiwell plate. Transportation time is the duration it takes to move a larva within the fluidic tube from one point to another. (b) Multi-thread operation: The system simultaneously performs loading, imaging, and unloading operations with three different larvae. As a result, the overall processing time is dictated solely by the duration of the slowest process (i.e. imaging; 9.6 sec), not by the total duration of all processes.

4.2.3 Fluorescence/bright-field automated zebrafish discriminator

A low-cost, high-performance discriminator (Figure 4.3a) is used to distinguish larvae from debris and air bubbles and to separate fluorescent and non-fluorescent larvae. The discriminator is formed by a bright-field photodetection system and a fluorescence-activated larva sorter. The bright-field photodetection system is comprised of an integrated photodiode and an amplifier chip (OPT301, Texas Instruments) and two LEDs aligned in transmission and refraction/scattering configurations. The fluorescence-activated sorter consists of an epi-fluorescence detection system with a GFP filter set, a 10X lens, a photo-multiplier tube (PMT), and a mercury light source. By simultaneously measuring transmitted light and refracted/scattered light at different wavelengths, this device can reliably discriminate between larvae, debris, and air bubbles based on the refraction/transmission ratio of different objects (Figure 4.3b). The transmitted light can largely pass through the fluidic tube when the tube is filled with solution. When an object or bubble crosses the light path, the light is absorbed/refracted/scattered and therefore the transmission light intensity received by the photodiode decreases. A live larva tends to absorb

light more than scattering it, while a dead larva, debris, or bubble tend to scatter light more than transmit it. To balance the scattered and transmitted light intensity on the detector, we use two LEDs where one is in the transmission path and the other is in the orthogonal scattering path. LEDs with different emission colors are used to aid the alignment of the refraction/transmission ratio. Although the scattered light intensity is significantly lower, the intensity of the LEDs did not require any tuning because of the significant difference in the spectral responsivity of the photodiode to the LEDs' colors. Such discrimination of multicellular organisms has traditionally been performed with more complicated setups and image processing algorithms. The reliability of our discriminator was tested under a variety of flow rates, ranging from 165 $\mu\text{L}/\text{sec}$ to 495 $\mu\text{L}/\text{sec}$ (Figure 4.3c). For the flow rates that we use in screening (330 $\mu\text{L}/\text{sec}$), the reliability is near 100%.

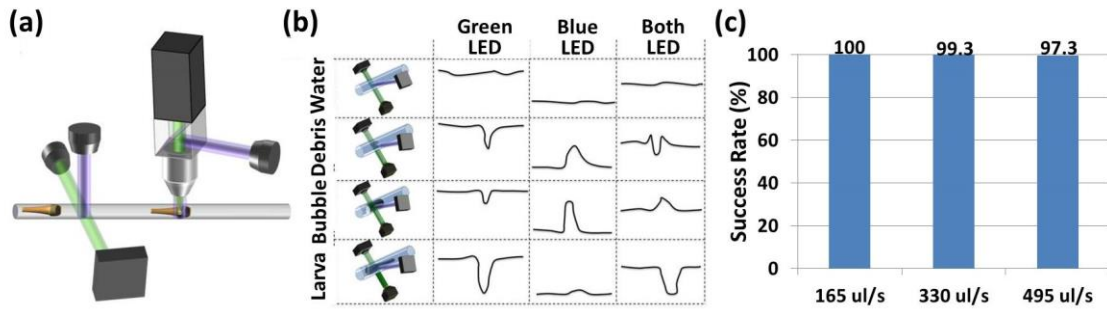


Figure 4.3: Zebrafish discriminator. (a) Schematic representation of the zebrafish discriminator. The system is composed of a bright-field discrimination system and a fluorescence-activated zebrafish sorter. (b) Schematic representation of the mechanism of action of the bright-field discrimination system. By combining both the refracted/scattered and transmitted signals the system distinguishes a zebrafish larva from air bubbles and debris. (c) Detection and discrimination reliabilities at increasing flow rates. The reliability is near 100 % at normal operating speeds of 330 $\mu\text{L}/\text{s}$. ($n=150$).

4.2.4 Automated identification of zebrafish orientation and position

A key step in the design of VAST is the automation of the fine positioning of the region of interest (ROI) within the relatively small field-of-view (FOV) of the high power objective lenses used for cellular-resolution imaging. To accurately and consistently image the same ROI across many larvae, it is necessary to precisely control both position along the length of the capillary and

orientation/rotation around the fixed axis of the capillary. Due to the phenotypic variations that can occur in large-scale genetic and chemical screens, a reliable and flexible algorithm is crucial.

Our algorithm works through a four-step process; coarse positioning of the larva under the FOV, calculation of the direction of its entry into the capillary, identification of its orientation and rotation, and fine positioning of the ROI within the FOV of the high power objective lens.

The coarse positioning of the larvae in the center of the FOV is done through a closed loop feedback between the CCD imaging the FOV and the computer-controlled syringe pump as previously described (Pardo-Martin, Chang et al. 2010, Pardo-Martin, Chang et al. 2010) .

Larvae can enter the capillary in either a head- or tail-first orientation. For this reason, the longitudinal (head vs. tail) orientation of the larvae has to be identified before any image processing steps are performed. A 1D pixel intensity profile $f(x)$ for the fish can be computed by summing the pixel intensities across the axis orthogonal to the main tube axis. The center of mass (of pixel intensities), CM , of the larvae is computed by summing the position values weighted by the normalized 1D intensity profile (Equation 1).

Equation 1: Centre of mass

$$CM = \frac{\sum_{x=1}^n f(x)x}{\sum_{x=1}^n f(x)}$$

The largest intensity variation between the zebrafish and surrounding water/tubing occurs at the very tip of the head, x_0 , which is identified by finding the position of maximum value of f' , the derivative of the 1D intensity profile. The center of mass falls in the upper part of the abdomen, and therefore the orientation of the larvae can be found by comparing the geometrical center to the center of mass of the fish (Equation 2).

Equation 2: Decision rule for animal orientation

$$D = \begin{cases} 1, & CM - x_0 > 0 \\ 0, & CM - x_0 = 0 \\ -1, & CM - x_0 < 0 \end{cases}$$

Where $D = 1$ ($D = -1$) means that the head is towards left (right).

We next identify the lateral orientation of the larva. Due to the anatomical symmetry and optical transparency of the larvae, it is unreliable to identify the lateral orientation based only on the ventral and dorsal views (Figure 4.4a). Instead, we acquire a series of 2D images of the larva $f(x, y)$ at a constant frame rate of 180 frames per second (fps) while rotating the capillary 360 degrees at a constant rotation speed (Figure 4.4b). Using the frame acquisition rate and rotation speed, a rotation angle is assigned for each acquired frame. We then compute the cross correlation (Lewis 1995), CC , between each frame and predefined template intensity distributions $t(x, y)$ of age-matched larvae imaged at dorsal and lateral views using the following relationship (Equation 3):

Equation 3: Cross correlation of images to the reference template

$$CC(f, t) = \max_{u,v} \left(\frac{\sum_{x,y} [f(x, y) - \bar{f}_{u,v}] [t(x - u, y - v) - \bar{t}_{u,v}]}{(\sum_{x,y} [f(x, y) - \bar{f}_{u,v}]^2 \sum_{x,y} [t(x - u, y - v) - \bar{t}_{u,v}]^2)^{\frac{1}{2}}} \right)$$

Where $\bar{f}_{u,v}$ and $\bar{t}_{u,v}$ are the average pixel values for the image and template, respectively. The cross-correlation with the dorsal template yields two narrow peaks at the dorsal and ventral orientations (Figure 4.4c). However, these peaks alone are insufficient to distinguish between dorsal and ventral sides. The cross-correlation with the lateral template yields a single wider peak that identifies the right versus left side of the fish. This knowledge of left/right orientation and the direction of rotation are then used to differentiate which peaks from the dorsal template corresponds to the ventral vs. dorsal orientations. To handle phenotypic variation across larvae, we have constructed a collection of templates for larvae under the typical morphological abnormalities (e.g. pericardial edema). When the maximum cross correlation between the templates and the larva does not exceed a user defined minimum, our algorithm looks through this collection of templates and recalculates the orientation using the template with the highest correlation. If the cross correlation does not reach a user-defined threshold for any template, the larva is discarded. The reliability of the orientation algorithm is 99 % ($n=100$ larvae).

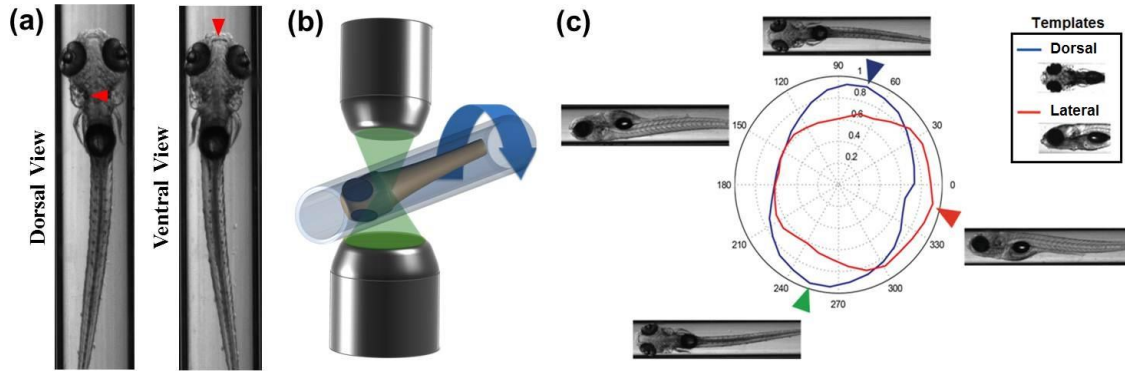


Figure 4.4: Identification of the angle and position of larvae. (a) Dorsally and ventrally oriented larvae. Red arrows indicate the dominant morphological features for distinguishing dorsally vs. ventrally views. It is too difficult to reliably determine the larva's orientation based solely on comparisons with dorsal and ventral reference images. (b) The larva is rotated along its longitudinal axis through a full 360° and snapshots are acquired at two degree increments at 180 frames per second. (c) The system then correlates the images with a library of prerecorded dorsal and lateral images from stage-matched control larvae (inset). The blue and red curves in the radar chart are results of the image correlations with the dorsal and lateral templates. The blue, green, and red arrows indicate the orientations of maximum correlations with the dorsally, ventrally and laterally orientated templates, respectively. The reliability of the algorithm is 99 % ($n=100$ larvae)

Once the dorsal, ventral, and lateral orientations have been identified, the larva is automatically rotated for imaging at the predefined angle specified by the user (e.g. dorsally to image the brain, ventrally to image the heart and brachial arches, obliquely to image the pancreas). At this orientation, the ROI is defined by matching the larva to a third template of aged-matched larvae at the desired angle which contains the location of the ROI.

4.2.5 Analysis of capillary materials for high- quality imaging

Confocal imaging necessitates both low autofluorescence and low optical aberrations. Since larvae are imaged through a capillary in VAST, the choice of capillary material is a critical factor in achieving distortion-free, low-background, high-resolution imaging. A previous study reported that Teflon tubes offer optimal quality for bright-field imaging of larvae within capillaries (Ekker, Petzold et al. 2010), due to the matched refractive index with water. However, limited quantitative

data has been reported for fluorescence imaging, which is crucial for most experiments. Polymers such as PTFE (polytetrafluoroethylene) and FEP (fluorinated ethylene propylene), two types of Teflon, cause significant autofluorescence. This dramatically decreases the signal-to-noise ratio (SNR) and lowers the quality of fluorescent images. On the other hand, glass capillaries with ultra-low autofluorescence and extinction coefficients are not refractive index-matched to the surrounding water, which can create distortions and lead to decreased confocality and axial resolutions.

We have tested four capillaries of different materials and thicknesses and quantitatively evaluated the point-spread functions (PSF) of the resultant confocal images. GFP-tagged fluorescent micro beads (0.2 μm in diameter) were mixed in 2% Type IV optical agarose (Sigma, A3643) to avoid Brownian motion. The beads were then imaged with a multifocal confocal system with pinhole size of 30 μm , through a 100x 1.1 NA water dipping objective (Nikon Instruments). The beads trapped within the agar mold (index matched to water) were imaged either without any intervening glass, inside a PTFE capillary with a wall thickness of 250 μm (Zeus Inc.), inside an FEP capillary with a wall thickness of 150 μm (Zeus Inc.), inside a borosilicate capillary with a wall thickness of 170 μm (Wale Apparatus Co.), or within an ultrathin borosilicate capillary tube with a wall thickness of 10 μm (Capillary Tube Supplies Ltd.). Figure 4.5a shows a cross-section in the radial and axial planes through the center of a bead for each of the conditions.

We computed the axial full-width half-maximum (FWHM) of the PSFs without a capillary and when using the FEP, 170 μm thick borosilicate, and the 10 μm thick borosilicate capillaries. The FWHMs were 1.2 μm , 1.4 μm , 2.6 μm and 1.1 μm , respectively (Figure 4.5b). Due to the optical aberrations that cause non-Gaussian like PSFs on the PTFE capillary, we were unable to compute a FWHM. Importantly, our analysis shows that the 10 μm thick borosilicate capillary produces significantly less image distortion than the Teflon capillaries with refractive indexes closer to water. Furthermore, our autofluorescence analysis demonstrates that, unlike borosilicate, both types of Teflon (i.e. PTFE and FEP) cause significant autofluorescence (Figure

4.5c). Thus, we conclude the ultrathin (10 μm thick) borosilicate capillary is the most appropriate choice for high-resolution confocal imaging.

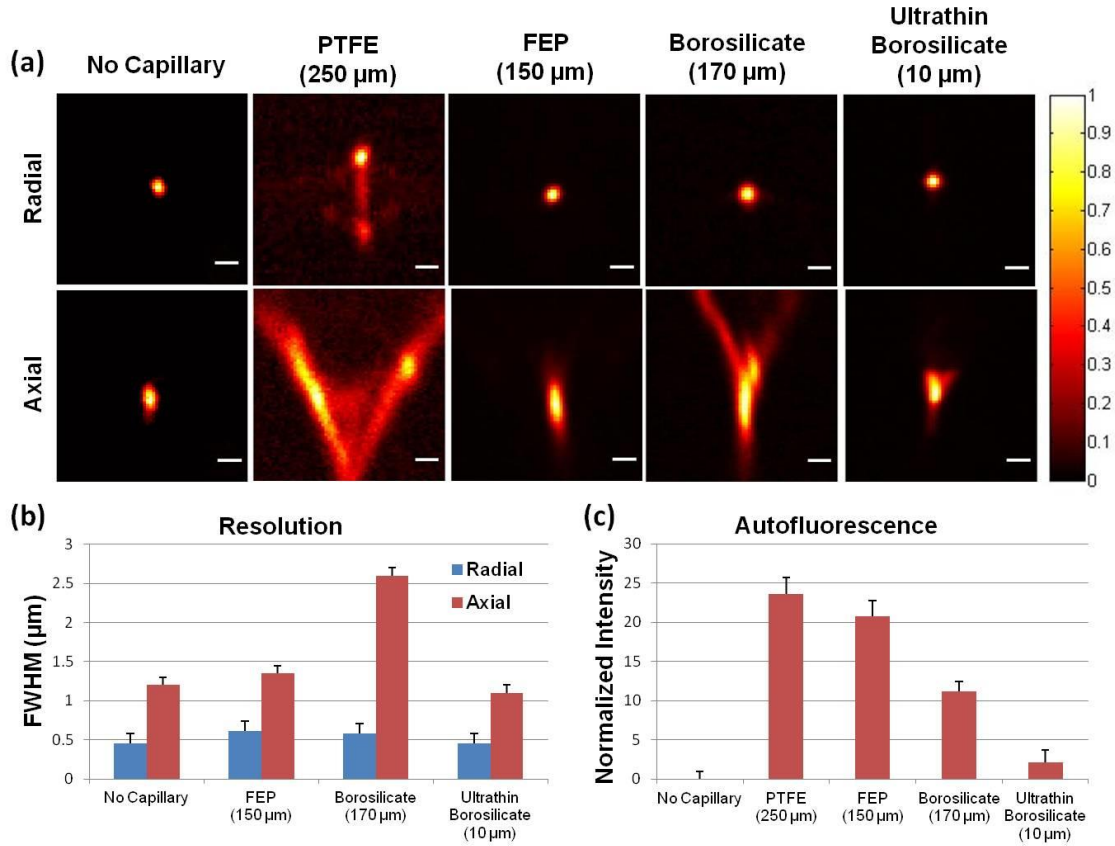


Figure 4.5: Analysis of capillary materials for distortion-free low-background high-resolution imaging. (a) From left to right, the point-spread functions (PSF) with different materials/conditions; no capillary, PTFE capillary, FEP capillary, borosilicate glass capillary, and ultra-thin borosilicate glass capillary. The wall thicknesses of capillaries are 250 μm , 150 μm , 170 μm and 10 μm , respectively. The ultra-thin glass capillary produces the least image distortion. Scale bar is 1 μm . (b) Radial (blue) and axial (red) resolutions of candidate materials. PTFE was not included due to the significant non-Gaussian PSF it produces. (c) Autofluorescence analysis of candidate materials. PTFE and FEP capillaries cause significant autofluorescence.

4.3 Methods

Wild-type and transgenic *Gt(T2KSAG)j1282b* zebrafish were used in all experiments. Zebrafish larvae were incubated at 28°C in E3 medium (5 mM NaCl, 0.17 mM KCl, 0.33 mM CaCl_2 and 0.33 mM MgSO_4) and were anesthetized with 0.2 mg/ml Tricaine during the experiments. All experiments were approved by MIT's Committee on Animal Care under protocol #0309-025-12.

4.4 Discussion and Summary

Here, we have demonstrated a fully automated multi-threaded vertebrate screening platform. To significantly increase throughput, we modularized the system into three independent sections that can process multiple zebrafish in parallel. In this configuration, system throughput is limited only by the image acquisition speed rather than by the speeds of fluidic and mechanical processes. A discriminator differentiates the entry of a fluorescent larva from non-fluorescent larva, air bubbles, and small debris. A simple and highly reliable algorithm is implemented for automated identification of the position and rotational angle of the larva. Furthermore, to identify the best capillary materials for confocal and fluorescence imaging, we analyzed various capillaries measuring their PSFs and autofluorescence. We showed that ultra-thin borosilicate capillaries (with wall thickness of 10 μm) provide the highest-resolution distortion-free low-background images.

5 A novel rapid optical projection tomography system for hyperdimensional *in vivo* phenotyping

In the following chapter, I will describe two novel technologies: a rapid optical projection tomography system capable of acquiring volumetric images of animals at speeds ~100 fold faster than existing systems, and a novel methodology to acquire and analyze a large number of independent metrics that are used to define a complex phenotype. The latter is based on results from the former, and although these can be used separately, we believe that they complement each other and together they represent a key advancement in high-content and high-throughput screening of complex samples such as zebrafish larvae. For this reason I have decided to group both these technologies in a single chapter.

To aid in the description of these technologies and methodology we have performed a proof-of-concept screen that assesses the appearance of craniofacial abnormalities on larvae after exposure to different classes of teratogen compounds.

5.1 Introduction

Large-scale screening of phenotypes induced by small molecules, natural products, gene mutations, and other agents is essential for all fields of modern biology and drug discovery. Although cell-based assays are amenable to high-throughput screening (HTS), results often fail to translate to animal models and clinical trials. Even the most sophisticated *in vitro* models fail to preserve the complexity and architecture of intact organs and *in vivo* processes such as disease pathology, tissue homeostasis, and drug-induced toxicity. To address these limitations, chemical screens are increasingly being conducted using zebrafish (*Danio rerio*) (Zon and Peterson 2005), a small vertebrate model organism that is widely used for genetic screens and is amenable to high-throughput methodologies. To date, however, chemical screens in zebrafish have typically ignored phenotypes not encompassed by more than a small number of pre-defined read-outs. The most ambitious efforts have focused on behavioral phenotypes and simultaneously assessed

up to a few dozen read-outs (Kokel, Bryan et al. 2010, Cachat, Stewart et al. 2011). Similarly, although large-scale genetic screens have been carried out for decades in zebrafish, the read-outs are often non-quantitative and limited to easily observed features. Morphological phenotyping remains a subjective process that can vary greatly between locales and lacks the systematization and throughput required for HTS.

To fully realize the potential of genetic and small molecule screens in vertebrates, it will be necessary to adopt a phenomics approach in which hundreds of morphological parameters are quantified and interpreted using unbiased, automated techniques similar to those developed for high content screening (HCS) of cells. For this purpose, we first demonstrate a high-throughput optical projection tomography (OPT) system that can generate three-dimensional (3D) images of entire zebrafish larvae at micrometer resolution within tens of seconds per larva (including all animal handling steps), an order of magnitude faster than existing OPT systems. Our system uses simple fluidics and image processing algorithms, and can be readily adapted to a variety of standard microscopes to rapidly generate micrometer -resolution 3D reconstructions of entire organs or other complex morphological features that have been labeled with standard histological dyes or by whole mount *in situ* hybridization or immunohistochemistry. This allows us to rapidly profile complex phenotypes in an unbiased manner using hundreds of independent morphological measurements on large numbers of animals. By hierarchically clustering the phenotypic signatures obtained under multiple screened conditions, we are then able to identify chemicals that act through related or different pathways *in vivo*. We term our approach hyperdimensional *in vivo* phenotyping (HIP).

5.2 Results

5.2.1 High-throughput optical projection tomography

High-content *in vivo* phenotyping of vertebrate model organisms necessitates rapid 3D imaging of large volumes of tissue. Conventional 3D imaging techniques, such as confocal and two-photon microscopy, rely on optically sectioning the specimen and are too slow for HTS of phenotypes

that encompass large regions of the body. Selective plane illumination microscopy (Voie, Burns et al. 1993, Huisken, Swoger et al. 2004) offers increased throughput, but suffers in samples containing opaque or highly scattering regions and is poorly suited for imaging larvae with developed organs. All of these techniques are dependent on fluorescent signals and cannot be adapted for commonly used chromogenic stains. OPT (Sharpe, Ahlgren et al. 2002) is a 3D imaging technique that computationally obtains volumetric information from collections of 2D images acquired at multiple sample angles. OPT is less subject to interference from intervening regions, has sufficient penetration depth to image an entire zebrafish larvae, and is compatible with both colored dyes and fluorescent reporters (Sharpe, Ahlgren et al. 2002, Ntziachristos 2010). In addition, unlike confocal and other optical slicing techniques, OPT yields rotationally symmetric voxels and therefore provides rotationally unbiased measurements. However, the throughputs of existing OPT systems are severely limited (acquisition times of 5-30 minutes per specimen) due to the complexity involved in sample preparation. The need to embed samples in agar or similar materials to stabilize them for precision rotation and image acquisition renders large-scale screens unfeasible (Sharpe, Ahlgren et al. 2002, Bryson-Richardson and Currie 2004). To avoid this limitation, we have developed a high-throughput OPT system that can handle and image entire non-embedded animals at micrometer resolution in tens of seconds by automatically correcting for errors due to animal movement and other artifacts (Figure 5.1).

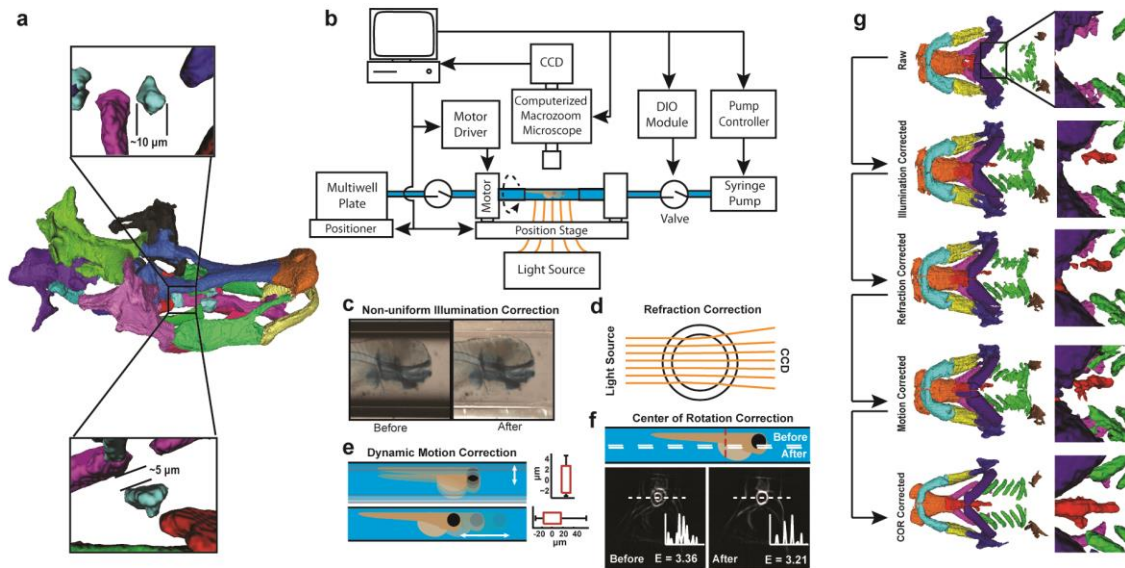


Figure 5.1: High-throughput optical projection tomography. (a) Tomographic reconstruction of the craniofacial cartilage after image processing. Insets show details of the hypobranchial bone. The resolution of the 3D reconstruction is sufficient to distinguish bones with dimensions of $\sim 10 \mu\text{m}$ and gaps of $\sim 5 \mu\text{m}$ between bones. (b) Schematic representation of the OPT platform. A fluidic system composed of a pump, valves, and tubing is used to load larvae from multiwell plates into an glass capillary located within the FOV of a macrozoom microscope. The capillary is held at two ends by stepper motors with hollow shafts that sit on a position stage. Several dynamic image artifact correction steps are performed prior to reconstruction. (c) Non-uniformity of illumination due to the capillary walls is corrected. (d) The light path through the capillary is simulated and is fed to the reconstruction algorithm to correct for the refraction of light by the capillary. (e) Small movements of the larva along the capillary axis and radial vibrations of the capillary are detected and corrected. The box-plots quantify the wobbling of the capillary (top plot) and the motion of the larva along the capillary axis (bottom plot) prior to correction. (f) Identifying the center of rotation (COR) for reconstruction. Reconstructing a cross-section using different COR estimates allows us to identify the true rotation axis with micron precision. The bottom panels show reconstructions using two different CORs. The reconstruction on the left corresponds to a COR estimated solely from the boundaries of the capillary sidewalls. The reconstruction on the right has sharper boundaries and lower entropy, and is therefore selected as the best estimate for true COR. Graphs show 1D intensity profiles across the dashed lines. Entropy of each image is shown on the bottom right corner. (g) Each step of image artifact correction produces increasingly accurate tomographic reconstructions. Images show 3D reconstructions from 320 images of a 5 dpf zebrafish larvae stained with Alcian blue. Insets show zoomed views of the most posterior region of the basihyal cartilage (red).

The system is simple and comprised of a standard computerized syringe pump and fluidic components (Figure 5.1b) that automatically loads individual zebrafish into a fluid-filled ultrathin borosilicate glass capillary, which we have recently shown to provide excellent imaging characteristics (Chang, Pardo-Martin et al. 2012). The capillary is held by two stepper motors that rotate the capillary through its main axis. With this system we are able to handle, rotate and image from multiple angles entire larvae (Pardo-Martin, Chang et al. 2010, Chang, Pardo-Martin et al. 2012). Unlike previous techniques, our method does not require larvae to be embedded, thereby eliminating the slowest and most labor-intensive step in OPT imaging. Live or fixed larvae are first automatically positioned in the capillary. Larvae are then rapidly rotated through 360 degrees, allowing images to be continuously acquired at a high frame-rate from multiple angles.

However, OPT reconstruction of such non-embedded samples present several new challenges that we first needed to address. Tomography algorithms require that the sample remains stationary and evenly illuminated during image acquisition. Additionally, the center of rotation (COR) of the imaged sample must be precisely known. Therefore, non-embedded samples need to be analyzed for (i) non-uniform illumination of the capillary (Figure 5.1c), (ii) refraction of light by the glass walls of the capillary (Figure 5.1d), (iii) motion artifacts arising from vibrations of the capillary and fluctuations in the fluidic pressure along the capillary (Figure 5.1e), and (iv) precise determination of the sample's center of rotation (COR) (Figure 5.1f).

We have developed algorithms that allow us to dynamically correct for each of these artifacts in every image frame. Prior to the image correction steps, an algorithm first determines the larva's orientation (head-first or tail-first) within the capillary (Chang, Pardo-Martin et al. 2012) and then aligns the capillary along the horizontal axis in each image by identifying its sidewalls through a Hough-transformation (Duda and Hart 1972).

Next, an algorithm corrects for non-uniform illumination between the sidewalls and the central axis of the capillary by first calculating average pixel intensities across regions containing no

larva, which are then used as a baseline to equalize illumination in all regions of the capillary (Figure 5.1c).

Two different types of motion artifacts arise during imaging of non-embedded samples: vibration of the capillary and longitudinal movement of the larvae within the capillary due to fluctuations in the fluidic pressure. Vibrations are automatically compensated for by identifying the sidewalls of the capillary. These landmarks are used to align all the images acquired at different angles and to stretch or shrink the images to equalize the capillary diameters across images. Longitudinal motions are automatically compensated for by identifying a prominent anterior feature (e.g. the tip of the head) and using this as a reference point to precisely align the larva across all the images (Figure 5.1e).

Estimating the COR by simply calculating the midpoint between the sidewalls of the capillary is insufficient for high-resolution reconstructions (Figure 5.1f 'Before'). We therefore automatically refine the COR estimate by using a filtered back-projection algorithm to compute multiple reconstructions of a single 2D transverse slice through the larva under different estimated CORs deviating slightly from the initial estimate. The COR whose reconstruction has the sharpest boundaries (i.e. lowest entropy) is considered to be the true COR and is used for the subsequent 3D reconstruction of the entire larva (Figure 5.1f 'After'). The corrected images are reconstructed using an order-subset expectation-maximization (OSEM) algorithm.

To produce the most accurate 3D reconstruction possible, the algorithm must take into account the refraction of light as it passes through the walls of the borosilicate glass capillary. To do this, we have modeled the path followed by parallel light rays originating from a source below the capillary and propagated them back to a virtual imaging plane (Figure 5.1d and Figure 5.2).

Using these algorithms, we can produce 3D reconstructions of non-embedded zebrafish larvae with micrometer resolution (Figure 5.1a and Figure 5.1c). For example, we are able to reliably detect individual bones and features of the segmented craniofacial skeleton (described below) with dimensions smaller than 10 μm and distinguish these from other structures located within only 5 μm .

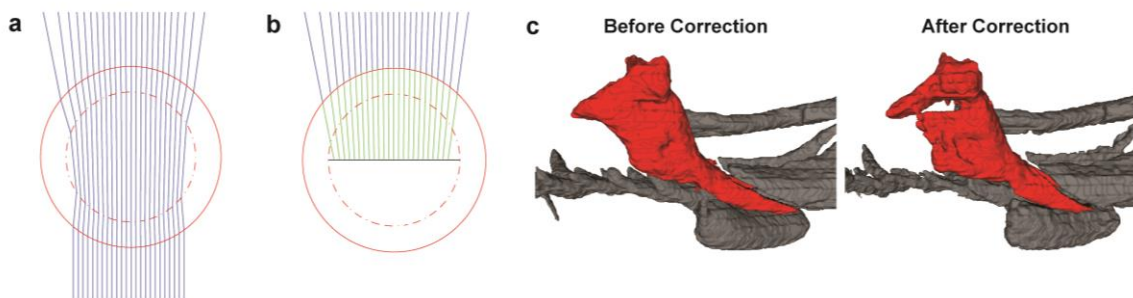


Figure 5.2: Compensation for the refraction of light rays by the capillary walls. (a) The path of light rays (blue) passing through the capillary as modeled using the Snell laws. Solid red lines indicate the outer surface of the capillary, dashed red lines indicate the inner surface of the capillary. (b) To estimate which CCD pixels the outgoing rays will reach to, we back-project (green) the previously computed outgoing rays (blue) without undergoing refraction deviations until they reach a virtual image of the CCD on the focus plane (black). This eliminates the need to model the optical lens by assuming that it is focused on the center of the capillary. (c) Image segmentation of the hyosymplectic bones before and after compensating for the index of refraction mismatch. After correction, the fine details of the bones are visible in the reconstructions.

The overall throughput for all imaging and handling steps is 18 seconds per larva (see Table 5). All steps of the OPT imaging process are automated, including the loading and positioning of the larva, capillary rotation, multi-angle image acquisition, unloading of larva, and movement of the loading nozzle to the subsequent well. During standard operation, the image acquisition rate is primarily governed by the camera's frame rate and the number of images acquired at different angles of rotation. To minimize the acquisition time we employ a high-speed CCD camera capable of acquiring 128 frames per second. We find that 320 images acquired as the sample is rotated through 360° are sufficient for accurate, high-resolution tomographic reconstruction. This allows a single larva to be imaged within only 2.5 seconds (i.e. exposure time of ~8 milliseconds). 3D image reconstruction from acquired multi-angle images is done automatically and offline; therefore it does not limit the speed of data acquisition and screening. Using a basic computer with a single processor, a 3D image with 250 x 250 x 450 pixels takes 3.5 minutes to reconstruct with the OSEM algorithm. For large-scale screens, image reconstruction can be easily accelerated by using multi-core computers or computer clusters.

Table 5: Timings for larva handling and image acquisition n=96

| Step | Mean Time (sec) | STD |
|---------------------------------|-----------------|------|
| Rough positioning of larva | 4.28 | 0.74 |
| Precise positioning of larva | 5.15 | 2.73 |
| Image Acquisition | 2.50 | 0* |
| Unloading of sample | 4.06 | 0.01 |
| Repositioning of loading nozzle | 2.01 | 0.21 |
| Total | 18.00 | 3.69 |

** The time required for this step is invariant.*

5.2.2 Assessment of craniofacial abnormalities

Histological dyes and chromogenic substrates (e.g. Alcian Blue, NBT/BCIP) modify the color or opaqueness of samples and are commonly used to label specific tissues. 3D reconstructions from samples labeled with these stains maintain their color properties, allowing features of interest to be computationally extracted through image analysis. The craniofacial skeleton stained with Alcian Blue is particularly attractive for 3D analysis due to its high level of organizational complexity. To analyze craniofacial cartilage, we employ a color-based linear discriminator model based on previous training data to automatically identify voxels associated with stained tissue based on their RGB values. Using this approach, we are able to successfully separate the craniofacial skeleton from surrounding tissues with exquisite precision and accuracy (Figure 5.1a). The isolated craniofacial skeleton is subsequently segmented into individual bones using a semi-automated but rapid algorithm. Using segmented 3D reconstructions from our system, we can visualize individual craniofacial bones and substructures with dimensions smaller than 5 μm (Figure 5.1a). The voxel size used for the craniofacial assessment described below is 2.25 μm x 2.25 μm x 2.25 μm , which is sufficient to accurately assess the morphology of all bones in zebrafish larvae at 5 days post fertilization (dpf).

Our high-throughput OPT system makes it possible to rapidly acquire large numbers of high-resolution 3D reconstructions and characterize the morphology of entire organs and body regions in great detail under numerous experimental conditions. Analysis of such large, dimensionally complex data sets can be facilitated by techniques developed for high-content cell-based assays:

automated feature extraction and quantification, unbiased data analysis, and hierarchical clustering. We have coined the term hyperdimensional *in vivo* phenotyping (HIP) to describe the application of HCS methodologies to large-scale whole-organism screens.

To demonstrate the utility of HIP in zebrafish, we have performed a proof-of-concept screen focusing on the craniofacial skeleton. The head skeleton of a 5 dpf zebrafish is composed of over 30 cartilaginous elements derived from two distinct migratory cell populations—cranial neural crest (CNC) and paraxial mesoderm—that are patterned by a variety of inductive signals from the surrounding tissues (Schilling and Kimmel 1994, Schilling and Kimmel 1997, Knight and Schilling 2006). Because the structure and the function of the skeletal system are intimately connected, the size, shape, location, and morphogenesis of all elements are tightly yet differentially regulated. Genetic or teratogenic perturbations in pathways governing cell migration, proliferation, or differentiation can lead to craniofacial malformations, which constitute the most common class of birth defects in humans (Young, Schneider et al. 2000). Craniofacial anomalies (CFA) are almost always studied in whole vertebrate models due to the strong influence of anatomical context on head skeleton morphogenesis. Even the most promising cell-based assays—such as embryoid bodies grown from embryonic stem cells—are limited to relatively simple read-outs such as osteoblast formation (zur Nieden, Davis et al. 2010).

Table 6: Chemicals and catalog numbers employed in teratogen screen

| Chemicals | CAS Number | Catalog Number (Sigma-Aldrich) |
|--|------------|--------------------------------|
| Triadimefon | 43121-43-3 | 45693 |
| Flusilazole | 85509-19-9 | 45753 |
| 13- <i>cis</i> -retinoic acid (Isotretinoin) | 4759-48-2 | R3255 |
| 9- <i>cis</i> -retinoic acid (Alitretinoin) | 5300-03-8 | R4643 |
| All- <i>trans</i> -retinoic acid (Tretinoin) | 302-79-4 | R2625 |
| Retinol (Vitamin A) | 68-26-8 | R7632 |
| Cyclopamine | 4449-51-8 | C4116 |

We selected chemicals that have been functionally linked to CFA in mammals for characterization via HIP in zebrafish (see Table 6). These chemicals can be divided into three classes based on their structures and underlying mechanisms of action: (1) Retinoids [retinoic acid (RA) in the all-trans conformation (atRA), the 9-*cis* isomer of RA (9-*cis*-RA), the 13-*cis* isomer of RA (13-*cis*-RA),

and retinol (a precursor to RA)], (2) triazole derivatives (triadmefon, fluconazole and flusilazole), and (3) steroidal alkaloids (cyclopamine). We hypothesized that malformations caused by these teratogens would differ in subtle ways that correlate with their underlying mechanism(s) of action and that such phenotypic variations would be captured by our technique and could be used to identify chemicals acting through similar mechanisms. Prior to CFA screening, a viability assessment was conducted by applying all chemicals at half log intervals ranging from 3 nM to 1 mM to determine the concentration causing lethality in 50% of treated larvae (LC₅₀) under the dosing protocol (Table 7).

Table 7: Concentrations and LC₅₀ for test chemicals

| Chemical | Vehicle | Lowest Concentration Exceeding LC ₅₀ | Test Concentrations (μM) |
|-----------------------|---------|---|----------------------------|
| Triadmefon | DMSO | 300 μM | 3, 10*, 30*, 100 |
| Flusilazole | DMSO | 100 μM | 1, 3*, 10*, 30 |
| Fluconazole | DMSO | > 1 mM | NA |
| 13- <i>cis</i> -RA | DMSO | 30 nM | 0.001*, 0.003*, 0.01 |
| 9- <i>cis</i> -RA | DMSO | 30 nM | 0.001*, 0.003*, 0.01 |
| all- <i>trans</i> -RA | DMSO | 100 nM | 0.001, 0.003*, 0.01*, 0.03 |
| Retinol | DMSO | 10 μM | 0.3*, 1*, 3 |
| Cyclopamine | Ethanol | 100 μM | 1, 3*, 10*, 30 |

* Concentrations used for clustering of chemicals in Figure 5.6c.

One test chemical (Fluconazole) was eliminated from the screen because elevated mortality was not observed at the maximum screenable concentration (1 mM) and we were therefore unable to determine an LC₅₀. Larvae were exposed to the chemicals starting at either 9 hours post fertilization (hpf) or 30 hpf to differentiate between chemically induced effects before and after the onset of CNC migration, which begins at approximately 12 hpf (Schilling and Kimmel 1994). Treatment was terminated at 3 dpf and the larvae were allowed to develop until 5 dpf. OPT imaging was carried out on fixed 5 dpf larvae stained with Alcian Blue and all chemicals were assessed at the three half-log intervals immediately below the calculated LC₅₀. For each larva, 320 frames were acquired at 4× magnification with an exposure time of 0.3 ms per image frame. The acquired images were reconstructed and segmented as described above. Figure 5.3a shows fully segmented reconstructions of representative larvae exposed to increasing

concentrations of chemicals from the three different classes: atRA (a retinoid), cyclopamine (a steroidal alkaloid), and flusilazole (a triazole derivative). The progression of morphological abnormalities at increasing concentrations follows distinct patterns for each class of chemicals. For example, the angle formed between Meckel's cartilage and the palatoquadrate is deflected ventrally by retinoids, dorsally by steroidal alkaloids, and remains unchanged by triazoles (Figure 5.3a). Quantitative analysis of these metrics shows that individual chemicals do not alter every bone of the craniofacial skeleton in the same manner and to the same degree (Figure 5.3b). Moreover, individual bones (Figure 5.3c), as well as their relative lengths (ratio between two bones) (Figure 5.3d), exhibit unique concentration-dependent responses to different chemicals (compare the trends in Figure 5.3c vs. Figure 5.3d). This indicates that measuring the morphology of a single bone is insufficient to fully describe the phenotypic variations induced by each chemical and measurements of multiple features and their interrelations are essential for complete characterization of phenotypes.

To quantify how much of the variation observed in individual metrics is due to actual difference in the craniofacial elements being measured and how much arises from errors in sample processing (e.g. sample illumination, image processing, segmentation, etc.), we compared reconstructions obtained from (1) the same untreated control larva loaded, imaged and reconstructed multiple times, (2) multiple untreated control larvae, and (3) multiple larvae exposed to 10 nM atRA (Figure 5.4). Our analysis shows the variations among replicate images of the same larvae are much smaller than those among different treated and untreated larvae, indicating that the variations introduced by our imaging and image reconstruction methods are negligible.

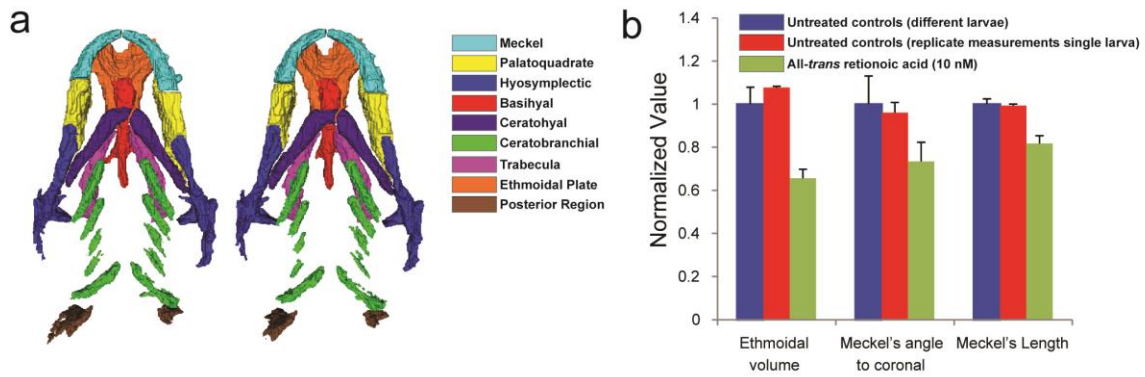


Figure 5.4: Analysis on repeatability of reconstruction and segmentation. (a) Representative reconstruction and segmentations of a single untreated control larva loaded and imaged multiple times. (b) Bar plot showing normalized values for the ethmoidal volume, meckel's angle to the coronal plane, and meckel's length. Values are shown for different untreated control larvae (blue), a single untreated control larva loaded and imaged multiple times (red) and for larvae treated with 10 nM of all-trans-retinoic acid (green) ($n=5$ for each treatment condition, \pm s.e.d).

5.2.3 Hyperdimensional in vivo phenotyping

To fully quantify the phenotypic variations in an unbiased manner, we compute a total of 202 independent metrics from each 3D reconstruction (see Table 8). These metrics include lengths, three-dimensional orientations, surface areas, and volumes of different skeletal bones. To perform analyses on groups of diverse features, the metrics first need to be adjusted to a notionally common scale that also accounts for statistical variation in controls. This is done by calculating a standard score, which indicates the number of standard deviations each metric is

from the mean of the control distribution and takes into account normal variation within the untreated population. This score is obtained by calculating the mean value for the metric over a large control population ($n=53$), subtracting the control value from the individual metric, and dividing the difference by the standard deviation of the control population. A two-tailed Student's t-test is also computed for each metric to calculate a p-value between the chemically-treated and control larvae. These measurements are then used to construct a hyperdimensional phenotypic signature for each larva (Figure 5.6a, right panel). In order to determine whether the large number of metrics use in the phenotypic signature provides redundant or non-redundant information, we computed the cross-correlation between standardized metrics for all screened conditions (Figure 5.5). The correlations among measured values of different metrics were low, indicating a high degree of independence across metrics (Figure 5.5a and Figure 5.5b inset). To further confirm the non-redundancy (i.e. orthogonality) of our measurements, we performed principal component analysis (PCA) and quantified the contribution of each metric to the overall hyperdimensional phenotypic signature. Despite the large number of metrics used, PCA showed that addition of each metric contributed new and non-redundant information about the specimen (see Figure 5.5), indicating that HIP is more descriptive and information-rich than traditional low-content phenotyping.

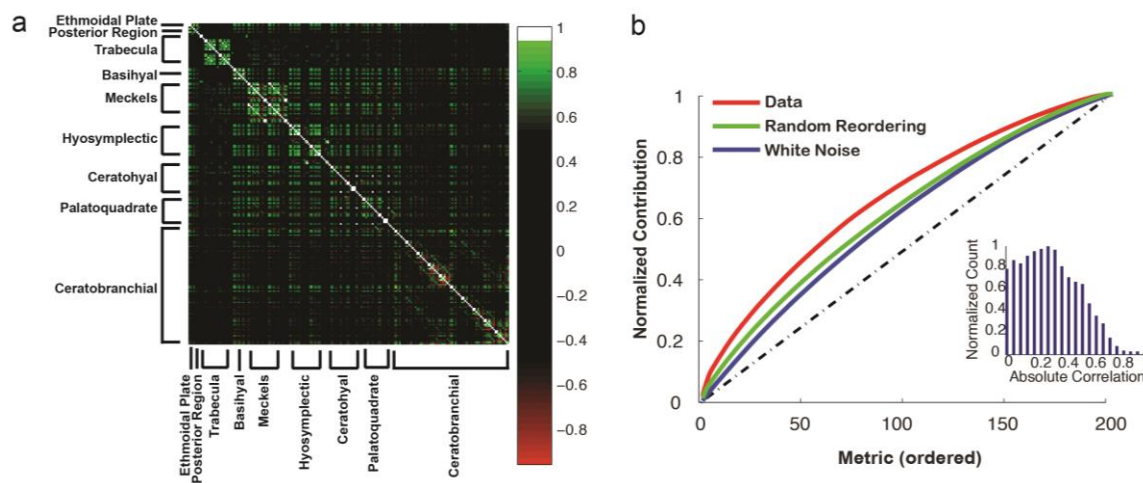


Figure 5.5: Independence of Phenotype Metrics Used. (a) Correlation matrix for metrics across all samples. Bones on which the metrics are based are indicated along the x- and y-axes. White indicates correlation coefficient values above 0.95. High correlations are primarily constrained to the main diagonal, indicating that most metrics behave in an uncorrelated manner. (b) Principal component analysis shows that each metric contributes non-redundant information to the phenotypic signatures. Plot shows the cumulative normalized contribution of each metric to the eigenvalues of the most significant principal components obtained through principal component analysis (red). Black dotted line indicates the cumulative sum if all metrics contributed equally. Green line shows the same analysis with random reordering of all metrics. The blue line shows the same analysis performed on white noise. The small inset shows the histogram of the correlation coefficients across metrics for all samples. These values are centered at a low correlation value of 0.3.

To determine whether or not hyperdimensional phenotypic signatures can reveal similarities and differences in the underlying mechanism(s) of action of test chemicals, we first performed hierarchical clustering based on the correlation of the p -values for all the samples and metrics to produce a heat map. Several distinct groups are apparent in the resultant heat map and individual larvae exposed to the same chemical at the same concentration tend to cluster together. To more precisely quantify similarities and differences between chemicals, we calculated the mean standardized value for every one of the 202 metrics for each test condition (3 to 8 larvae per condition). Due to the extreme malformations at concentrations near the LC_{50} , we eliminated the test concentration immediately below the calculated LC_{50} from our analysis and included the

remaining two half-log interval concentrations in our analysis. The result is a hyperdimensional phenotypic signature for each chemical that consists of 404 metrics (202 at each concentration).

Cluster analysis of the hyperdimensional phenotypic signatures from our test screen produces a dendrogram with two distinct groups, one encompassing all the retinoids (red) and another encompassing the two triazole derivatives (green; Figure 5.6c). Cyclopamine is highly uncorrelated with these two groups. Moreover, our analysis reveals similarities between retinoids and the triazole derivatives (Figure 5.6c). These results are consistent with the known biochemical pathways and underlying mechanisms of action (Chen, Taipale et al. 2002, Mark, Ghyselinck et al. 2006, Menegola, Broccia et al. 2006, Hernandez, Putzke et al. 2007, Duester 2008). Vitamin A (retinol) and its active derivatives (the retinoids) regulate transcription of RA target genes and are important therapeutic agents in oncology and dermatology (Mark, Ghyselinck et al. 2006). Triadimefon and flusilazole are triazole fungicides that act by inhibiting enzymes of the cytochrome P450 (CYP) family, including CYP26 (Menegola, Broccia et al. 2006) and several triazole derivatives are under investigation as CYP26-specific inhibitor (Gomaa, Bridgens et al. 2011). CYP26 metabolizes RA to an inactive form (Fujii, Sato et al. 1997) and loss of its activity leads to increased RA-dependent gene expression and teratogenic phenotypes similar to those induced by exogenous RA in mouse and zebrafish embryos (Yashiro, Zhao et al. 2004, Hernandez, Putzke et al. 2007). Cyclopamine, on the other hand acts by binding to Smoothened and blocking the Hedgehog signaling pathway, which acts independently of the retinoid pathway (Chen, Taipale et al. 2002).

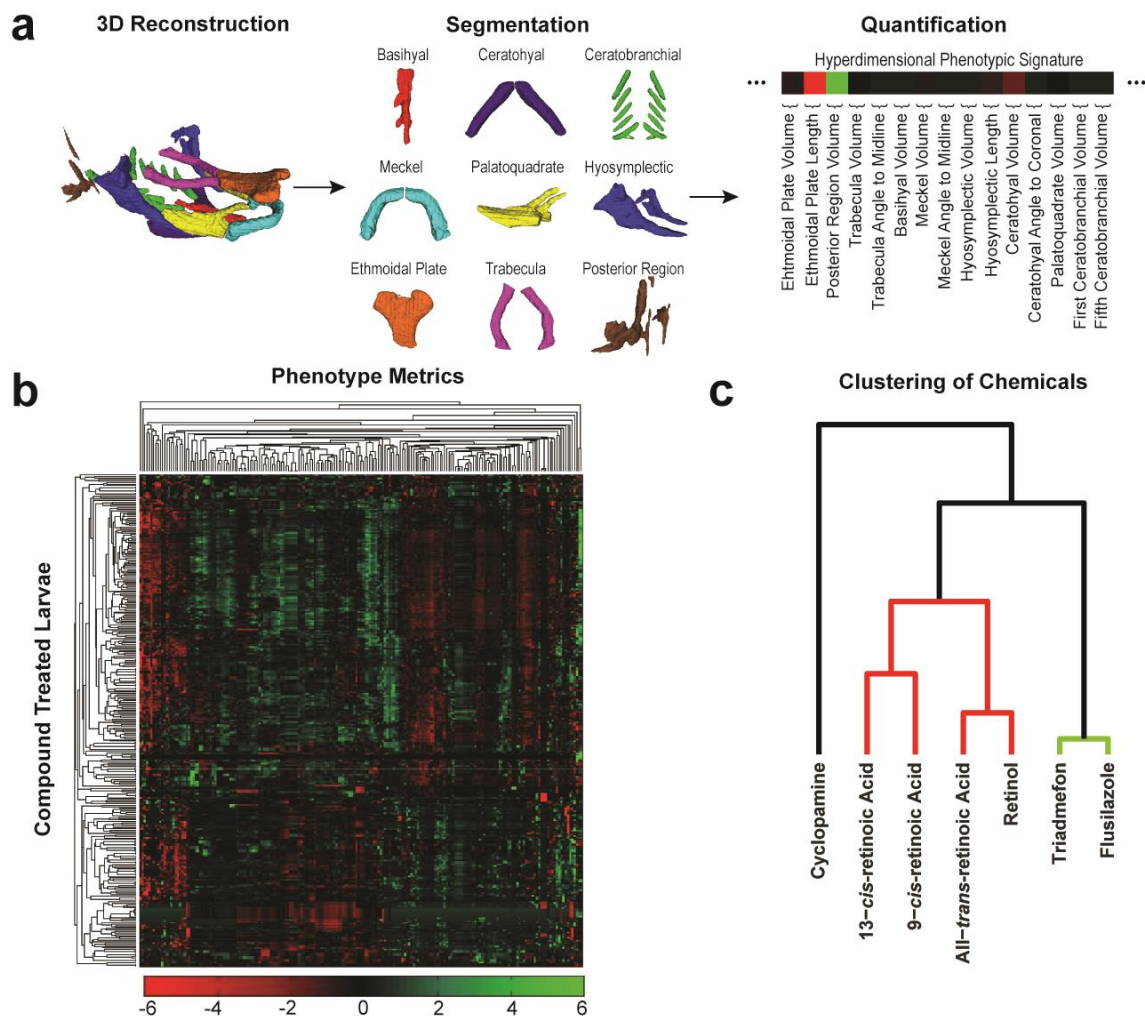


Figure 5.6: Hyperdimensional in vivo phenotyping. (a) Schematic representation of the analysis process. Following 3D reconstruction (left) Individual bones are segmented and separated by bone type (center). Morphological image analysis is then used to compute metrics for each bone segment (e.g. volume, length, angles, surface area, and location). These values are stored as a hyperdimensional phenotypic signature for each larva (right). (b) Phenotypic signature array (shown log 10 scale of p-values). Each row represents individual larvae treated with a compound. Measurements are color-coded to indicate a reduction (red) or an increase (green) with respect to untreated controls. Phenotype metrics and compound treated larvae are ordered by hierarchical clustering based on correlation. (c) Dendrogram computed on linkage by correlation of the mean standard score for chemicals applied beginning at 9 hpf. Teratogens known to cause developmental bone abnormalities are grouped based on similarities in their hyperdimensional phenotype signature. Retinol and the retinoids (red) and the triazole derivatives (green) cluster together in groups that are distinct from cyclopamine (a steroidal alkaloid).

HIP reveals additional correlations between members of the retinoid group that may reflect underlying differences in their mechanisms of action (Figure 5.7). Retinoids act primarily through two nuclear receptor families—retinoic acid receptors (RARs) and retinoid X receptors (RXRs)—which control transcription of RA target genes (Mark, Ghyselinck et al. 2006). RARs bind both atRA and 9-cis RA with high affinity, while RXRs preferentially bind 9-cis-RA and serve as obligatory partners for RAR and other nuclear receptors (Allenby, Bocquel et al. 1993). Unlike atRA and 9-cis-RA, which are biologically active ligands, retinol must first undergo enzymatic metabolism to retinaldehyde and then to RA (Duester 2008, Ziouzenkova and Plutsky 2008). The predominant biologically active derivative of retinol is atRA (Theodosiou, Laudet et al. 2010). These findings agree well with our observation that the hyperdimensional phenotypic signatures of retinol and atRA cluster together on the same branch and are distinct from, but closely related to, 9-cis RA (Figure 5.6c). Interestingly, although 13-cis RA shows low *in vitro* binding affinity to RARs and RXRs and low activity in gene expression assays (Armstrong, Redfern et al. 2005, Schroeder and Zouboulis 2007), it is a potent teratogen *in vivo* (Benke 1984) and clusters with other biologically active retinoids when assessed by HIP in zebrafish larvae.

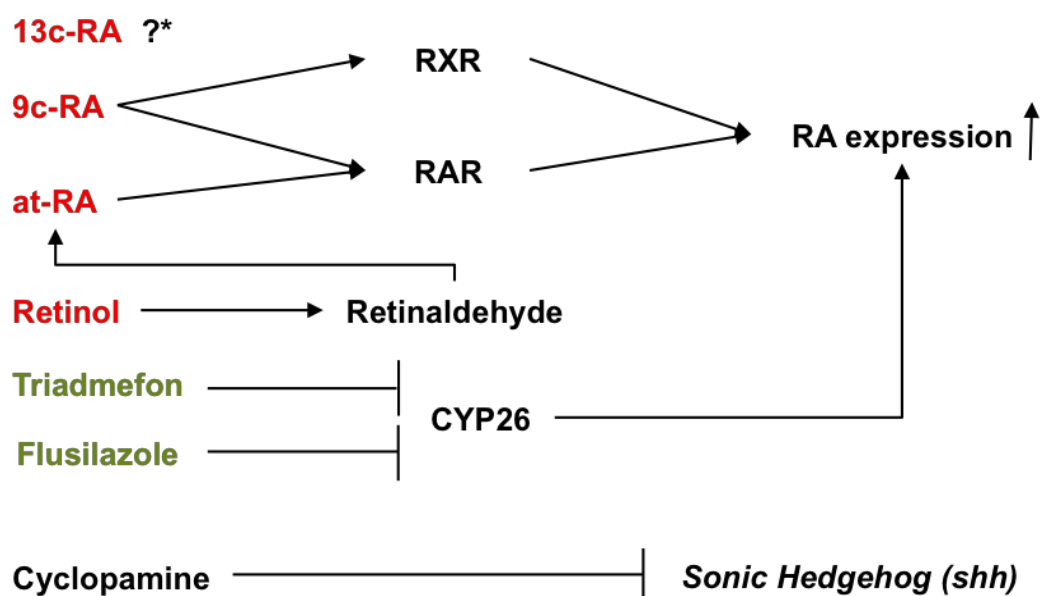


Figure 5.7: Mechanism of action of the screened teratogen compounds. Compounds labeled in red are from the retinoids family, compounds in green are from the triazole-derivative class and Cyclopamine belongs to the steroidal-alkaloid family.

Table 8: Complete list of metrics employed for HIP in the teratogen screen.

| Bone | Metric | Bone | Metric |
|-------------------------------|--|------------------------------------|--|
| Etmoidal Plate | Volume Surface Surface/Volume Length Height Thickness Center of Mass (Y) | Hyosymplectic (left and right) | Volume Surface Surface/Volume Length Thickness Depth Width |
| Posterior Region | Volume Surface Surface/Volume Number bones | | Angle to Sagittal Angle to Transverse Angle to Coronal Plane Height front Height back Steepness |
| Trabecula (left and right) | Volume Surface Surface/Volume Length Center of Mass (y) Width Thickness Angle to Sagittal Angle to Transverse | Palatoquadrate (left and right) | Volume Surface Surface/Volume Length Thickness Depth Width |
| Basihyal | Volume Surface Surface/Volume Length Thickness Depth Width Number bones | | Angle to Sagittal Angle to Transverse Angle to Coronal Plane |
| Meckel's (left and right) | Volume Surface Surface/Volume Length Thickness Depth Width Angle to Sagittal Angle to Transverse Angle to Coronal Height front Height back Steepness | Ceratohyal (left and right) | Volume Surface Surface/Volume Length Thickness Depth Width Angle to Sagittal Angle to Transverse Angle to Coronal Plane |
| | | Ceratobranchial (each bone) | Volume Surface Surface/Volume Length Angle to Sagittal Angle to Transverse Angle to Coronal Plane |

5.3 Methods

In the next section I will describe an overview of the methods used for both rapid optical projection tomography and for hyperdimensional *in vivo* phenotyping. For simplification methods

that are not novel are not fully described here. In these instances a more detailed description of the methods are found in the previous work referenced in each subsection.

5.3.1 Sample handling and image acquisition

The system loads fixed or anesthetized larvae from multiwell plates or reservoirs and positions them inside an ultrathin borosilicate glass capillary tube located under the field-of-view (FOV) of a microscope through the use of a computerized syringe pump (Pardo-Martin, Chang et al. 2010, Chang, Pardo-Martin et al. 2012) (Figure 5.1b). We have previously demonstrated ultrathin borosilicate glass to be an excellent capillary material due to its low autofluorescence and optical distortion (Chang, Pardo-Martin et al. 2012). A three-axis linear stage positions the loading nozzle and the computerized syringe pump aspirates the larvae into a flexible tube connected to the glass capillary. The larvae are automatically detected and positioned under the FOV as previously described (Pardo-Martin, Chang et al. 2010, Chang, Pardo-Martin et al. 2012). The capillary is held by two stepper motors with hollow shafts that rotate it around its longitudinal axis. The capillary is immersed in water for refractive index matching between the inside and outside of the tube. The stepper motors rotate the capillary at a predefined speed while a high-speed camera acquires images at multiple angles. The rotation speed and timestamps assigned to each image frame are used to precisely calculate the angle of rotation of capillary at each frame.

5.3.2 Tomographic reconstruction

Before performing the tomographic reconstruction we align the images and correct for imaging and movement artifacts. From the corrected rotational images, we reconstruct the 3D object with an iterative reconstruction method. Each of the color channels is reconstructed independently to yield a color 3D-reconstruction. During this study we employed two different reconstruction algorithms described previously; filtered back projection (FBP) (Brown and Brown 1999) and Ordered Subset Expectation Maximization (OSEM) (Hudson and Larkin 1994). The FBP is a fast reconstruction method but does not provide the same reconstruction quality as iterative methods. Methods such as OSEM and Maximum likelihood Expectation Maximization (MLEM) (Lange and

Carson 1984) provide better reconstruction quality but are computationally demanding. Due to the superior speed of the FBP we use it to detect the COR, where speed is more important than the quality of reconstruction. The OSEM is an optimization of the expectation maximum reconstruction algorithm. The projection data are grouped into an ordered sequence of subsets. The iterative reconstruction is then performed on the subsets, resulting in a faster convergence. The OSEM provides significant speed increase compared to the MLEM while preserving image quality. For the whole animal reconstruction we use OSEM method, as it provides good quality and acceptable reconstruction time. Reconstruction algorithms work under the assumption that the light-rays reaching the detector undergo a rectilinear trajectory. These algorithms suffer from refraction due to index mismatch between the ultrathin capillary glass and the larva medium. As described in the Light Simulation section, we model the propagation of light through the capillary and employ the ray paths for the Radon transformation before reconstruction to compensate for this mismatch in the index refraction (see Figure 5.2).

5.3.3 Image segmentation and bone identification

The region(s) of interest (i.e. the Alcian blue-stained cartilaginous bones of the craniofacial skeleton) were segmented from the 3D reconstruction to facilitate morphometric analyses. In general, features of interest will differ depending on the application and there are many different 3D segmentation algorithms that can be applied to this type of data (Pham, Xu et al. 2000). Here we used a color-based linear discriminant analysis (LDA) (Fisher 1936) to segment the bones from the surrounding tissue. A GUI with a slice view of the x-y, x-z, and y-z planes provides the user with the ability to browse through the reconstructed sample from several angles. The user marks regions containing the desired anatomical structure (e.g. Alcian blue stained cartilage) and background regions not associated with the structure. These data serve as the training set of a classifier for identifying the desired structure. By using a linear discriminant classification, all samples in the data set can be classified according to the classes defined by the initial training set. A similar GUI isolates each segmented feature and presents it sequentially to the operator. If the segmented feature comprises a single bone, the operator can use the keypad to rapidly select

the appropriate label for the bone. If the segmented feature comprises two or more bones, the operator clicks once at each side of the intersection between the bones and an algorithm automatically separates them, assigning different labels to each. If the segmented feature presented to the user is not a bone (e.g. a melanophore or other high contrast structure that was mistakenly picked up by the linear discriminant classification) the user can delete the feature from the analysis. Although fully-automated algorithms can in principle be developed to segment and label the various bones of the skeleton, our semi-automated algorithm is rapid enough and sufficiently robust that a user can segment the entire skeleton accurately in less than one minute.

5.3.4 Maintenance of fish, embryo collection, and staging of larvae

Zebrafish were maintained under standard laboratory conditions and embryos and larvae were staged according to standard practices (Kimmel, Miller et al. 2001). All procedures on live animals were approved by the Massachusetts Institute of Technology Committee on Animal Care.

5.3.5 Cartilage staining

The nomenclature for cartilaginous bones used throughout the present study is based on Kimmel et al. (Kimmel, Miller et al. 2001). Alcian blue staining was carried out essentially as described in previous work (Schilling and Kimmel 1997). Briefly, at 5 dpf larvae were anesthetized with tricaine (E10521; Sigma-Aldrich) and fixed overnight at room temperature in 10% neutral buffered formalin solution (HT5011; Sigma-Aldrich). The larvae were transferred into a solution of 0.01% Alcian blue (A5268; Sigma-Aldrich) dissolved in 80% ethanol and 20% glacial acetic acid and stained for 20 hours at room temperature. After staining, the larvae were rinsed briefly in ethanol, destained for 1 hour in acidic ethanol (5% HCl, 75% EtOH, 20% H₂O), rehydrated in PBS, and the tissue was cleared in a 1% trypsin solution (T7409; Sigma-Aldrich) dissolved in 30% saturated sodium tetraborate for 6 hours at room temperature. The specimens were stored in PBST at 4°C prior to imaging. All Alcian blue staining steps were carried out in 24-well cell culture plates.

5.3.6 Assay design and chemical treatment

At approximately 2-4 hpf embryos were collected and transferred into E3 medium (5 mM NaCl, 0.17 mM KCl, 0.4 mM CaCl₂, and 0.16 mM MgSO₄) at 28°C. At 9 and 30 hpf, healthy embryos were arrayed into 24-well cell culture plates (4 embryos per well) containing 1 mL of E3 medium. Embryos were allowed to remain in their chorions for chemical application at 9 hpf and dechorionated immediately prior to chemical application at 30 hpf using pronase. For each treatment condition, a 100× working stock of test chemical was prepared in 100% DMSO (for cyclopamine, 200× working stocks were prepared in ethanol) and 10 µL of the working stock (5 µL for cyclopamine) was added to each well. Each experiment consisted of 8 embryos per treatment condition (see Table 7) and 53 vehicle controls (1% DMSO or 0.5% ethanol). Following treatment, embryos were continuously incubated in covered plates at 28°C until the end of the experiment. Embryos were maintained in test chemical (without medium changes) until they reached 3 dpf, at which point they were removed from test chemical, washed briefly, and raised in E3 medium until 5 dpf.

5.3.7 Test chemicals

All test chemicals were purchased from Sigma-Aldrich. CAS numbers and catalog numbers are provided in Table 6. Stock solutions were prepared at 10 or 100 mM in dimethyl sulfoxide (DMSO), except for cyclopamine which was prepared as a 20 mM stock in ethanol as previously described (Chen, Taipale et al. 2002).

5.3.8 Timings

Timings were measured using the 'clock' functions in MATLAB and have been performed on a 96-well microtiter plate (see Table 5). Times include average loading, imaging, and unloading of the samples. Other sample preparation steps (such as staining, 3D image reconstructions and image segmentation) are not included in the analysis.

5.3.9 Statistics

To calculate the p -values between the chemically treated and control larvae we employed two-tailed Student's t -test.

5.3.10 Components of the system

The multiwell plate loading system consists of three linear precision motors (RCA2; Intelligent Actuators). The motors are controlled with RACON 10 drivers (Intelligent Actuators) and a RoboNet Serial Interface Module (RGW-SIO; Intelligent Actuators). Two fluidic valves (075P2NC12; Bio-Chem Fluidics) are used to stop the fluid flow when the sample is positioned in the field-of-view to minimize longitudinal motions along the axis of the capillary (CV7087; Wale Apparatus) due to micro-fluctuations in fluid pressure stemming from pinching/torque of silicone tubing (1/32 inch/0.8 mm inner diameter \times 3/32 inch outer diameter; Bio-Chem Fluidics). The valves are driven through an external digital output module (NI 9472 & NI USB-9162; National Instruments). The flow across the system is controlled by a computerized syringe pump (Cavro XLP6000; Tecan System) with a 5 mL glass syringe (Tecan Systems). The imaging system consists of an upright zoom microscope (AZ100; Nikon Instruments) with a 2 \times AZ Fluor lens (Nikon Instruments). The images are captured with a high-speed CCD camera (Prosilica GX-1050C; Allied Vision Technologies). The capillary tube is rotated by a set of two 5-phase hollow shaft motors (AH1K-S543; Autonics) run by 5-phase microstepping drivers (MD5-HF14; Autonics), which are themselves driven by an external serial controller (PMC-2HS-USB; Autonics). The capillary and motors are held on a linear motorized stage for fine positioning (PT1-Z8; Thorlabs) driven through a DC Motor Controller (TDC001; Thorlabs).

5.3.11 Image alignment

Zebrafish larvae can enter the capillary in a head-first or tail-first orientation, therefore the direction of each larva must first be determined. To do so, we compute a 1D intensity profile of the larva along the capillary by summing up the intensity of pixels across the capillary. There is a significant intensity difference between the tip of the head and the capillary surrounding the fish.

The tip of the head is identified by finding the maximum of the derivative of the 1D intensity profile. The center of mass of the 1D profile is then computed. The center of mass falls in the upper part of the abdomen, and we determine the direction of the larva by comparing the position of the tip of the head and the center of mass of the larva (Chang, Pardo-Martin et al. 2012). We next align the capillary across all rotational images (Figure 5.8b). This is accomplished by detecting the sidewalls of the capillary and performing a Hough transform (Duda and Hart 1972) to determine the angle of the sidewalls. We then rotate each image to correct for the deviation in this angle (Figure 5.8a).

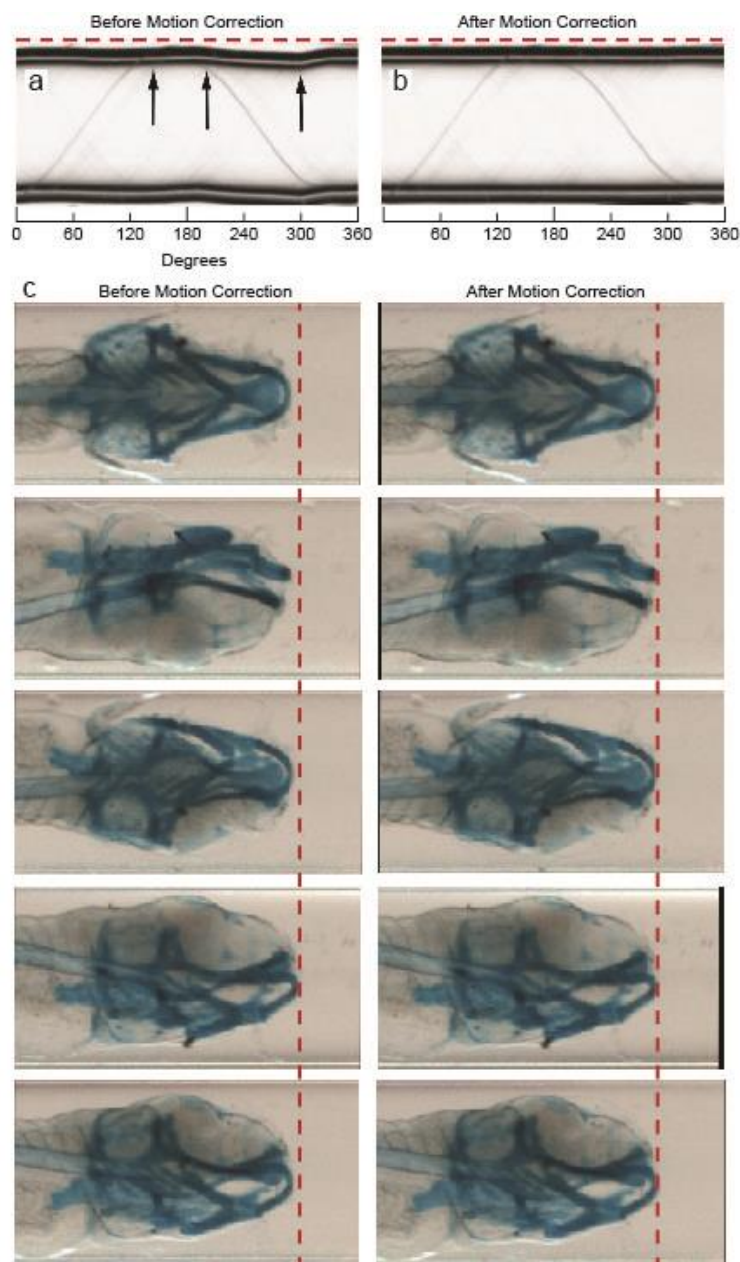


Figure 5.8: Compensation for wobbling of the ultrathin capillary and longitudinal movement of the larva. (a-b) Sinograms (i.e. single column (y-axis) of pixels obtained from the collection 2D images acquired at all angles through rotation (x-axis)) of $4\ \mu\text{m}$ large beads attached to capillary walls. (a) Sinogram prior to correcting for wobbling of the ultrathin capillary. Black arrows point to angles at which the capillary experiences significant motion orthogonal to capillary axis. (b) Sinogram image after automatically correcting for wobbling. The large movements are compensated for and the capillary sidewalls remain stationary at all angles of rotation. (c) Five frames before and after compensating for the longitudinal sliding of the larva along the capillary axis (x-axis). Prior to artifact correction, the tip of the larva's head is not aligned across all images. Red dashed lines are straight reference lines that have been added to aid visualization of the corrections of the artifacts.

5.3.12 *Image artifact corrections*

Two different types of motion artifacts arise during rotation of the capillary, which introduce distortions into the final 3D reconstruction if not compensated for: wobbling of the larva due to vibrations of the capillary and longitudinal sliding of the larva along the capillary axis due to fluctuations in the fluidic pressure. Small wobbles of the capillary are detected by tracking the sharp boundaries at the edges of the capillary. We use a sub pixel cross correlation method to detect the motion of each capillary sidewall separately (Guizar-Sicairos, Thurman et al. 2008). We use the detected upper and lower boundaries to align all rotational images and to stretch or shrink the image to achieve an equal capillary diameter in all images. We compensate for longitudinal motions of the sample along the axis of the capillary by identifying the larva in each of the rotational images by performing an intensity threshold. We then use the tip of the head of the identified larva to dynamically adjust its position in all frames. Any non-uniformity in illumination across the cross-section of the capillary must be corrected prior to reconstruction. Regions of the capillary that are not occluded by the larva can be used to calculate the illumination. Using the position of the tip of the head (identified in the previous alignment step), a region of capillary without larva is selected. By calculating the average pixel intensity distribution at each point from the sidewall to the central axis of the empty region of the capillary, we attain a cross-sectional profile of the illumination and use this to compensate for the non-uniformity of the illumination. To find the COR, we employ a two-step process. We first make a rough estimate of the COR by finding the symmetry axis in a summation image of all rotational images. We detect the symmetry axis by cross correlating the region on one side of the COR with a mirrored image of the other side. This is done for a wide range of the CORs and the one with the highest correlation value is chosen as the initial COR. Using the estimated COR, we perform test reconstructions with a filtered back projection of a fraction of the whole image over a small range of deviations from this estimate COR. The COR position yielding the lowest image entropy is considered to be the closest to the true COR (Walls, Sled et al. 2005) (see Figure 5.9). The image entropy is calculated from the histogram distribution of the grayscale intensity values using (Equation 4).

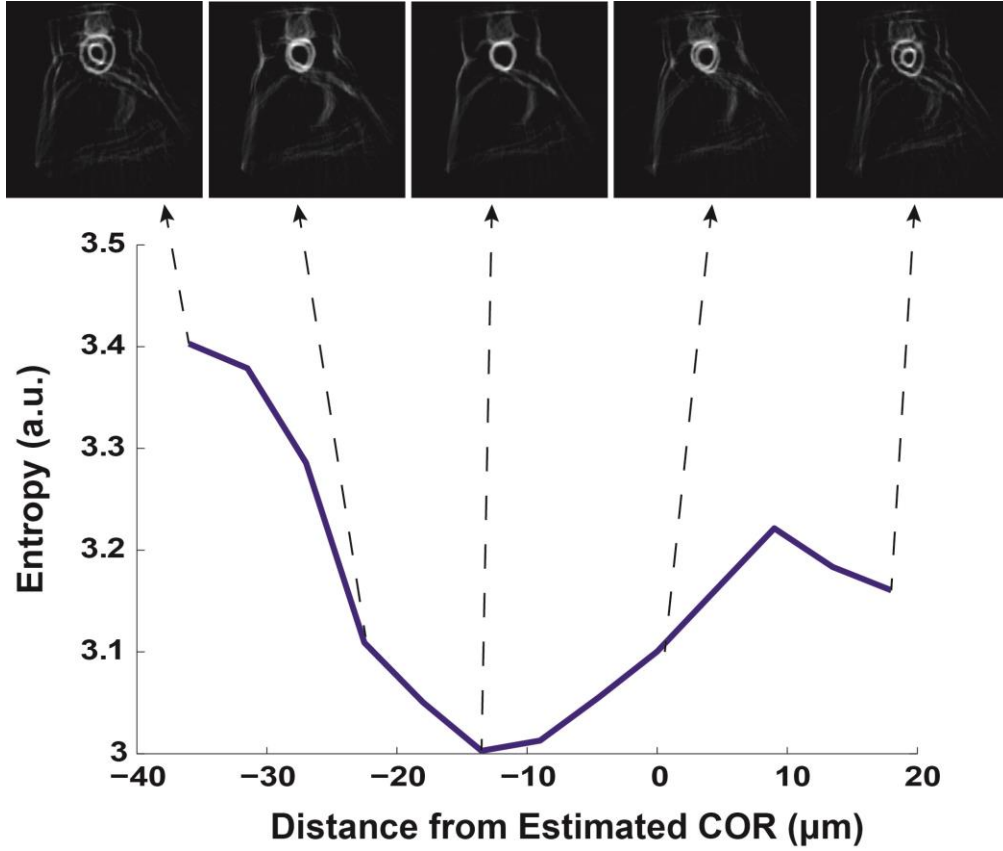


Figure 5.9: Image processing is used to estimate the true center of rotation (COR). Plot shows the measured entropy values for multiple images that have been reconstructed using COR estimates shifted from the original COR estimate (distances represent displacement from the original COR estimate located at $x=0$). Arrows indicate representative reconstructed images for various COR estimates. Images show single transverse slices through the larva using a filtered back-projection algorithm. The reconstruction at the bottom, corresponding to a COR at $-12.5 \mu\text{m}$ from the original estimate, has the lowest entropy and is therefore used as the true COR for the complete 3D reconstruction.

Equation 4: Entropy of a gray scale image from the histogram of its intensity values

$$E = - \sum_p (p \cdot \log_2(p))$$

Where p is the number of values in each histogram bin. Images that have narrow distributions, such as those with well-defined borders result in low entropies. Images with even distribution of gray-scale values result in higher entropies.

5.3.13 *Light ray simulation*

We calculate the refraction at each boundary to trace the rays from light source to detector using the Snell Laws (Equation 5) (see Figure 5.2a-b). A homogeneous collimated source of light originating from below the capillary is modeled as a large collection of parallel rays. The trajectory of each ray is computed using the refraction angles calculated beforehand (see Figure 5.2a). To calculate how these rays reach the detector, we model the microscope lens by creating a virtual CCD (black line in Figure 5.2b) at the microscope's focus plane (i.e. at the geometrical center of the capillary). The trajectories of the rays leaving the capillaries are then propagated back to the virtual CCD without undergoing any refraction (green line in Figure 5.2b). The pixel of the virtual CCD onto which the rays' back propagation falls corresponds to the true pixel in the absence of refraction from the glass capillary. Using this technique we back-track the pixels covered by the rays arriving to each pixel. This information is calculated in advance and fed to the OSEM or FBP algorithms for reconstruction. The light-path tracing is done only once and needs to be repeated only if the microscope's magnification or the capillary is modified.

Equation 5: Snell laws

$$\sin \theta_1 \cdot n_1 = \sin \theta_2 \cdot n_2$$

Where Θ is the angle of incidence and ' n ' the index of refraction of the medium.

5.3.14 *Software*

A custom software in MATLAB was developed to control the platform, to compensate for the motions of the sample, to perform the reconstruction and segmentations, and to analyze the reconstructions.

5.4 *Discussion and Summary*

HCS was developed in late 1990s to apply high-throughput techniques to the study of intact cellular systems. Over the past decade, HCS has become a mainstream technology in the pharmaceutical industry and is employed at all stages of the drug development pipeline.

Increasing public availability of large-scale screening resources, through initiatives such as the Molecular Libraries Program, has also spurred an interest in HCS among academic biomedical researchers. Although HCS offers the potential to capture a vast realm of biological complexity, in practice assays are often constrained by reliance on grossly simplified biological models such as immortalized cell lines and simple culture conditions. Proposals to address these limitations typically focus on transitioning HCS assays into more biologically relevant *in vitro* systems such as primary cells, stem cells, three-dimensional organotypic models, and mixed co-cultures. A more powerful approach would be applying HCS directly to *in vivo* models that more accurately mimic normal development, disease pathology, and systemic responses to perturbing agents. Here, we have demonstrated such an approach.

With only minor modifications, our technology can generate high-resolution 3D reconstructions of any organ or tissue that has been labeled using a suitable chromogenic staining protocol. Of particular relevance for zebrafish researchers, our technology can easily be applied to larvae that have been stained by whole mount *in situ* hybridization (WISH) using antisense riboprobes to visualize gene expression patterns. This can allow virtually any organ, tissue, or underlying signaling pathway to be interrogated under normal and pathological conditions using HIP. When adapting OPT to new stains, it is essential to use a compatible clearing agent that optimizes the optical properties of the fixed tissue in such a way that light scattering is minimized and transmission in the visible spectra is maximized. In the case of Alcian blue, optical clearing is achieved using a 1% trypsin solution followed by equilibration in PBST (see the Methods section). In the case of WISH, optical clearing may require imaging stained larvae in a 2:1 benzyl benzoate:benzyl alcohol (BB:BA) solution, which is compatible with most substrates used for colorimetric detection of alkaline phosphatase activity and allows for almost complete clearing of fixed and yolk-containing tissue.

By coupling high-throughput 3D tomography with automated image analysis, our platform can generate quantitative morphological metrics to create standardized phenomic databases. Phenomic databases produced by HIP can be readily compared between independent

laboratories and across multiple studies. This approach allows the full diversity of morphological phenotypes in a given genetic or chemical screen to be documented and subsequently analyzed using data mining and bioinformatics tools. A major strength of HIP is that it allows for unbiased screens in which mechanistic relationships can be determined without *a priori* knowledge. Using our platform, we are able to cluster chemicals based on their unique hyperdimensional phenotypic signatures and reveal biologically significant correlations that agree with known mechanisms of action in mammals. Importantly, at no point during this study did we need to introduce metrics that would specifically distinguish between different classes of chemicals. Automated quantitative whole-animal phenotyping technologies such as HIP will be particularly important for large-scale initiatives like the Zebrafish Phenome Project, which aims to systematically characterize loss-of-function mutations in every protein-coding gene (Cheng, Xin et al. 2011). In addition, our technology will allow *in vivo* characterization of the diversity of large chemical libraries and natural-product libraries with hard-to-predict targets.

6 Conclusion

6.1 Summary

Large-scale screening of phenotypes induced by drugs, gene mutations, and other agents is essential for modern biology and drug discovery. However, these are generally carried out in *in vitro* models that do not fully preserve the complexity of intact organs nor accurately replicate *in vivo* results. To address these limitations large-scale screens are increasingly being conducted using small model organisms that are amenable to high-throughput methodologies. As discussed in previous chapters the zebrafish larva is an ideal small model organism for *in vivo* high-throughput screening. It is a vertebrate with a high level conservation of drug activity with humans, it has a small size, it is optically transparent, it possesses complex organs and is easy to culture. Despite the zebrafish's ideal features for *in vivo* high-throughput screening, before this work, there were no tools capable of screening at sufficient throughput and resolution to fully exploit of the complexity the zebrafish. This motivated me to focus my graduate work in the engineering and fabrication of tools and systems that allow for sample preparation, imaging and phenotyping of zebrafish at sufficient throughputs to allow large-scale screenings.

To allow rapid sample preparation we demonstrated the vertebrate automated screening technology (VAST), a microfluidic based screening platform capable of handling zebrafish larvae and orienting them for high-resolution imaging inside ultrathin capillaries at throughputs as high as 10 seconds per sample. Our device is designed to operate three linked but independent fluidic sections that allow handling multiple larvae simultaneously. We have also demonstrated that by using simple image-based algorithms we are capable of accurately positioning and orienting each larva in the field-of-view of a microscope in an automated fashion. We have also shown that by enclosing the larvae in capillaries we are able to employ high-resolution high-NA water-dipping lenses that operate with short working distances. These lenses permit the use of accurate imaging and photo-manipulation techniques and allow highly complex assays to be performed

with our system. Here we also provide, with sufficient detail, instructions to replicate our VAST system, the software on which it operates and a detailed step-by-step protocol to fabricate the optical system to couple a femtosecond laser with the imaging on VAST.

To develop a system capable of imaging at sufficient resolution and throughput to allow *in vivo* screening, we used VAST to improve on current optical-projection-tomography techniques. Optical-projection-tomography consists in reconstructing 3D volumes from multiple projections of the sample acquired at a large variety of angles. Our VAST system's capability of rapidly and accurately orienting the larvae under the field-of-view of the microscope allowed prompt acquisition of such projections. To avoid the time consuming steps of immobilization in agar and step-by-step rotation and imaging of the sample, we focused on developing novel image analysis algorithms that dynamically correct for small movements and fluctuations of the capillary and the larvae. This strategy allowed us to acquire 350 images of a larva undergoing a complete rotation in ~2 seconds by means of a high-speed CCD camera. We have shown this technique to work consistently for various chromogenic stains, including immunohistochemistry, whole mount *in situ* hybridization and Alcian blue.

Lastly, we demonstrated novel algorithms to automatically extract hundreds of morphometric measurements from the 3D reconstructions to create hyperdimensional phenotypic signatures of the samples. We performed a proof-of-concept screen looking at the effect of various known teratogen compounds on the formation of craniofacial abnormalities in 5 days post-fertilization zebrafish larvae. By staining the treated samples with Alcian blue and performing our rapid optical-projection-tomography we were able to reconstruct, classify and separate all of the individual bones of the zebrafish craniofacial structures. Our algorithm was then able to extract more than 200 independent morphometric measurements from each sample. These were then used to create phenome-arrays and to perform hierarchical clustering analyses that classify compounds by the similarity of the phenotypes produced. These clustering successfully classified each compound by their known family and mechanism of action.

6.2 Concluding remarks

The three tools demonstrated in this dissertation (i.e. VAST, rapid OPT and hyperdimensional *in vivo* phenotyping) together are able to increase the content and throughput of the screens currently performed in zebrafish larvae.

It is the believe of the author that these tools could form the initial devices on which to build more complex instruments that will ultimately lead to the an earlier introduction of *in vivo* models in the drug discovery pipeline. Earlier introduction of *in vivo* models in the pipeline will not only result in improved efficacy and specificity in the identification of lead compounds, it will also allow researchers to investigate complex diseases that have not yet been able to take advantage of the vast data content and speed of HTS and HCS. This is even more important now, when medicine is moving into an era where the common pathologies of the developed countries are becoming ever more complex (e.g. Alzheimer's disease and Parkinson's disease) and harder to replicate with *in vitro* models.

Besides their application in drug discovery the introduction of the tools presented here has the potential to benefit basic research. The zebrafish community, led by community wide initiatives such as *ZFIN*, *ZIRC* and the *ZMP*, has developed the genetic tools to interrogate a large number of genes for their expression pattern and function. These advances, supported by the instruments we demonstrate here, could form the foundation on which to base other large-scale initiatives like the *Zebrafish Phenome Project*, which aims to systematically characterize loss-of-function mutations in every protein-coding gene.

In conclusion, the work presented in this dissertation has the potential to accelerate both basic and translational research by fully exploiting the innate potential of the zebrafish as an ideal small model organism for large-scale screening studies.

7 Appendix A – Protocol for the construction of a femtosecond laser microsurgery system

Precision and repeatability of *in vivo* neural injury techniques are important for the study of the complex mechanisms of neuronal degeneration and regeneration, as well as for studies of neuronal networks. In particular, femtosecond laser microsurgery allows selective ablation of single neurites *in vivo* with minimal damage to the surrounding tissue.

Here, I present a step-by-step protocol for constructing a femtosecond laser microsurgery setup using a widely available compound fluorescence microscope. The protocol begins with the assembly and alignment of beam-conditioning optics at the output of a femtosecond laser. Then a dichroic mount is installed to direct the laser beam into the objective of a standard inverted microscope. Finally, the laser is focused on the imaging plane of the microscope to allow simultaneous surgery and fluorescence imaging. The protocol can be completed within two days.

7.1 Introduction

In the following protocol, I detail a procedure to add a subcellular-resolution neuronal-ablation capability to a standard fluorescence microscope using commercially available components. Laser micro-surgery is becoming the preferred *in vivo* method for studying neural injury, the function of neuronal networks, and animal development in model organisms such as *C. elegans* and *Danio Reiro* due to its high precision and repeatability (Yanik, Cinar et al. 2004, Yanik, Cinar et al. 2006, Wu, Ferguson et al. 2008) (Biron, Wasserman et al. 2008) (Zhang, Chung et al. 2008) (Supatto 2005, Nishimura, Schaffer et al. 2006, Gabel, Antoine et al. 2008, Hammarlund, Nix et al. 2009, Pardo-Martin, Chang et al. 2010). Femtosecond laser microsurgery can also be integrated with on-chip high-throughput microfluidics to overcome the drawbacks of low-throughput and imprecise manual methods such as mechanical damage and chemical treatments with neurotoxins (Hulme, Shevkoplyas et al. 2007, Rohde, Zeng et al. 2007, Chung, Crane et al. 2008, Guo, Bourgeois et al. 2008, Zeng, Rohde et al. 2008). We previously demonstrated the use

of femtosecond laser microsurgery as a method to study functional neural regeneration in the nematode *C. elegans* and zebrafish (Yanik, Cinar et al. 2004, Yanik, Cinar et al. 2006, Pardo-Martin, Chang et al. 2010), as well as in combination with microfluidic screening chips (Rohde, Zeng et al. 2007, Zeng, Rohde et al. 2008).

To achieve axotomy with sub-cellular resolution in tissue, we use a near-infrared (NIR) laser with femtosecond pulse durations. Tissue is highly transparent to NIR wavelengths, thus allowing laser penetration with minimal out-of-focus absorption. The ablation occurs by multi-photon absorption and chemical decomposition (bond breaking) rather than thermoelastic expansion as with continuous wave lasers or lasers with long pulse widths. In order to achieve multi-photon absorption, photons must coincide in space and time, and be simultaneously absorbed by the tissue (Vogel, Noack et al. 2005). The three-dimensional spatial and temporal coincidence of the photons is achieved by tight focusing of the laser beam via a high-NA objective lens and by the use of temporally compressed (i.e. sub-picosecond duration) laser pulses. This three-dimensionally constrained ablation minimizes damage.

With minimal modifications, the setup presented in this protocol can be utilized for the femtosecond-induced ablation of other commonly operated-upon targets including organelles.

7.2 Materials

In the following pages I present the complete list of both reagents.

7.2.1 Reagents

- Experimental animals. Strains can be labeled with fluorescent protein to allow for easy imaging of the neuronal process for targeting. **CAUTION** All animal experiments must comply with the relevant institutional and national animal care guidelines.
- Cover glass (0.175mm x 25mm x 50mm)
- Microscope cover slides (1mm x 25mm x 50mm)

- Agarose gel 1.5%
- Sodium azide 10mM

7.2.2 Equipment

7.2.2.1 General Equipment

- Femtosecond laser (Spectra Physics Mai Tai HP Ti:Sapphire, tunable-wavelength Class IV laser). More cost-effective femtosecond lasers with a fixed wavelength can also be used including: Del Mar Photonics Ti:Sapphire Custom Made Kit, model TISSA100 and HighQLaser FemtoTrain™, model IC-1045-3000. Minimum recommended pulse energy is ~20 nJ (i.e. average power 1.6 Watts for a laser with 80 MHz pulse repetition rate).
- Laser warning sign and safety equipment which meet requirements set by institutional as well as local and national safety standards. Laser goggles with minimal safety rating of OD7+ are recommended (Kentek, Diode/Nd:YAG 42F goggle, cat. no. KGG-42F)
- Optical table with sufficient surface area (1) (3.0 m × 1.5 m) and set of four air-damped legs (Newport cat. nos. RS-4000-510-12 and I-2000-413.5, respectively).
- Inverted fluorescence microscope system (1) (Nikon Eclipse TI or similar model) including a 70 mm stage-up kit to provide sufficient clearance for the rear-entry of the laser beam and a stage plate capable of holding a standard glass slide.
- Image acquisition software (1) (NIS-Elements 2.0) and compatible computer.
- High resolution CCD camera (1) (Photometrics Coolsnap HQ2)
- RMS-Threaded IR and VIS Alignment Disk (400-640 nm, 800-1700 nm) (1) (Thorlabs, cat. no. RMSIR)
- RMS 45 to CFI 60 Objective Adapter (1) (Nikon, cat. no. MXA20750)
- IR Card (1) (Newport, model no. F-IRC4)
- Infrared viewer (1) (Newport, cat. no. IRV1-2000)

- Optical power meter and detector (1) (Newport, part nos. 1918-C and 818P-010-12, respectively)
- Ø1/2" Post (2") (1) (Thorlabs, cat. no. TR2)
- Ø1/2" Post Holder (2") (1) (Thorlabs, cat. no. PH2-ST)
- Standard Base (1) (Thorlabs, cat. no. BA2)
- Function generator with single-pulse generation capability (1) (BK Precision, model no. 4030) **CRITICAL** If another model or device is used, ensure that the function generator, or any source in general driving the high-voltage amplifier, is capable of driving the input load of the high voltage amplifier. For example if the input impedance of the HV amplifier is 50 Ω and the maximum input voltage is 1V, the function generator must be able to supply at least 20 mA to have access to the full input range.
- Oscilloscope (Tektronix TDS2024)
- 3/8" Corded Drill Driver (1) (RIDGID, model# R70002)
- Drill Set (Ryobi, model# AR2074)
- 1/4"-20 cap and set screws and #8-32 cap and screws (ThorLabs, cat. nos. HW-KIT2, HW-KIT3, respectively)

7.2.2.2 Laser Setup:

- Optical Isolator (1) (Conoptics, cat. no. 712TGG)
- Half-Wave Plate for 600-1050 nm high power applications (1) (Thorlabs, cat. no. AHWP05M-950)
- High Precision Rotation Mount for Ø1" Optics (1) (Thorlabs, cat. no. PRM1)
- Glan-Thompson Polarizer with 600-1050 nm anti-reflection coating (1)(Thorlabs, cat. no. GL10-B)
- Polarizing Prism Mount (1) (Thorlabs, cat. no. SM1PM10)
- Kinematic Mount for thin Ø1" Optics (1) (Thorlabs, cat. no. KM100T)

- Electro-optic modulator (1) (EOM) and requisite high-voltage (HV) amplifier (Conoptics, cat. no. 350-160 E-O modulator with amplifier) **CAUTION:** The cables connecting EOM to the HV amplifier carry high voltage. Only the appropriately rated cables from the EOM manufacturer should be used. A shutter capable of providing a 2.2 ms pulse can be substituted for the EOM, however, the EOM enables the added benefit of two-photon excitation targeting.
- Optical Isolator Mount (1) (Conoptics Model M102, modified to hold the isolator)
- EOM Mount-Labjack (1) (Conoptics Model M102)
- Safety shutter (1) (Electro-optic Products, Corp. SH-10 Interlock Safety Shutter with silver coated mirror, for NIR and DSH-10-110V controller)
- Beam Block, (Includes TR3 Post) (7) (Thorlabs cat. nos. LB1)
- 2" High Universal Post Holder (for use with Beam Blocks) (7) (Thorlabs cat. no. UPH2)
- Ø1/2" Post (2") (3) (Thorlabs, cat. no. TR2)
- Ø1/2" Post Holder (2") (3) (Thorlabs, cat. no. PH2-ST)
- Standard Base (3) (Thorlabs, cat. no. BA2)
- 50-Ω BNC cables of sufficient length (2) to connect the function generator to the oscilloscope and to the high-voltage amplifier. T-joint BNC-cable connector (Cablesnmore.com cat. nos. N23713, X15305, respectively)

7.2.2.3 Dichroic Mounting Adapter

- IR dichroic mirror (1) (Chroma, cat. no. 670dcspxr)
- Nikon Adapter Plate ("Dust Cover") from Nikon 70 mm stage-up kit
- Ø1" (1") Pedestal Pillar Post (1) (Thorlabs, cat. no. RS1P)
- Compact Kinematic Mount (1) (Thorlabs, cat. no. KMS)
- BA1 Standard Base (1) (Thorlabs cat. no. BA1)
- Dichroic Cube Holder (1) (Large aluminum Nikon Filter Cube)
- High Performance Epoxy (1) (Loctite Fixmaster® part no. L08FA12920)

- #8-32 screw x 1/4" with low-profile head (1) (McMaster-Carr, cat. no. 91770A190)

7.2.2.4 Periscope and Beam Expander:

- 40 mm focal length, Ø1", near-IR achromatic doublet lens (1) (Thorlabs, cat. no. AC254-040)
- 200 mm focal length, Ø2", near-IR achromatic doublet lens (1) (Thorlabs, cat. no. AC508-200)
- Single-axis position stage with micrometer (1) (Newport, cat. no. 460P-X)
- Ø1.5" Post Clamp Adapter Plate (1) (Thorlabs, cat. no. C1520)
- 14" tall Ø1.5" Mounting Post (3) (Thorlabs, cat. no. P14)
- Ø1.5" Post Mounting Clamp (4) (Thorlabs, cat. no. C1501)
- Right-Angle Kinematic Cage Mount (2) (Thorlabs, cat. no. KCB1)
- Ø1" Gold Mirror (3) (Thorlabs, cat. no. PF10-03-M01)
- 12" Optical Rail (1) (Thorlabs, cat. no. RLA1200)
- Ø2" Lens Mount (1) (Thorlabs, cat. no. LMR2)
- Ø1" Optics, Translating Lens Mount (1) (Thorlabs, cat. no. LM1XY)
- Ø1" Iris (4) (Thorlabs, cat. no. ID25) (leave in path for easier alignment of lenses)
- Rail Carrier (4) (Thorlabs, cat. no. RC1)
- Ø1/2" Post (2") (7) (Thorlabs, cat. no. TR2)
- Ø1/2" Post Holder (2") (6) (Thorlabs, cat. no. PH2-ST)
- Standard Base (5) (Thorlabs, cat. no. BA2)
- Ultra-Stable Kinematic Ø1" Mirror Mount (1) (Thorlabs, cat. no. KS1)

7.2.2.5 Microscope Optics

- High-Numerical Aperture (NA) objective lens for laser surgery (1). NA greater than 0.7 recommended. Examples: Mag: 20×, NA: 0.75, air lens (Nikon, cat. no. MRD00200). For work with zebrafish axotomy, 25×, NA: 1.1 provides a suitable balance between field of view and NA for quick, efficient axotomy. In the case of

laser surgery on other targets such as objectives with higher magnifications and higher NAs may be used. The optical hardware listed in this protocol is designed to sufficiently fill the back aperture of the objective described above, however, so if a different objective is used for axotomy, then the beam expanding optics must be altered accordingly, as discussed in design of the telescope.

- Fluorescence filter cube for use with the fluorescent reporter protein expressed by the organism (1) (For GFP, Nikon, HQ:F)
- Optical Notch Filter at the Laser Wavelength (1) (Thorlabs cat. no. FES0700)
- Standard Square Cage Plate, SM1 Threaded Inner Bore (1) (Thorlabs cat. no. CP02)
- Epi and brightfield shutters (1) (Sutter cat. no. LB-SC and IQ25-SA)

7.3 Procedure

TIMING: These steps are time independent and may be stopped and started when necessary, however it is imperative that the laser is either properly shuttered or turned off when not in use.

7.3.1 Laser Safety Section

11 CAUTION Prior to initiating the protocol, ensure that the appropriate “Laser in Use” safe signs are installed at the proper locations. Additionally, the laser warning system as well as the laser system itself must comply with the relevant institutional, local, and national laser safety guidelines. It is important to observe good laser safety practice whenever working with the laser, including not wearing reflective items such as jewelry and wrist watches when working near the laser. Use beam blocks to safely terminate the laser beam while aligning. Do not look through the microscope eyepieces when the laser is on and either the internal laser shutter or the safety shutter is open. The laser should be shuttered while inserting components into the beam path. When installing a component into the beam path, use the IR card and/or IR viewer to visualize the location of the beam. Close either the internal laser shutter or the safety shutter (depending on

the component location) and then place the component in the path. Following this, open the shutter and view the location of the beam in relation to the component being aligned. Close the necessary shutter and make more adjustments. If necessary, repeat this on/view-off/adjust cycle multiple times in order to obtain satisfactory alignment.

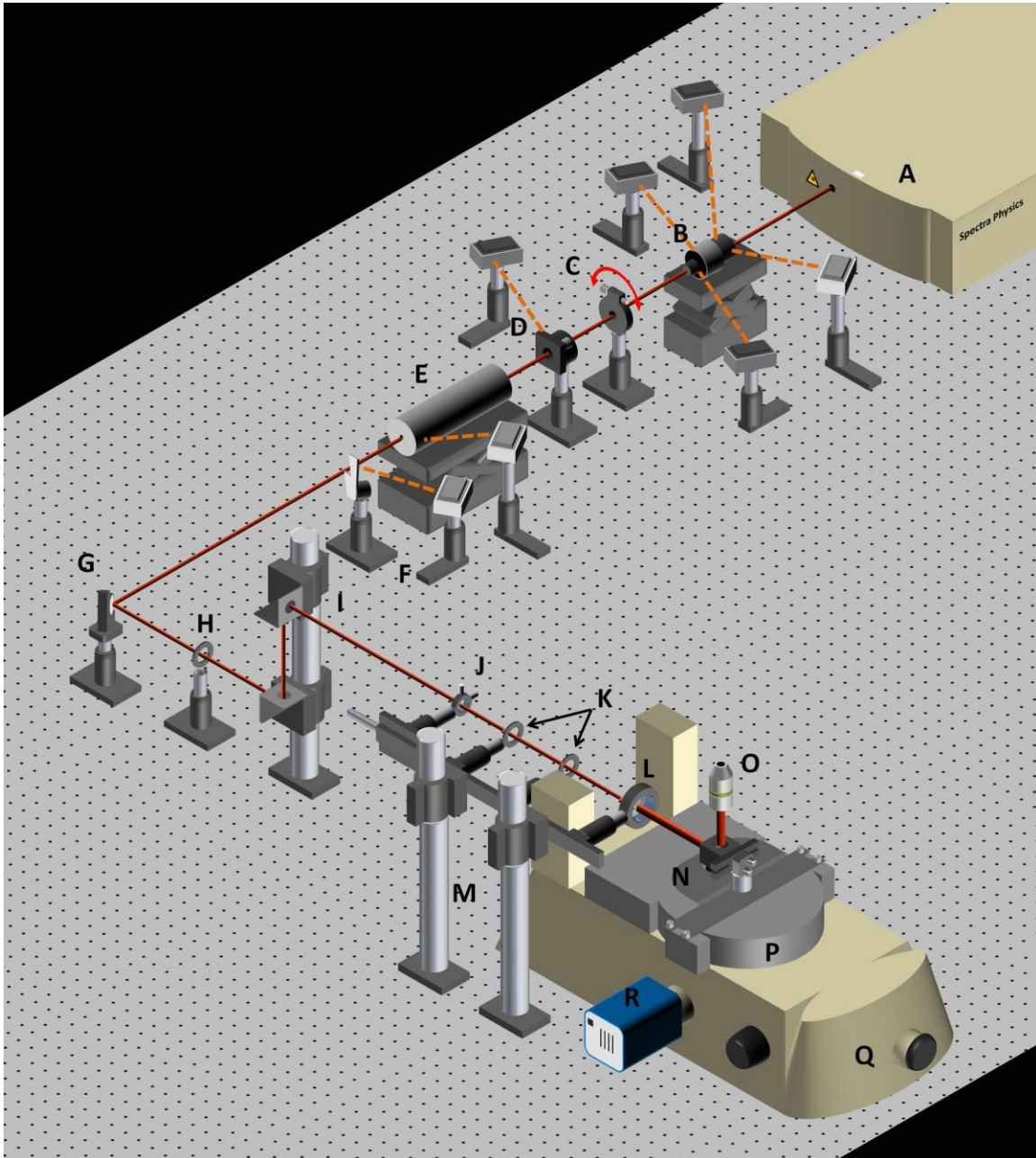


Figure 7.1: Optical system layout. List of components in Table 9.

7.3.2 *Setting up the optical table, laser, power meter, microscope, and optical isolator:*

- 2l Install the optical table. This should be done by the manufacturer.
- 3l Install the femtosecond laser system such that the beam is aligned down the center of the optical table. This should be done by the manufacturer.
- 4l Install the microscope body and supporting equipment at least 1.5 meters from the output of the laser to allow sufficient room for the beam-conditioning optics. Installation of the microscope should be done by the manufacturer.

Table 9: List of components as shown in Figure 7.1

| Component | Description |
|-----------|-----------------------------------|
| A | Femtosecond Laser |
| B | Optical Isolator |
| C | Half-Wave Plate |
| D | Glan-Thompson Polarizer |
| E | Electro-Optic Modulator |
| F | Safety Shutter and Beam Block |
| G | Kinematically Mounted Mirror |
| H | Ø1" Iris |
| I | Periscope |
| J | Ø1" lens L1 on z-adjustable stage |
| K | Two Ø1" Irises |
| L | Ø2" lens L2 |
| M | Beam Expander |
| N | Dichroic Mounting Adapter |
| O | 20 X 0.75 NA Objective |
| P | Epi-fluorescence Filter Turret |
| Q | Lower Half of Microscope Body |
| R | Camera |

- 5l Attach the optical power detector to the power meter. Mount the detector on one of the Ø1/2" posts and insert the post into a Ø1/2" post holder mounted on a standard base (BA2) for easy insertion and positioning of the detector in the beam path. Turn on the attenuator in front of the optical power detector to avoid damage (see manufacturer's manual for details.) Zero the optical power meter to calibrate it for ambient radiation. **CAUTION** It is critical both for user and equipment safety that the power meter is accurately calibrated.

6I Turn on the laser, leaving the internal shutter closed, and allow it to warm up. Set the laser wavelength to 800 nm.

7I Set the output power of the laser to a low yet stable level (~150mW) and ensure that the laser is not pulsing. This state of the laser is used for aligning optical components in steps below.

CAUTION Do not allow the output power of the laser to exceed 200mW.

8I Install the optical isolator (Component B in Figure 7.1) with its mounting hardware in front of the laser to eliminate back reflections. Follow the instructions of the manufacturer for alignment. **CAUTION** The optical isolator contains a powerful magnet that can attract metallic tools such as screwdrivers during installation, causing damage. It is also imperative that sufficient beam block assemblies, composed of one beam block with post (LB1) and one 2" high universal post holder, are placed around the isolator to absorb any beams reflected from the crystal surfaces of the isolator as shown in Figure 7.1 by the dashed orange lines. The placement and number of beam blocks is dependent to the alignment of the optical isolator.

7.3.3 Installing the equipment to control the laser power:

9I Install the half-wave plate (Component C in Figure 7.1) using the high precision rotation mount, one Ø1/2" post, one Ø1/2" post holder, and a standard base (BA2) at the output of the optical isolator. Rotate the half-wave plate mount to the 0° position.

10I Install the Glan-Thompson polarizer (Component D in Figure 7.1) using the polarizing prism mount, the kinematic mount for thin Ø1" optics, one Ø1/2" post, one Ø1/2" post holder, and a standard base (BA2). Place a beam block assembly to absorb the rejected beam.

11I Install the Electro-Optic Modulator (Component E in Figure 7.1) (or high-speed shutter. See equipment list), and place a beam block assembly to absorb the rejected beam. Follow the installation instructions of the manufacturer. **CAUTION** When aligning the EOM, 200 mW or less average power must be used to avoid damage.

12I Install the high-voltage (HV) amplifier (if using EOM), but do not turn it on. Connect the HV amplifier to the EOM using the included high-voltage-rated cables. **CAUTION** The high-voltage-rated cables look similar to standard low-voltage-rated BNC cables. Using improperly rated cables increases the risk of electrocution and may damage equipment.

13I Use a T-joint connector and two 50- Ω BNC cables to connect the output of the function generator both to the input port of the HV amplifier (or high-speed shutter controller) and also to the input of the oscilloscope. To visualize single electrical pulses on the oscilloscope screen, set the oscilloscope to trigger and hold on the rising edge at 0.5 V. Consult the oscilloscope manufacturer's manual for detailed operation instructions.

14I Set the function generator to produce a square pulse with a 2.2 ms duration and 1.0 V amplitude (or the voltage required by the high-speed shutter control). Consult the function generator manufacturer's manual for detailed operation instructions.

15I Mount the safety shutter using one $\varnothing 1/2$ " post, one $\varnothing 1/2$ " post holder, and a standard base (BA2) as well as a beam block assembly to serve as a rejected beam dump (Components F in Figure 7.1). Using the IR card and IR Viewer, adjust the position of the safety shutter and the beam block such that the beam is not clipped when the safety shutter is open and the beam is reflected into the center of the beam block when the safety shutter is closed.

16I Close both the internal laser shutter and the safety shutter.

17I Turn the laser to its maximum emission power and ensure that it is pulsing. For the MaiTai HP laser the expected maximum emission power is approximately 3.0 Watts at 800 nm.

TROUBLESHOOTING

18I Place the optical power detector at the output of the EOM. Turn on the HV amplifier. Open the internal laser shutter and adjust the position of the detector to maximize the power read.

19I Adjust the bias voltage of the HV amplifier until the measured power reaches its minimum.

20l Turn off the HV supply.

21l Rotate the half-wave plate (component C in Figure 7.1) until the power measured is appropriate for surgery: For axotomy, 1.2 Watts is sufficient when using a 20× objective lens with NA=0.75 and a 2.2 ms exposure time. For higher NA or longer exposure times, lower power levels are sufficient (Vogel, Noack et al. 2005).

22l Turn on the HV amplifier and record the value on the power meter. This is the minimum amount of transmitted laser power. The ratio of the power set in step 21 to this value gives the contrast ratio of the laser power at the sample. A ratio of at least 50 is desirable.

TROUBLESHOOTING

23l Close the internal laser shutter.

24l Remove the power detector from the beam path.

7.3.4 Assembly of the dichroic mounting adapter:

25l Mount the dichroic mounting adapter in order to direct the laser beam into the objective lens without interfering with the normal optical paths of the microscope. The dichroic mounting adapter, shown in detail in Figure 7.2, is composed of the dichroic mirror, the Nikon adapter plate from the 70 mm stage-up kit for a Nikon Eclipse TI, one Ø1" (1") pedestal pillar post, one compact kinematic mount, one standard base (BA1), one dichroic cube holder.

26l Mount the dichroic mirror in the dichroic cube holder. **CRITICAL** Ensure that the coated side of the dichroic mirror is facing the laser.

27l Glue the dichroic cube holder to the standard base (BA1) using two-part epoxy following the diagram in Figure 7.2.

28l Glue the compact kinematic mount to the standard base using two-part epoxy following the diagram in Figure 7.2. **CRITICAL** To ensure the components are glued properly, place the assembly upside-down on a flat surface overnight while the epoxy cures.

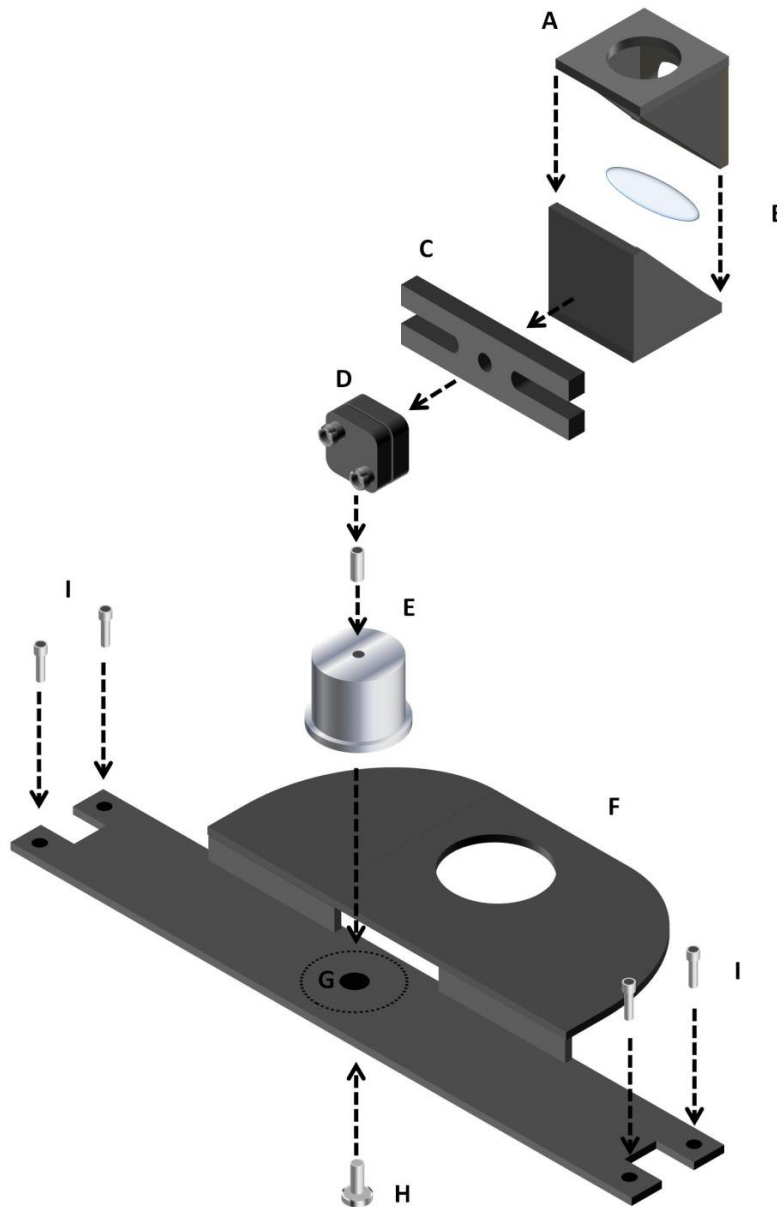


Figure 7.2: An exploded view of the dichroic mounting adapter. The dichroic mounting adapter is composed of a metal filter cube (A), which contains an IR dichroic mirror (B). The filter cube is attached to a BA1 standard base (C) using glue. The opposite face of the BA1 standard base attaches to a 2-axis compact kinematic mount (D) also using glue. The compact kinematic mount is attached to a Ø1" (1") pedestal pillar post (E) with a #8-32 x 1/4" set screw. The assembly comprising components A through E mounts to a Nikon adapter plate from a 70 mm stage-up kit (F) so that the dichroic mirror sits in the beam path. This is accomplished by drilling a hole (G) and using a #8-32 x 1/4" screw (H) to position the dichroic mirror over the opening in the adapter plate. The entire assembly is affixed to the microscope using screws (I) included in the 70 mm stage-up kit. Figure 7.1 shows the location of the dichroic mounting adapter on the microscope.

29I Attach the pedestal pillar post to the compact kinematic mount using one #8-32 × 1/4" set screw.

30I Hold the dichroic cube holder so that the dichroic mirror is centered above the large hole in the Nikon adapter plate. Use a marker to draw a circle on the Nikon adapter plate around the bottom of the pedestal pillar post.

31I Using a hand-held power drill, make a 0.25" hole in the Nikon adapter plate at the center of the marked circle as shown in Figure 7.2.

32I Use a low-profile #8-32 × 1/4" screw to attach the pedestal post to the dust cover through the hole drilled in **step 31**.

33I Attach the completed dichroic mounting adapter (Component N in Figure 7.1) to the top of the microscope's fluorescent filter turret (Component 'P' in Figure 7.1) using the screws and hardware included in the 70 mm stage-up kit.

7.3.5 Assembly of the periscope

34I Construct a periscope (Component I in Figure 7.1) using one Ø1.5" Mounting Post, one BA2 standard base, two right-angle kinematic cage mounts, two Ø1" gold mirrors, and two Ø1.5" Post Mounting Clamps. Place the periscope assembly on the optical table as shown in Figure 7.1 so that it will be able to direct the beam into the laser entry port of the microscope.

35I Install a Ø1" gold mirror in the ultra-stable kinematic Ø1" mirror mount.

36I Repeat **Step 7** to lower the laser output power.

37I Turn off the HV amplifier.

38I Mount the ultra-stable kinematic Ø1" mirror mount using a one Ø1/2" post, one Ø1/2" post holder, and a standard base (BA2) (Component G in Figure 7.1) on the optical table. Open the internal laser shutter and the safety shutter. Coarsely align the kinematic mirror to center the

laser on the periscope's lower mirror. Close the safety shutter and secure the kinematic mirror to the optical table.

39I Place a Ø1" iris at the input of the periscope (Component H in Figure 7.1). This iris will ease the process of realignment when needed.

40I Coarsely align the periscope to direct the laser horizontally into the back port of the microscope.

41I Adjust the angle of the lower periscope mirror to center the laser on the upper periscope mirror.

42I It may be necessary to repeat steps **37 through 40** several times iteratively in order to obtain a satisfactory alignment.

43I Close both the safety shutter and the internal laser shutter.

7.3.6 Assembly of the laser beam expander:

44I Determine the focal lengths of lenses L1 and L2 needed to fill the back aperture of the objective used for axotomy. In this protocol, the laser beam diameter of 3 mm must be expanded to fill the 15mm-in-diameter back aperture of the objective lens, and therefore the beam must be expanded five-fold. The amount of expansion is determined by the ratio of the focal length of the lens L2 to that of lens L1, which in this protocol is $200 \text{ mm} / 40 \text{ mm} = 5$. The distance between the lenses is the sum of their focal lengths f_1 and f_2 as shown in Figure 7.4, which in this protocol is $40 \text{ mm} + 200 \text{ mm} = 240 \text{ mm}$.

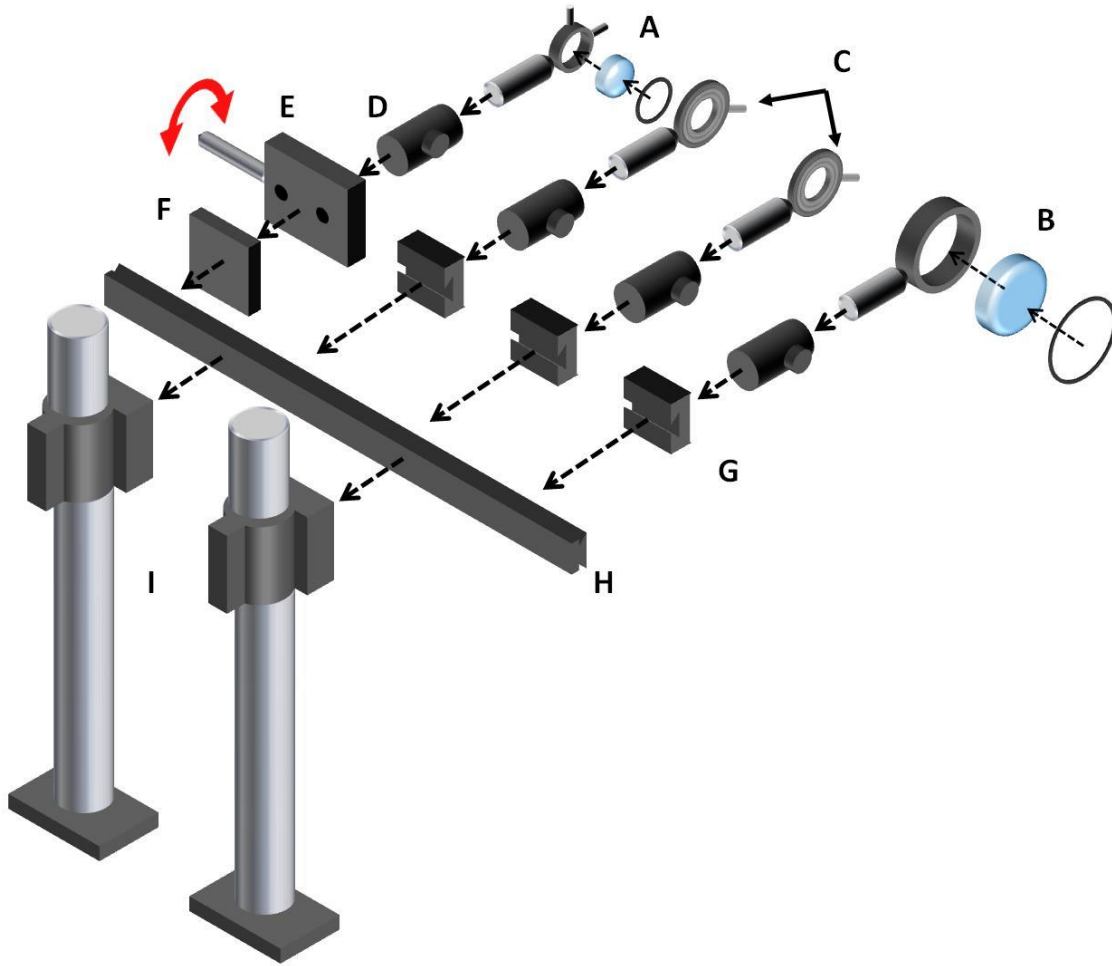


Figure 7.3: An exploded view of the beam expander. Lenses L1 and L2 (A and B, respectively) sit in their mounts which are attached to $\varnothing 1/2''$ posts. Two $\varnothing 1''$ irises (C) are also attached to $\varnothing 1/2''$ posts. All four posts sit securely in $\varnothing 1/2''$ post holders (D), one of which is attached to a single-axis stage with rotatable micrometer (E) and $\varnothing 1.5''$ post clamp adapter plate (F) while the remaining three are attached to rail carriers (G). These four assemblies firmly attach to the 12" optical rail (H) which is mounted to the two $\varnothing 1.5''$ posts via two $\varnothing 1.5''$ post mounting clamps (I). The entire assembly is mounted using BA2 standard bases.

451 Construct the beam expander following the diagram in Figure 7.3 using two $\varnothing 1.5''$ mounting posts, two standard bases (BA2), two $\varnothing 1.5''$ post mounting clamps, one 12" optical rail, three rail carriers, one single-axis position stage with micrometer, one $\varnothing 1''$ translating lens mount, one $\varnothing 2''$ lens mount, and four $\varnothing 1/2''$ post holders.

46l Place the beam expander on the optical table next to the microscope as shown in Figure 7.1. This positioning of the beam expansion optics close to the microscope has two primary benefits: First, it allows for a single person to (re)align the setup, thus facilitating quick troubleshooting. Second, it reduces the amount of real estate on the optical table consumed by the optics.

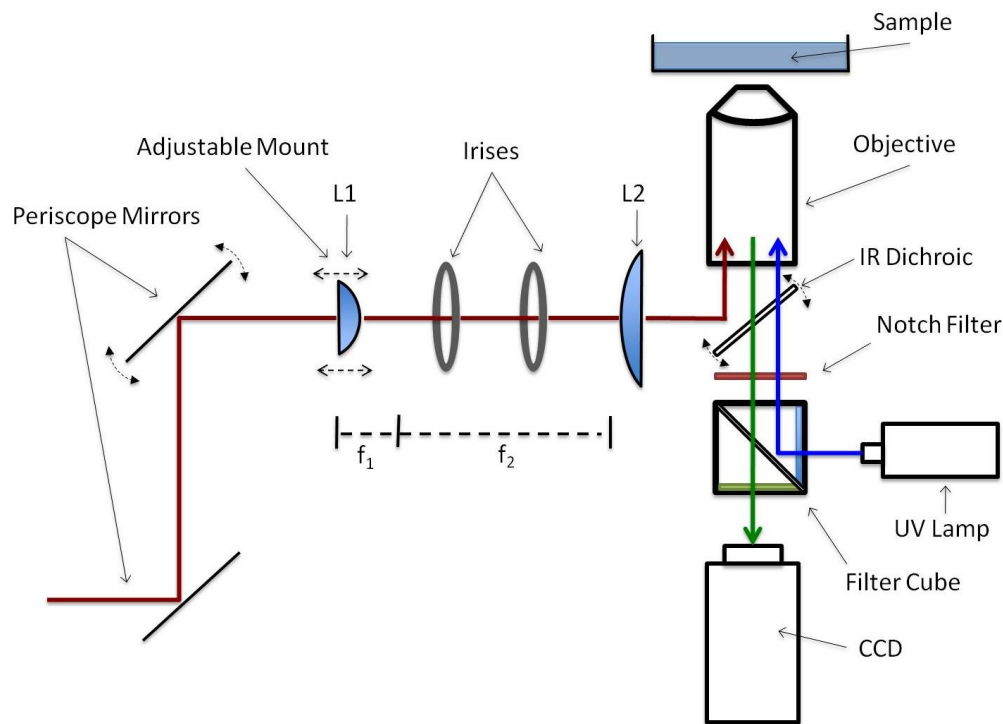


Figure 7.4: Optical path for simultaneous epi-fluorescence imaging and laser axotomy. The femtosecond laser, indicated by the red line, passes through beam conditioning optics before being directed up by the NIR dichroic mirror into the back aperture of the objective lens. The epi-fluorescence excitation, indicated by the blue line, is simultaneously directed into the back aperture of the objective lens by the filter cube. The fluorescence emission, indicated by the green line, passes through multiple filters and is captured by the camera.

47l Use a bubble level to ensure the 12" optical rail is level. The rail carriers slide onto the optical rail and are hand-tightened with the included screws. The single-axis position stage with micrometer is mounted using cap screws.

48I Space the outer Ø1/2" post holders by a distance equal to $f_1 + f_2$. The distance between these two Ø1/2" post holders is finely adjusted below in the protocol.

49I Lower the laser power as in **step 7**.

50I Completely close the iris closest to the objective. Close the remaining two irises leaving an aperture of approximately five millimeters.

51I With the aid of the IR viewer and IR card, adjust both the height and the angle of the upper periscope mirror until the laser beam passes through the two open irises.

52I Open all three irises.

53I Center the beam on the dichroic mirror by adjusting only the height of the upper periscope mirror and the position of the periscope assembly on the optical table. If the periscope assembly is displaced, repeat **steps 38 through 41** to re-center the beam on the lower periscope mirror.

54I Close all three irises leaving an aperture of approximately five millimeters. Adjust the height of the 12" optical rail until the laser passes through all three irises. Use a bubble level to ensure the 12" optical rail is level. **TROUBLESHOOTING**

55I Close both the safety shutter and the internal laser shutter.

7.3.7 Coarse alignment of the laser

56I Construct the IR alignment tool by drilling a 1/8" diameter hole through the center of the RMS-threaded IR alignment disk and then insert the modified IR alignment disk into an RMS 45 to CFI 60 Objective Adapter. **CAUTION** The alignment disk is built from brittle plastic so drilling must be done with care.

57I Thread the completed IR alignment tool into the microscope nosepiece.

58I Place a cover glass on the stage plate to act as a reflecting surface for laser alignment.

59I Lower the laser power for alignment as in **step 7**.

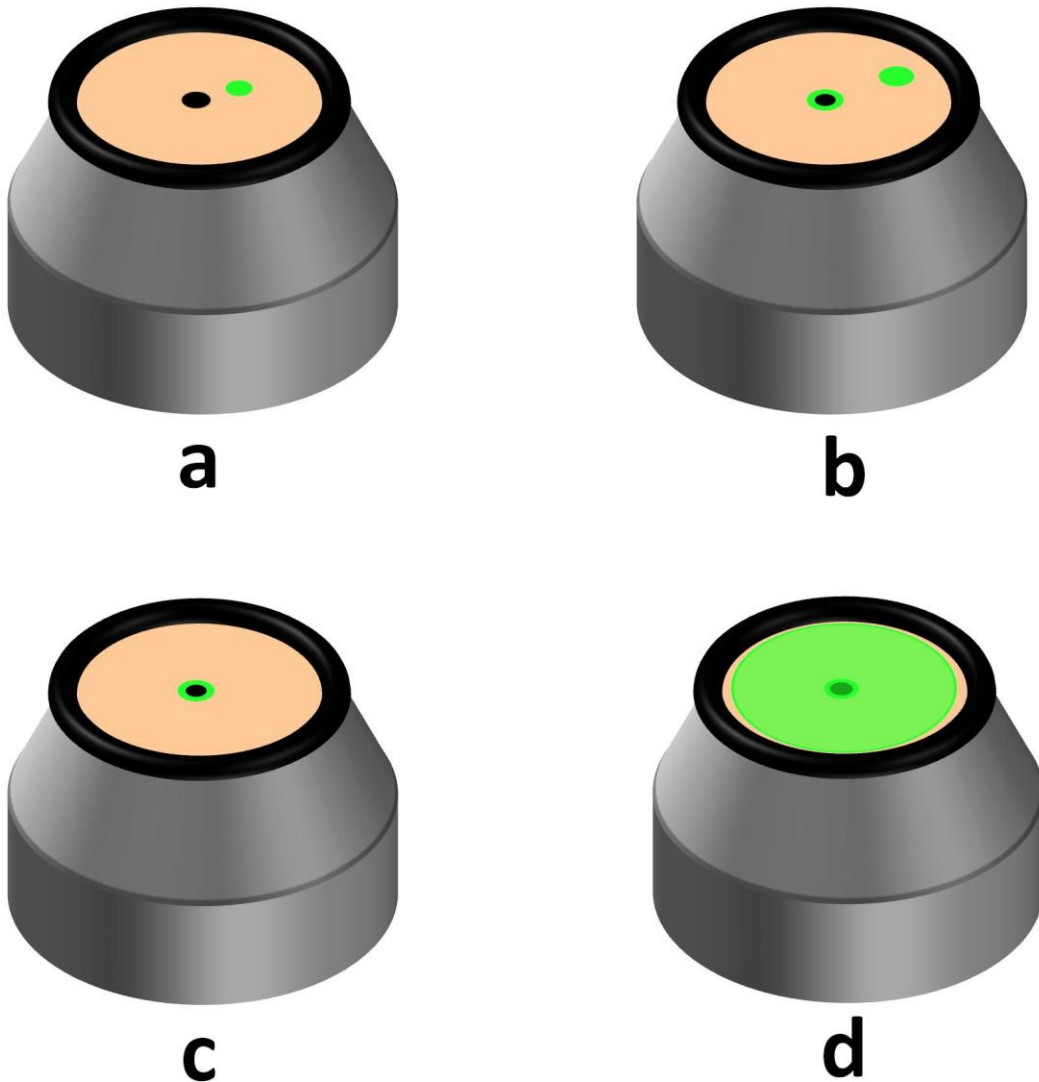


Figure 7.5: Use of the IR alignment tool. The IR alignment tool is composed of a RMS IR-aligning disk and a RMS 45 to CFI 60 objective adapter. Without lenses L1 and L2, the transmitted beam is directed to the center of the dichroic mirror resulting in a glowing spot on the field of the disk (a). Adjusting the dichroic mirror causes the transmitted beam to pass through the center hole and an additional spot caused by the reflection of the beam from the cover glass appears on the field of the disk (b). The reflected spot is caused by the non-normal incidence of the transmitted beam on the cover glass. Moving the transmitted spot half-way towards the initial location of the reflected spot by adjusting the upper periscope mirror and then moving the transmitted spot back to the center hole by adjusting the angle of the dichroic mirror, achieves normal incidence of the beam on the cover glass. Normal incidence is indicated by both reflected and transmitted beams passing through the center (c). Inserting both lenses L1 and L2 into the beam path (Steps 68-70), results in a large, symmetric circular illumination on the IR alignment tool (d).

- 60I** Tilt the condenser arm away from the stage to facilitate viewing of the IR alignment tool.
- 61I** Open the internal laser shutter and the safety shutter.
- 62I** Using the IR viewer, observe the top of the IR alignment tool as shown in Figure 7.5.
- CAUTION** Do not hold the IR viewer directly in the beam path as this could result in damage to the IR viewer.
- 63I** If the laser is not passing through the center hole then a glowing dot will appear on the surface of the IR alignment tool as shown in Figure 7.5a. Use the compact kinematic mount of the dichroic mounting adapter to center the laser on the IR alignment tool. **TROUBLESHOOTING**
- 64I** If the laser beam is not normal to the cover glass two spots will appear on the surface of the IR alignment tool as shown in Figure 7.5b: a glowing ring around the center hole (the “transmitted beam spot”) and a spot off to the side (the “reflected beam spot”).
- 65I** Note the location of the reflected beam spot.
- 66I** Adjust the angle of the upper periscope mirror to move the transmitted beam spot approximately half the distance towards the initial location of the reflected beam spot (from the previous step). In doing this, the reflected beam spot will itself move and may disappear since the transmitted beam is no longer passing through to the cover glass. **TROUBLESHOOTING**
- 67I** Adjust the angle of the dichroic mirror using the compact kinematic mount of the dichroic mounting adapter to bring the transmitted beam spot back to the center hole. The reflected beam spot should move back towards the center hole at approximately twice the rate as the transmitted beam spot, and they will meet in the middle as shown in Figure 7.5c. **TROUBLESHOOTING**
- 68I** Close the safety shutter. Insert L2 making sure that the curved surface of the lens faces away from the objective.
- 69I** Open the safety shutter. Using the IR viewer, observe the IR alignment tool and center the transmitted beam spot by adjusting the position and pitch of L2. **TROUBLESHOOTING**
- 70I** Close the safety shutter. Insert L1 making sure that the curved surface faces L2.

71I Open the safety shutter. Using the IR viewer, observe the IR alignment tool and center the transmitted beam spot by adjusting the position and pitch of L1 using both the Ø1/2" post and the Ø1" translating lens mount. Note that the transmitted beam spot will be larger and diffuse after inserting L1 as shown in Figure 7.5d. Ensure that the beam is not clipped (i.e. the transmitted beam spot should be a full, symmetric, circular disk on the IR alignment tool).

TROUBLESHOOTING

72I Close the safety shutter and internal laser shutter.

7.3.8 Fine alignment of the laser and image focal planes

73I Insert the objective to be used for surgery. Make sure that no filter cube is in the active slot of the epi-fluorescence filter turret. Turn on the HV amplifier and adjust the half-wave plate as discussed in **steps 18 through 22**.

74I Close the internal laser shutter and the safety shutter.

75I Draw lines on a clean cover glass using a non-water-based permanent marker (e.g. Sharpie™). Place the cover glass on the stage plate. **CRITICAL** Use only a single pass with the marker as a thick coating will not allow the laser to produce thin cuts.

76I Turn on the camera and image acquisition software.

77I Open the internal laser shutter and the safety shutter.

78I Locate the image of the laser in the preview window of the image acquisition software. Center the beam in the preview window by adjusting the angle of the dichroic mirror using the compact kinematic mount of the dichroic mounting adapter. **TROUBLESHOOTING**

79I Mark the position of the laser on the computer monitor with a piece of tape. **CRITICAL** Do not move the image acquisition software preview window after marking the beam location.

80I Close the internal laser shutter and the safety shutter.

81I Insert the laser notch filter into a 30 mm standard square cage plate.

82I Insert the laser notch filter between the dichroic mirror and the microscope epi-fluorescence filter turret.

83I Tilt the condenser arm to its original upright position. Turn on the brightfield source, adjust the exposure of the camera, and focus on the edge of a marker line. Move the stage to position the edge of a marker line under the piece of tape on the computer monitor.

84I Open the safety shutter. Depending on the locations of L1 and L2 set in **steps 67 through 70** the region of marker underneath the tape will be ablated to varying degrees of sharpness, symmetry, and size. While staying focused on the edge of the marker line, adjust the position of L1 along the optical rail using the micrometer to adjust the focus of the laser beam to increase the sharpness of the ablation. Additionally, adjust L1 using its translating mount axes to further improve the shape of the ablation. **TROUBLESHOOTING.**

85I Characterize the laser alignment by using the single-pulse button on the function generator to generate spots and compare the result to the images in Figure 7.6.
TROUBLESHOOTING

86I Close the safety shutter and the internal laser shutter.

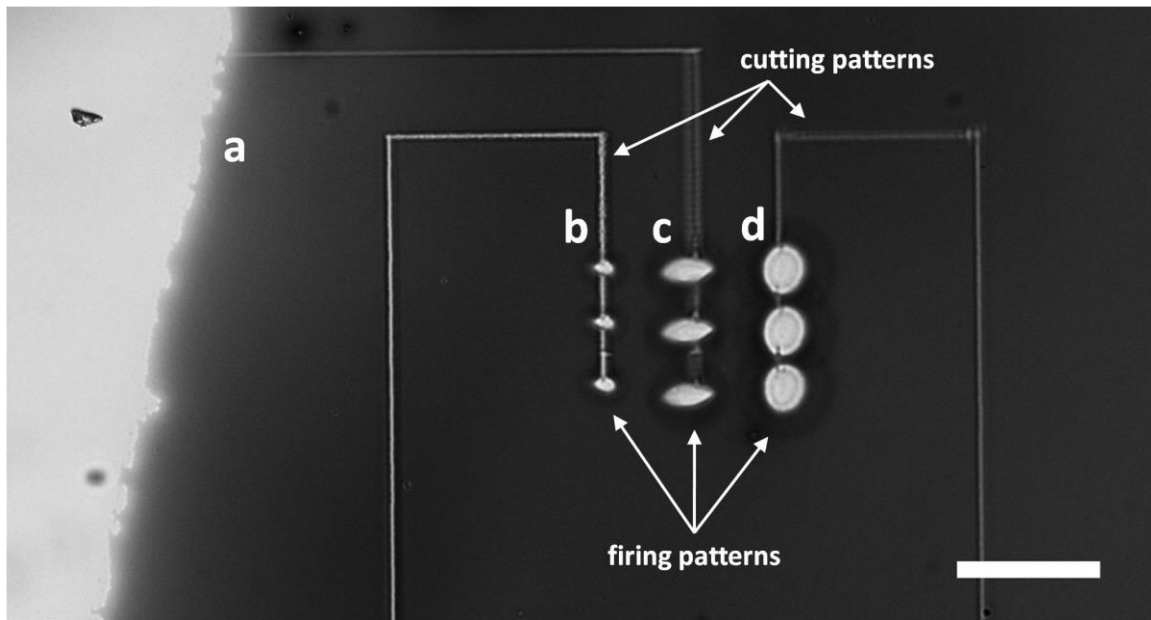


Figure 7.6: Ablated patterns in permanent marker on cover glass under different alignment conditions. When the image plane is focused on the boundary of the marked and unmarked glass surfaces (a), and when the system is properly-aligned, the resulting cutting pattern is narrow and symmetric, while the firing pattern is relatively small and also symmetric (b). If the beam is clipped and/or lenses L1 and L2 are misaligned, the cutting pattern is wider in one direction than the orthogonal direction. Additionally the firing pattern becomes asymmetric (c). If the laser is out of focus, the cutting pattern is blurred and the firing pattern is larger (d). Scale bar is 50 μm .

7.3.9 Laser axotomy on in-vivo and in-vitro samples

TIMING: These steps are time dependent and must be completed within 30 minutes once the anesthetic has been administered to ensure minimal toxic effects.

- 871 Prepare the microscope for fluorescence imaging, and remove the laser notch filter.
- 881 Turn on the HV amplifier and adjust the half-wave plate as discussed in **steps 18 through 22**.
- 891 Open the internal laser shutter and the safety shutter.
- 901 Locate the image of the laser in the preview window of the image acquisition software and adjust the piece of tape on the monitor if necessary. **TROUBLESHOOTING**

911 Close the safety shutter and return the laser notch filter to its position above the microscope filter turret.

921 In-vivo laser axotomy

1. Immobilize the zebrafish larvae on a cover glass using standard procedures. Place the cover glass on the stage plate. Ensure that the animal is as close to the cover glass as possible.
2. Using fluorescence imaging, locate the animal and move the stage to bring the axon or cell to be ablated directly under the piece of tape. Bring the target axon or cell into focus.
3. Open the safety shutter and use the two-photon excitation to fine tune the focus onto the axon.
4. Press the single-pulse button on the function generator to ablate the target axon or cell. Immediately close the safety shutter to avoid damaging the organism/cell. **TROUBLESHOOTING**.
5. Recover the animal using standard procedures.

In-vitro ablation of sub cellular structures:

1. Cells to be ablated should be cultured on a no.1 (0.17 mm) glass bottom multi-well plate to allow for high quality imaging.
2. Transfer the cell-cultured multi-well to the microscope and bring the cells to be ablated into focus. Bring the targeted structure directly under the piece of tape and bring it into focus with the objective calibrated for the surgery.
3. Open the safety shutter and if the targeted subcellular structured is fluorescence label, use the two-photon excitation to fine-tune the focus onto the subcellular structure.
4. Press the single-pulse button on the function generator to ablate the target axon or cell. Immediately close the safety shutter to avoid damaging the organism/cell. **TROUBLESHOOTING**.

931 At the end of the experiment, close the safety shutter and internal laser shutter. Turn off the laser and the fluorescence and brightfield sources.

7.4 Anticipated results

7.4.1 Characterization of the femtosecond laser surgery system

The setup described in this protocol produces a circular laser spot with a full-width-half-maximum (FWHM) of $1.7\ \mu\text{m}$ at the focal plane (See Figure 7.7). An objective with a higher numerical aperture can be used to generate a smaller laser spot size at the expense of the working distance and/or the field of view. Using the components described in this protocol, the total power loss between the output of the EOM and the sample is 47.5%.

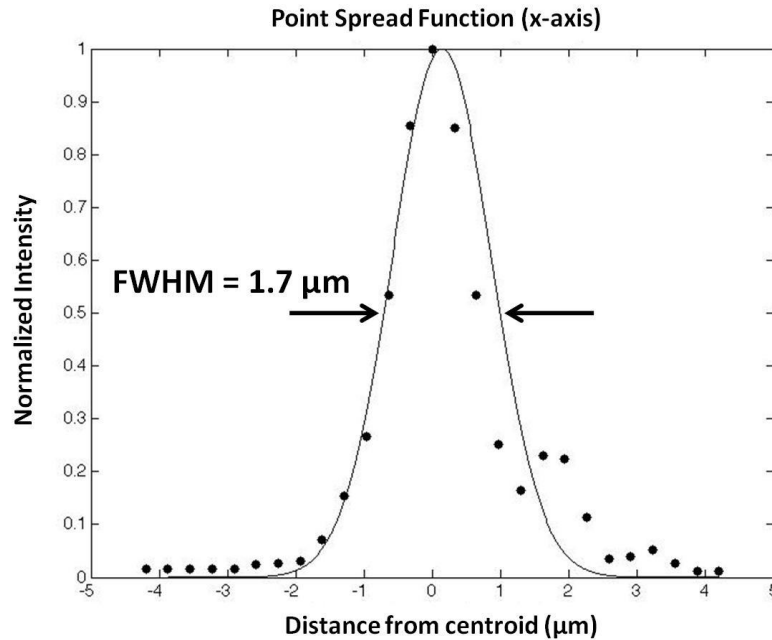


Figure 7.7: Point spread function of the laser at the focal plane. The system described in this protocol generates a circular laser spot at the sample with a full-width-half-maximum of $1.7\ \mu\text{m}$.

7.4.2 Femtosecond axotomy of *C. elegans* mechanosensory neurons

With a $20\times$ ($\text{NA} = 0.75$) objective, we use a 1.20 Watt (measured at the output of the EOM, which corresponds to 0.63 Watts at the sample), 2.2 ms-long laser pulse train to perform axotomy on *C. elegans zdl5* strain (GFP-labeled mechanosensory neurons) (See Figure 7.8). Although low-magnification objective lenses have lower numerical apertures, they allow simultaneous

visualization of the cell body and large portions of the axons, enabling surgery of the axons at precisely measured distances from the soma.

Lower laser power and shorter pulse trains can be used, however the reproducibility of surgery decreases at lower powers in part due to increased sensitivity to laser focus. In addition, it becomes difficult to distinguish photodamage from photobleaching. Photobleaching is often followed by spontaneous recovery of fluorescence in the axon at the site of injury within a few minutes, whereas photodamage leads to permanent non-fluorescent regions. The threshold power levels for photobleaching versus photodamage can be characterized using dye-filling techniques (Yanik, Cinar et al. 2004, Yanik, Cinar et al. 2006). Conversely, higher laser powers and/or longer pulse trains often result in extensive scarring, causing widespread injury to the animal (Vogel, Noack et al. 2005).

Upon ablation, we often observe fluorescent protein leaking from the axon terminals and diffusing into the surrounding area. The brightness of the axon terminals decreases initially, and recovers within several minutes, while leaving a non-fluorescent region at the site of surgery. Within several minutes both the proximal and distal axon terminals retract by several microns (arrow 2 in Figure 7.8b). Within few hours, the proximal axon terminal starts regrowing (arrow 3 in Figure 7.8b) (Yanik, Cinar et al. 2004). The regrowing proximal axon terminal may also fuse with the distal axon terminal (Yanik, Cinar et al. 2006).

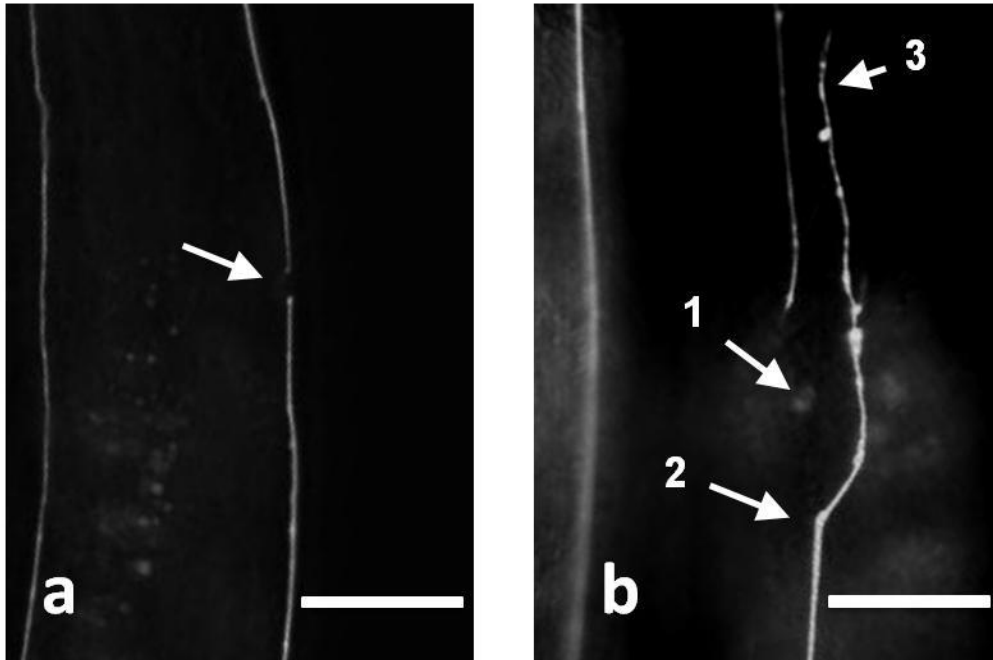


Figure 7.8: Femtosecond laser microsurgery. (a) A highly localized region (arrow) of a mechanosensory neuron is ablated using the system described in this protocol. (b) Following surgery at point 1, the ablated process first retracts to point 2, and then regenerates to point 3. Scale bar 10µm.

7.5 Timings

Setting up the optical table, laser, power meter, microscope and optical isolator: 6 hours;

Installing the equipment to control the laser power: 2 hours;

Assembly of the dichroic mounting adapter: 1 hour + 24 hour pause;

Assembly of the periscope: 1 hour;

Assembly of the laser beam expander: 1 hour;

Coarse alignment of the laser: 30 min;

Fine alignment of the laser and image focal planes: 1 hour;

In-vivo laser axotomy: 15 min;

Table 10: Troubleshooting table for each step of the protocol for the construction of a femtosecond laser surgery system.

| Step | Problem | Possible Reason | Solution |
|-------|---|--|--|
| 17 | Laser is not pulsing | Optical isolator is not functioning properly, allowing back reflections into the laser | Check optical isolator manual and ensure the component is aligned correctly |
| 22 | Power Ratio at EOM is insufficient | EOM is misaligned or damaged | Realign and/or consult manufacturer |
| | | Bias voltage for HV amplifier is incorrect | Repeat step 19 |
| 54 | The beam will not pass through all three irises | The 12" optical rail is not parallel to the beam path | Rotate the beam expander structure to bring the 12" optical rail parallel to the beam path |
| 63 | Cannot find laser spot on the IR alignment tool | Dichroic mirror is severely misaligned | Adjust the rotation of the dichroic and/or compact kinematic mount on the adapter plate |
| 66,67 | Transmitted beam spot disappears when moved | The beam is being clipped | Adjust the position/rotation of the Ø1" pedestal pillar post; |
| 69 | The beam spot cannot be properly centered using only L2 | The laser beam is not passing through the center of L2 | Adjust the beam expander hardware, in particular the height of the 12" optical rail from the table |
| 71 | Expanded beam shape is asymmetric/irregular | Clipping of the beam and/or poor orientation of the lenses | Check alignment using IR viewer and IR card and correct the misaligned components |
| 78 | Cannot find laser in preview window | Beam may not be falling on the CCD of the camera. | Rotate the camera in its mount if the sensitive area is particularly small. |
| | | Filter cube may be in the active slot of the epi-fluorescence filter turret and may be blocking the laser beam | Remove the filter cube |
| 84 | Cannot obtain sharp cuts on the permanent marker | Imaging and laser plane of focus are mismatched | Find both planes of focus; if laser plane is below imaging plane, move L1 closer to L2 r; if laser focus is above, move lenses apart |
| | | Laser is not pulsing | Change the settings of the laser to pulsing mode or go to troubleshooting of step 17 |
| 85 | Firing pattern is asymmetric or large | Clipping of laser beam | Trace the beam path using the IR card to determine the point of clipping and correct the misalignment |
| | | Misalignment of lenses | Realign the lenses |
| | | Laser is not focused on the image plane | Adjust the position of L1 along the 12" optical rail using the micrometer |
| | | Power level is too high | Verify the high-power level using steps 18-22 |
| | | Laser is not centered on or overfilling the back aperture of the objective lens | Redo steps 64-72 to align the incoming beam on the back aperture of the objective |
| | The position of cuts shifts when focusing | Non-normal incidence of laser beam onto the back aperture of the objective | Redo steps 64-67 to correctly orient the incoming beam |
| 90 | Laser spot has moved since last usage | The alignment of components have changed | Check alignment using IR viewer and IR card and correct the misaligned components |
| 94 | Failure to successfully ablate the target | Laser is not focused on the image plane | Repeat steps 73-86 |
| | | Energy of the laser is too low | Check maximum power of the beam using power detector at the output of the EOM; see step 18 |
| | | Target is too deep in the tissue for efficient cutting; excessive scattering | Reorient the sample |
| | | Laser is not pulsing | Change the settings of the laser to pulsing mode or go to troubleshooting of step 17 |
| | | Laser pulses are significantly broadened | Analyze the path for portions which cause dispersion and replace components with ones suited for high-speed NIR lasers |
| | Specimen is damaged while at low power | Minimum transmitted power is too high | Check/Correct EOM bias voltage and the rotational angle of the half-wave plate |

8 Acknowledgements

This thesis is the result of the research conducted at the *Research Laboratory of Electronics* (RLE) and MIT, Cambridge, United States. I would like to express my sincere gratitude and appreciation towards all those people who have contributed, directly or indirectly, to this thesis.

8.1 Advising

I thank Dr. Yanik, Dr. Eimon and Dr. Smith for their academic and research advice on the work presented here and through my years at Harvard and MIT.

8.2 Research Funding

We thank the following funding sources: NIH Transformative Research Award (R01 NS073127), NIH Director's New Innovator award (1-DP2-OD002989), Packard award in Science and Engineering, Sparc Grant from the Broad Institute.

8.3 Graduate Funding

We thank the HHMI International Student Fellowship, the Martino's Centre for the Advanced Neuroimaging Training Grant and the "La Caixa" Graduate Fellowship for all graduate funding.

8.4 Zebrafish Husbandry and Lines

All zebrafish used in these studies were raised and maintained in the Koch Institute Zebrafish Core Facility. We thank Dr. Adam Amsterdam for his oversight of the fish facility, and specifically of the transgenic lines used here, and we thank Tim Angellini for technical assistance in raising and maintaining the fish.

We thank A. Schier and I. Woods (Harvard University) for the fluorescent lateral neuron line; C. Chien (University of Utah) for the line (*robo2*^{*ti272z/ti272z*} with *Tg(pou4f3:gap43GFP)s356t*); and S.

Johnson (Washington University at St. Louis) and R. Jain and M. Granato (University of Pennsylvania) for the fluorescent Mauthner line *Et(tol2:GFP) j1282b*.

8.5 Other Authors Contributions

The author performed all the novel work presented in this thesis either by himself or in collaboration with other graduate students in the “High-throughput Neurotechnology Group” at the RLE at MIT. For completeness I here include the collaborators in this work and their contributions to the thesis:

- Dr. Mehmet Fatih Yanik – supervised all work in this thesis
- Dr. Carolina Whalby – supervised the work related to the rapid optical projection tomography
- Dr. Peter Eimon – supervised zebrafish work of Chapter VI and performed part of the teratogen screen.
- Mr. Steven Wasserman – supervised and advised on the fabrication of the vertebrate automated screening platform.
- Dr. Tsung-Yao Chang – equally contributing author in papers related to Chapter III and IV. He designed the distal detection system for the zebrafish larvae and the loading nozzle for the zebrafish. He also put together the pipelining system described in Chapter IV.
- Dr. Amin Allalou – wrote ~50% of the code designed to correct for the vibrations and movement of the larvae in the capillary and the code related to 3D detection of single cells. He also designed the COR correction algorithms.

References

- Abraham, V. C., D. L. Taylor and J. R. Haskins (2004). "High content screening applied to large-scale cell biology." Trends Biotechnol **22**(1): 15-22.
- Allenby, G., M. T. Bocquel, M. Saunders, S. Kazmer, J. Speck, M. Rosenberger, A. Lovey, P. Kastner, J. F. Grippo, P. Chambon and et al. (1993). "Retinoic acid receptors and retinoid X receptors: interactions with endogenous retinoic acids." Proc Natl Acad Sci U S A **90**(1): 30-34.
- Amsterdam, A., S. Burgess, G. Golling, W. Chen, Z. Sun, K. Townsend, S. Farrington, M. Haldi and N. Hopkins (1999). "A large-scale insertional mutagenesis screen in zebrafish." Genes Dev **13**(20): 2713-2724.
- Ando, H., T. Furuta, R. Y. Tsien and H. Okamoto (2001). "Photo-mediated gene activation using caged RNA/DNA in zebrafish embryos." Nature genetics **28**: 317-325.
- Ando, H., M. Kobayashi, T. Tsubokawa, K. Uyemura, T. Furuta and H. Okamoto (2005). "Lhx2 mediates the activity of Six3 in zebrafish forebrain growth." Developmental biology **287**: 456-468.
- Ando, R., H. Hama, M. Yamamoto-Hino, H. Mizuno and A. Miyawaki (2002). "An optical marker based on the UV-induced green-to-red photoconversion of a fluorescent protein." Proceedings of the National Academy of Sciences of the United States of America **99**: 12651-12656.
- Armstrong, J. L., C. P. Redfern and G. J. Veal (2005). "13-cis retinoic acid and isomerisation in paediatric oncology--is changing shape the key to success?" Biochem Pharmacol **69**(9): 1299-1306.
- Barut, B. A. and L. I. Zon (2000). "Realizing the potential of zebrafish as a model for human disease." Physiol Genomics **2**(2): 49-51.
- Bellipanni, G., T. Murakami, O. G. Doerre, P. Andermann and E. S. Weinberg (2000). "Expression of Otx homeodomain proteins induces cell aggregation in developing zebrafish embryos." Dev Biol **223**(2): 339-353.
- Benke, P. J. (1984). "The isotretinoin teratogen syndrome." JAMA **251**(24): 3267-3269.
- Bewersdorf, J., R. Pick and S. W. Hell (1998). "Multifocal multiphoton microscopy." Optics Letters **23**: 655-657.
- Bhatt, D. H., S. J. Otto, B. Depoister and J. R. Fetcho (2004). "Cyclic AMP-induced repair of zebrafish spinal circuits." Science **305**(5681): 254-258.
- Biron, D., S. Wasserman, J. H. Thomas, A. D. Samuel and P. Sengupta (2008). "An olfactory neuron responds stochastically to temperature and modulates *Caenorhabditis elegans* thermotactic behavior." Proc Natl Acad Sci U S A **105**(31): 11002-11007.

Breuninger, T., K. Greger and E. H. K. Stelzer (2007). "Lateral modulation boosts image quality in single plane illumination fluorescence microscopy." Optics letters **32**: 1938-1940.

Brown, B. H. and B. H. Brown (1999). Medical physics and biomedical engineering. Bristol ; Philadelphia, Institute of Physics Pub.

Bryson-Richardson, R. J. and P. D. Currie (2004). "Optical projection tomography for spatio-temporal analysis in the zebrafish." Zebrafish: 2nd Edition Cellular and Developmental Biology **76**: 37-+.

Buckley, C. E., P. Goldsmith and R. J. Franklin (2008). "Zebrafish myelination: a transparent model for remyelination?" Dis Model Mech **1**(4-5): 221-228.

Cachat, J., A. Stewart, E. Utterback, P. Hart, S. Gaikwad, K. Wong, E. Kyzar, N. Wu and A. V. Kalueff (2011). "Three-Dimensional Neurophenotyping of Adult Zebrafish Behavior." Plos One **6**(3).

Carvalho, R., J. de Sonnevile, O. W. Stockhammer, N. D. Savage, W. J. Veneman, T. H. Ottenhoff, R. P. Dirks, A. H. Meijer and H. P. Spaink (2011). "A high-throughput screen for tuberculosis progression." PLoS One **6**(2): e16779.

Chang, T.-Y., C. Pardo-Martin, A. Allalou, C. Wahlby and M. F. Yanik (2012). "Fully automated cellular-resolution vertebrate screening platform with parallel animal processing." Lab on a Chip.

Chen, J. K., J. Taipale, M. K. Cooper and P. A. Beachy (2002). "Inhibition of Hedgehog signaling by direct binding of cyclopamine to Smoothened." Genes & Development **16**(21): 2743-2748.

Cheng, K. C., X. Xin, D. P. Clark and P. La Riviere (2011). "Whole-animal imaging, gene function, and the Zebrafish Phenome Project." Curr Opin Genet Dev **21**(5): 620-629.

Chung, K., M. M. Crane and H. Lu (2008). "Automated on-chip rapid microscopy, phenotyping and sorting of *C. elegans*." Nat Methods **5**(7): 637-643.

Curran, K., J. a. Lister, G. R. Kunkel, A. Prendergast, D. M. Parichy and D. W. Raible (2010). "Interplay between Foxd3 and Mitf regulates cell fate plasticity in the zebrafish neural crest." Developmental biology **344**: 107-118.

Das, T., B. Payer, M. Cayouette and W. a. Harris (2003). "In vivo time-lapse imaging of cell divisions during neurogenesis in the developing zebrafish retina." Neuron **37**: 597-609.

Deiters, A., R. A. Garner, H. Lusic, J. M. Govan, M. Dush, N. M. Nascone-Yoder and J. a. Yoder (2010). "Photocaged Morpholino Oligomers for the Light-Regulation of Gene Function in Zebrafish and Xenopus Embryos." Journal of the American Chemical Society: 11000-11001.

Ding, Z., Y. Zhao, H. Ren, J. Nelson and Z. Chen (2002). "Real-time phase-resolved optical coherence tomography and optical Doppler tomography." Optics express **10**: 236-245.

Dmochowski, I. J. and X. Tang (2007). "Taking control of gene expression with light-activated oligonucleotides." Biotechniques **43**.

Driever, W., L. Solnica-Krezel, A. F. Schier, S. C. Neuhauss, J. Malicki, D. L. Stemple, D. Y. Stainier, F. Zwartkruis, S. Abdelilah, Z. Rangini, J. Belak and C. Boggs (1996). "A genetic screen for mutations affecting embryogenesis in zebrafish." Development **123**: 37-46.

Duda, R. O. and P. E. Hart (1972). "Use of the Hough transformation to detect lines and curves in pictures." Communications of the ACM **15**(1): 11-15.

Duester, G. (2008). "Retinoic acid synthesis and signaling during early organogenesis." Cell **134**(6): 921-931.

Ekker, S. C., A. M. Petzold, V. M. Bedell, N. J. Boczek, J. J. Essner, D. Balciunas and K. J. Clark (2010). "SCORE Imaging: Specimen in a Corrected Optical Rotational Enclosure." Zebrafish **7**(2): 149-154.

Enejder, A., C. Brackmann and F. Svedberg (2010). "Coherent Anti-Stokes Raman Scattering Microscopy of Cellular Lipid Storage." IEEE Journal of Selected Topics in Quantum Electronics **16**: 506-515.

Fercher, A. and J. Briers (1981). "Flow visualization by means of single- exposure speckle photography." Optics communications **37**: 326-330.

Fisher, R. A. (1936). "The use of multiple measurements in taxonomic problems." Annals of Human Genetics **7**(2): 179-188.

Fricke, C., J.-s. Lee, S. Geiger-rudolph, F. Bonhoeffer and C.-b. Chien (2001). "Homolog Required for Retinal Axon Guidance." Science **292**: 507-510.

Fuchs, E., J. Jaffe, R. Long and F. Azam (2002). "Thin laser light sheet microscope for microbial oceanography." Optics express **10**: 145-154.

Fujii, H., T. Sato, S. Kaneko, O. Gotoh, Y. Fujii-Kuriyama, K. Osawa, S. Kato and H. Hamada (1997). "Metabolic inactivation of retinoic acid by a novel P450 differentially expressed in developing mouse embryos." EMBO J **16**(14): 4163-4173.

Funfak, A., A. Brösing, M. Brand and J. M. Köhler (2007). "Micro fluid segment technique for screening and development studies on Danio rerio embryos." Lab on a Chip **7**(9): 1132.

Gabel, C. V., F. Antoine, C. F. Chuang, A. D. Samuel and C. Chang (2008). "Distinct cellular and molecular mechanisms mediate initial axon development and adult-stage axon regeneration in *C. elegans*." Development **135**(6): 1129-1136.

Gehrig, J., M. Reischl, E. Kalmar, M. Ferg, Y. Hadzhiev, A. Zaucker, C. Song, S. Schindler, U. Liebel and F. Muller (2009). "Automated high-throughput mapping of promoter-enhancer interactions in zebrafish embryos." Nat Methods **6**(12): 911-916.

Goldstein, A. M. and M. C. Fishman (1998). "Notochord regulates cardiac lineage in zebrafish embryos." Dev Biol **201**(2): 247-252.

Gomaa, M. S., C. E. Bridgens, G. J. Veal, C. P. Redfern, A. Brancale, J. L. Armstrong and C. Simons (2011). "Synthesis and biological evaluation of 3-(1H-imidazol- and triazol-1-yl)-2,2-dimethyl-3-[4-(naphthalen-2-ylamino)phenyl]propyl derivatives as small molecule inhibitors of retinoic acid 4-hydroxylase (CYP26)." J Med Chem **54**(19): 6803-6811.

Graf, S. F., S. Hotzel, U. Liebel, A. Stemmer and H. F. Knapp (2011). "Image-based fluidic sorting system for automated Zebrafish egg sorting into multiwell plates." J Lab Autom **16**(2): 105-111.

Guizar-Sicairos, M., S. T. Thurman and J. R. Fienup (2008). "Efficient subpixel image registration algorithms." Optics letters **33**(2): 156-158.

Guo, S. X., F. Bourgeois, T. Chokshi, N. J. Durr, M. A. Hilliard, N. Chronis and A. Ben-Yakar (2008). "Femtosecond laser nanoaxotomy lab-on-a-chip for in vivo nerve regeneration studies." Nat Methods **5**(6): 531-533.

Haas, K., W. C. Sin, A. Javaherian, Z. Li and H. T. Cline (2001). "Single-cell electroporation for gene transfer in vivo." Neuron **29**(3): 583-591.

Haffter, P., M. Granato, M. Brand, M. C. Mullins, M. Hammerschmidt, D. A. Kane, J. Odenthal, F. J. van Eeden, Y. J. Jiang, C. P. Heisenberg, R. N. Kelsh, M. Furutani-Seiki, E. Vogelsang, D. Beuchle, U. Schach, C. Fabian and C. Nusslein-Volhard (1996). "The identification of genes with unique and essential functions in the development of the zebrafish, *Danio rerio*." Development **123**: 1-36.

Halloran, M. C., M. Sato-Maeda, J. T. Warren, F. Su, Z. Lele, P. H. Krone, J. Y. Kuwada and W. Shoji (2000). "Laser-induced gene expression in specific cells of transgenic zebrafish." Development **127**: 1953-1960.

Hammarlund, M., P. Nix, L. Hauth, E. M. Jorgensen and M. Bastiani (2009). "Axon regeneration requires a conserved MAP kinase pathway." Science **323**(5915): 802-806.

Hellerer, T., C. Axäng, C. Brackmann, P. Hillertz, M. Pilon and A. Enejder (2007). "Monitoring of lipid storage in *Caenorhabditis elegans* using coherent anti-Stokes Raman scattering (CARS) microscopy." Proceedings of the National Academy of Sciences of the United States of America **104**: 14658-14663.

Hernandez, P. P., V. Moreno, F. A. Olivari and M. L. Allende (2006). "Sub-lethal concentrations of waterborne copper are toxic to lateral line neuromasts in zebrafish (*Danio rerio*)." Hear Res **213**(1-2): 1-10.

Hernandez, R. E., A. P. Putzke, J. P. Myers, L. Margaretha and C. B. Moens (2007). "Cyp26 enzymes generate the retinoic acid response pattern necessary for hindbrain development." Development **134**(1): 177-187.

Höltkä-Vuori, M., V. T. V. Salo, L. Nyberg, C. Brackmann, A. Enejder, P. Panula and E. Ikonen (2010). "Zebrafish: gaining popularity in lipid research." The Biochemical journal **429**: 235-242.

Howe, D. G., Y. M. Bradford, T. Conlin, A. E. Eagle, D. Fashena, K. Frazer, J. Knight, P. Mani, R. Martin, S. A. Moxon, H. Paddock, C. Pich, S. Ramachandran, B. J. Ruef, L. Ruzicka, K. Schaper, X. Shao, A. Singer, B. Sprunger, C. E. Van Slyke and M. Westerfield (2013). "ZFIN, the Zebrafish Model Organism Database: increased support for mutants and transgenics." Nucleic Acids Res **41**(D1): D854-860.

Huang, H. B., D. Sun, J. K. Mills and S. H. Cheng (2009). "Robotic Cell Injection System With Position and Force Control: Toward Automatic Batch Biomanipulation." IEEE Transactions on Robotics **25**: 727-737.

Hudson, H. M. and R. S. Larkin (1994). "Accelerated image reconstruction using ordered subsets of projection data." IEEE Trans Med Imaging **13**(4): 601-609.

Huiskens, J., J. Swoger, F. Del Bene, J. Wittbrodt and E. H. K. Stelzer (2004). "Optical sectioning deep inside live embryos by selective plane illumination microscopy." Science **305**(5686): 1007-1009.

Hulme, S. E., S. S. Shevkoplyas, J. Apfeld, W. Fontana and G. M. Whitesides (2007). "A microfabricated array of clamps for immobilizing and imaging *C. elegans*." Lab Chip **7**(11): 1515-1523.

Hwang, H. and H. Lu (2012). "Microfluidic tools for developmental studies of small model organisms –nematodes, fruit flies, and zebrafish." Biotechnology Journal: n/a-n/a.

Hyatt, T. M. and S. C. Ekker (1999). "Vectors and techniques for ectopic gene expression in zebrafish." Methods Cell Biol **59**: 117-126.

Iftimia, N. V., D. X. Hammer, R. D. Ferguson, M. Mujat, D. Vu and A. a. Ferrante (2008). "Dual-beam Fourier domain optical Doppler tomography of zebrafish." Optics express **16**: 13624-13636.

Jesuthasan, S. and S. Subburaju (2002). "Gene transfer into zebrafish by sperm nuclear transplantation." Dev Biol **242**(2): 88-95.

Ji, N., J. C. Magee and E. Betzig (2008). "High-speed, low-photodamage nonlinear imaging using passive pulse splitters." Nature Methods **5**(2): 197-202.

Johnston, B. D., T. M. Scown, J. Moger, S. a. Cumberland, M. Baalousha, K. Linge, R. van Aerle, K. Jarvis, J. R. Lead and C. R. Tyler (2010). "Bioavailability of nanoscale metal oxides TiO₂, CeO₂, and ZnO to fish." Environmental science & technology **44**: 1144-1151.

Jontes, J. D., J. Buchanan and S. J. Smith (2000). "Growth cone and dendrite dynamics in zebrafish embryos: early events in synaptogenesis imaged in vivo." Nature neuroscience **3**: 231-237.

Juskaitis, R., T. Wilson, M. A. A. Neil and M. Kozubek (1996). "Efficient real-time confocal microscopy with white light sources." Nature **383**(6603): 804-806.

Kari, G., U. Rodeck and A. P. Dicker (2007). "Zebrafish: an emerging model system for human disease and drug discovery." Clin Pharmacol Ther **82**(1): 70-80.

Karlsson, J., J. von Hofsten and P.-E. Olsson (2001). "Generating Transparent Zebrafish: A Refined Method to Improve Detection of Gene Expression During Embryonic Development." Marine Biotechnology **3**(6): 0522-0527.

Kawakami, K., A. Shima and N. Kawakami (2000). "Identification of a functional transposase of the Tol2 element, an Ac-like element from the Japanese medaka fish, and its transposition in the zebrafish germ lineage." Proc Natl Acad Sci U S A **97**(21): 11403-11408.

Keller, P. J., A. D. Schmidt, A. Santella, K. Khairy, Z. Bao, J. Wittbrodt and E. H. K. Stelzer (2010). "Fast, high-contrast imaging of animal development with scanned light sheet-based structured-illumination microscopy." Nature Methods **7**: 637-642.

Keller, P. J., A. D. Schmidt, J. Wittbrodt and E. H. K. Stelzer (2008). "Reconstruction of Zebrafish Early Embryonic Development by Scanned Light Sheet Microscopy." Science **322**(5904): 1065-1069.

Kim, S., N. A. Zaghloul, E. Bubenshchikova, E. C. Oh, S. Rankin, N. Katsanis, T. Obara and L. Tsiokas (2011). "Nde1-mediated inhibition of ciliogenesis affects cell cycle re-entry." Nat Cell Biol **13**(4): 351-360.

Kimmel, C. B., W. W. Ballard, S. R. Kimmel, B. Ullmann and T. F. Schilling (1995). "Stages of embryonic development of the zebrafish." Developmental dynamics **203**: 253-310.

Kimmel, C. B., C. T. Miller and C. B. Moens (2001). "Specification and morphogenesis of the zebrafish larval head skeleton." Dev Biol **233**(2): 239-257.

Kimura, Y. (2004). "Interhemispheric difference in emotional response without awareness." Physiology & Behavior **82**(4): 727-731.

Knight, R. D. and T. F. Schilling (2006). "Cranial neural crest and development of the head skeleton." Adv Exp Med Biol **589**: 120-133.

Kokel, D., J. Bryan, C. Laggner, R. White, C. Y. Cheung, R. Mateus, D. Healey, S. Kim, A. A. Werdich, S. J. Haggarty, C. A. Macrae, B. Shoichet and R. T. Peterson (2010). "Rapid behavior-based identification of neuroactive small molecules in the zebrafish." Nat Chem Biol **6**(3): 231-237.

Lange, K. and R. Carson (1984). "EM reconstruction algorithms for emission and transmission tomography." J Comput Assist Tomogr **8**(2): 306-316.

Lewis, J. P. (1995). "Fast Template Matching." Vision Interface: 120-123.

Li, J., J. a. Mack, M. Souren, E. Yaksi, S.-i. Higashijima, M. Mione, J. R. Fetcho and R. W. Friedrich (2005). "Early development of functional spatial maps in the zebrafish olfactory bulb." The Journal of neuroscience : the official journal of the Society for Neuroscience **25**: 5784-5795.

Lieschke, G. J. and P. D. Currie (2007). "Animal models of human disease: zebrafish swim into view." Nature Reviews Genetics **8**(5): 353-367.

Liu, K. S. and J. R. Fetcho (1999). "Laser ablations reveal functional relationships of segmental hindbrain neurons in zebrafish." Neuron **23**: 325-335.

Lu, Z., P. C. Y. Chen, J. Nam, R. Ge and W. Lin (2007). "A micromanipulation system with dynamic force-feedback for automatic batch microinjection." Journal of Micromechanics and Microengineering **17**(2): 314-321.

Manzini, M. C., D. E. Tambunan, R. S. Hill, T. W. Yu, T. M. Maynard, E. L. Heinzen, K. V. Shianna, C. R. Stevens, J. N. Partlow, B. J. Barry, J. Rodriguez, V. A. Gupta, A. K. Al-Qudah, W. M. Eyaid, J. M. Friedman, M. A. Salih, R. Clark, I. Moroni, M. Mora, A. H. Beggs, S. B. Gabriel and C. A. Walsh (2012). "Exome sequencing and functional validation in zebrafish identify GTDC2 mutations as a cause of Walker-Warburg syndrome." Am J Hum Genet **91**(3): 541-547.

Mark, M., N. B. Ghyselinck and P. Chambon (2006). "Function of retinoid nuclear receptors. Lessons from genetic and pharmacological dissections of the retinoic acid signaling pathway during mouse embryogenesis." Annual Review of Pharmacology and Toxicology **46**: 451-480.

Mauch, C. P., H.-u. Dodt, U. Leischner, A. Schierloh, N. Ja, K. Becker, K. Deininger, J. M. Deussing, M. Eder and W. Zieglga (2007). "Ultramicroscopy : three-dimensional visualization of neuronal networks in the whole mouse brain." Nature Methods **4**: 331-336.

McGrath, P. and C. Li (2008). "Zebrafish: a predictive model for assessing drug-induced toxicity." Drug Discovery Today **13**(9-10): 394-401.

Mckinney, S. A., C. S. Murphy, K. L. Hazelwood, M. W. Davidson and L. L. Looger (2009). "BRIEF COMMUNICATIONS A bright and photostable photoconvertible fluorescent protein." Nature Methods **6**: 131-133.

McLean, D. L. and J. R. Fetcho (2008). "Using imaging and genetics in zebrafish to study developing spinal circuits in vivo." Developmental neurobiology **68**: 817-834.

Meeker, N. D. and N. S. Trede (2008). "Immunology and zebrafish: spawning new models of human disease." Dev Comp Immunol **32**(7): 745-757.

Menegola, E., M. L. Broccia, F. Di Renzo and E. Giavini (2006). "Postulated pathogenic pathway in triazole fungicide induced dysmorphogenic effects." Reproductive Toxicology **22**(2): 186-195.

Milan, D. J. and C. A. Macrae (2008). "Zebrafish genetic models for arrhythmia." Prog Biophys Mol Biol **98**(2-3): 301-308.

Mochida, G. H., V. S. Ganesh, M. I. de Michelena, H. Dias, K. D. Atabay, K. L. Kathrein, H. T. Huang, R. S. Hill, J. M. Felie, D. Rakiec, D. Gleason, A. D. Hill, A. N. Malik, B. J. Barry, J. N. Partlow, W. H. Tan, L. J. Glader, A. J. Barkovich, W. B. Dobyns, L. I. Zon and C. A. Walsh (2012). "CHMP1A encodes an essential regulator of BMI1-INK4A in cerebellar development." Nat Genet **44**(11): 1260-1264.

Nasevicius, A. and S. C. Ekker (2000). "Effective targeted gene 'knockdown' in zebrafish." Nat Genet **26**(2): 216-220.

Neil, M. A. A., R. Juskaitis and T. Wilson (1997). "Method of obtaining optical sectioning by using structured light in a conventional microscope." Optics Letters **22**(24): 1905-1907.

Neveu, P., I. Aujard, C. Benbrahim, T. Le Saux, J.-F. Allemand, S. Vriz, D. Bensimon and L. Jullien (2008). "A caged retinoic acid for one- and two-photon excitation in zebrafish embryos." Angewandte Chemie (International ed. in English) **47**: 3744-3746.

Niell, C. M. and S. J. Smith (2005). "Functional imaging reveals rapid development of visual response properties in the zebrafish tectum." Neuron **45**(6): 941-951.

Nishimura, N., C. B. Schaffer, B. Friedman, P. S. Tsai, P. D. Lyden and D. Kleinfeld (2006). "Targeted insult to subsurface cortical blood vessels using ultrashort laser pulses: three models of stroke." Nature Methods **3**(2): 99-108.

Ntziachristos, V. (2010). "Going deeper than microscopy: the optical imaging frontier in biology." Nature Methods **7**(8): 603-614.

O'Brien, G. S., S. Rieger, S. M. Martin, A. M. Cavanaugh, C. Portera-Cailliau and A. Sagasti (2009). "Two-photon axotomy and time-lapse confocal imaging in live zebrafish embryos." Journal of visualized experiments : JoVE.

Olivier, N., M. a. Luengo-Oroz, L. Duloquin, E. Faure, T. Savy, I. Veilleux, X. Solinas, D. Debarre, P. Bourguine, a. Santos, N. Peyrieras and E. Beaurepaire (2010). "Cell Lineage Reconstruction of Early Zebrafish Embryos Using Label-Free Nonlinear Microscopy." Science **329**: 967-971.

Ouyang, X., I. a. Shestopalov, S. Sinha, G. Zheng, C. L. W. Pitt, W.-H. Li, A. J. Olson and J. K. Chen (2009). "Versatile synthesis and rational design of caged morpholinos." Journal of the American Chemical Society **131**: 13255-13269.

Pardo-Martin, C., T. Y. Chang, B. K. Koo, C. L. Gilleland, S. C. Wasserman and M. F. Yanik (2010). "High-throughput in vivo vertebrate screening." Nat Methods **7**(8): 634-636.

Parng, C., N. M. Roy, C. Ton, Y. Lin and P. McGrath (2007). "Neurotoxicity assessment using zebrafish." Journal of pharmacological and toxicological methods **55**: 103-112.

Peterson, R. T., S. Y. Shaw, T. A. Peterson, D. J. Milan, T. P. Zhong, S. L. Schreiber, C. A. MacRae and M. C. Fishman (2004). "Chemical suppression of a genetic mutation in a zebrafish model of aortic coarctation." Nature Biotechnology **22**(5): 595-599.

Petzold, A. M., V. M. Bedell, N. J. Boczek, J. J. Essner, D. Balciunas, K. J. Clark and S. C. Ekker (2010). "SCORE imaging: specimen in a corrected optical rotational enclosure." Zebrafish **7**: 149-154.

Pham, D. L., C. Xu and J. L. Prince (2000). "Current methods in medical image segmentation." Annual Review of Biomedical Engineering, Vol 13 **2**: 315-337.

Pisharath, H., J. M. Rhee, M. a. Swanson, S. D. Leach and M. J. Parsons (2007). "Targeted ablation of beta cells in the embryonic zebrafish pancreas using E. coli nitroreductase." Mechanisms of development **124**: 218-229.

Rihel, J., D. A. Prober, A. Arvanites, K. Lam, S. Zimmerman, S. Jang, S. J. Haggarty, D. Kokel, L. L. Rubin, R. T. Peterson and A. F. Schier (2010). "Zebrafish behavioral profiling links drugs to biological targets and rest/wake regulation." Science **327**(5963): 348-351.

Roeser, T. and H. Baier (2003). "Visuomotor behaviors in larval zebrafish after GFP-guided laser ablation of the optic tectum." The Journal of neuroscience **23**: 3726-3734.

Rohde, C. B., F. Zeng, R. Gonzalez-Rubio, M. Angel and M. F. Yanik (2007). "Microfluidic system for on-chip high-throughput whole-animal sorting and screening at subcellular resolution." Proc Natl Acad Sci U S A **104**(35): 13891-13895.

Rubinstein, A. L. (2003). "Zebrafish: from disease modeling to drug discovery." Curr Opin Drug Discov Devel **6**(2): 218-223.

Sato, T., M. Takahoko and H. Okamoto (2006). "HuC:Kaede, a useful tool to label neural morphologies in networks in vivo." Genesis (New York, N.Y. : 2000) **44**: 136-142.

Schilling, T. F. and C. B. Kimmel (1994). "Segment and cell type lineage restrictions during pharyngeal arch development in the zebrafish embryo." Development **120**(3): 483-494.

Schilling, T. F. and C. B. Kimmel (1997). "Musculoskeletal patterning in the pharyngeal segments of the zebrafish embryo." Development **124**(15): 2945-2960.

Schroeder, M. and C. C. Zouboulis (2007). "All-trans-retinoic acid and 13-cis-retinoic acid: pharmacokinetics and biological activity in different cell culture models of human keratinocytes." Horm Metab Res **39**(2): 136-140.

Serbedzija, G. N., J. N. Chen and M. C. Fishman (1998). "Regulation in the heart field of zebrafish." Development **125**: 1095-1101.

Sharpe, J., U. Ahlgren, P. Perry, B. Hill, A. Ross, J. Hecksher-Sorensen, R. Baldock and D. Davidson (2002). "Optical projection tomography as a tool for 3D microscopy and gene expression studies." Science **296**(5567): 541-545.

Shen, Y.-c., D. Li, A. Al-Shoaibi, T. Bersano-Begey, H. Chen, S. Ali, B. Flak, C. Perrin, M. Winslow, H. Shah, P. Ramamurthy, R. H. Schmedlen, S. Takayama and K. F. Barald (2009). "A student team in a University of Michigan biomedical engineering design course constructs a microfluidic bioreactor for studies of zebrafish development." Zebrafish **6**: 201-213.

Shestopalov, I. a., S. Sinha and J. K. Chen (2007). "Light-controlled gene silencing in zebrafish embryos." Nature chemical biology **3**: 650-651.

Shin, J. T. and M. C. Fishman (2002). "From Zebrafish to human: modular medical models." Annu Rev Genomics Hum Genet **3**: 311-340.

Singh, K. K., G. De Rienzo, L. Drane, Y. Mao, Z. Flood, J. Madison, M. Ferreira, S. Bergen, C. King, P. Sklar, H. Sive and L. H. Tsai (2011). "Common DISC1 polymorphisms disrupt Wnt/GSK3beta signaling and brain development." Neuron **72**(4): 545-558.

Steinmeyer, J. D., C. L. Gilleland, C. Pardo-Martin, M. Angel, C. B. Rohde, M. A. Scott and M. F. Yanik (2010). "Construction of a femtosecond laser microsurgery system." Nat Protoc **5**(3): 395-407.

Supatto, W. (2005). "In vivo modulation of morphogenetic movements in Drosophila embryos with femtosecond laser pulses." Proceedings of the National Academy of Sciences **102**(4): 1047-1052.

Tamplin, O. J. and L. I. Zon (2010). "Fishing at the cellular level." Nature Methods **7**(8): 600-601.

Tang, X., S. Maegawa, E. S. Weinberg and I. J. Dmochowski (2007). "Regulating gene expression in zebrafish embryos using light-activated, negatively charged peptide nucleic acids." Journal of the American Chemical Society **129**: 11000-11001.

Theodosiou, M., V. Laudet and M. Schubert (2010). "From carrot to clinic: an overview of the retinoic acid signaling pathway." Cell Mol Life Sci **67**(9): 1423-1445.

Thermes, V., C. Grabher, F. Ristoratore, F. Bourrat, A. Choulika, J. Wittbrodt and J. S. Joly (2002). "I-SceI meganuclease mediates highly efficient transgenesis in fish." Mech Dev **118**(1-2): 91-98.

Tomasini, A. J., A. D. Schuler, J. a. Zebala and A. N. Mayer (2009). "PhotoMorphs: a novel light-activated reagent for controlling gene expression in zebrafish." Genesis (New York, N.Y. : 2000) **47**: 736-743.

Ton, C. and C. Parng (2005). "The use of zebrafish for assessing ototoxic and otoprotective agents." Hear Res **208**(1-2): 79-88.

Tran, T. C., B. Sneed, J. Haider, D. Blavo, A. White, T. Aiyejorun, T. C. Baranowski, A. L. Rubinstein, T. N. Doan, R. Dingleline and E. M. Sandberg (2007). "Automated, quantitative screening assay for antiangiogenic compounds using transgenic zebrafish." Cancer Res **67**(23): 11386-11392.

Tropepe, V. and H. L. Sive (2003). "Can zebrafish be used as a model to study the neurodevelopmental causes of autism?" Genes Brain Behav **2**(5): 268-281.

Vennemann, P., R. Lindken and J. Westerweel (2007). "In vivo whole-field blood velocity measurement techniques." Experiments in fluids **42**: 495-511.

Vogel, A., J. Noack, G. Huttman and G. Paltauf (2005). "Mechanisms of femtosecond laser nanosurgery of cells and tissues." Applied Physics B-Lasers and Optics **81**(8): 1015-1047.

Voie, A. H., D. H. Burns and F. A. Spelman (1993). "Orthogonal-plane fluorescence optical sectioning: three-dimensional imaging of macroscopic biological specimens." J Microsc **170**(Pt 3): 229-236.

Walls, J. R., J. G. Sled, J. Sharpe and R. M. Henkelman (2005). "Correction of artefacts in optical projection tomography." Physics in medicine and biology **50**(19): 4645.

Wang, W., X. Liu, D. Gelinas, B. Ciruna and Y. Sun (2007). "A fully automated robotic system for microinjection of zebrafish embryos." PLoS ONE **2**(9): e862.

Wen, L., W. Wei, W. Gu, P. Huang, X. Ren, Z. Zhang, Z. Zhu, S. Lin and B. Zhang (2008). "Visualization of monoaminergic neurons and neurotoxicity of MPTP in live transgenic zebrafish." Developmental Biology **314**(1): 84-92.

Wienholds, E., S. Schulte-Merker, B. Walderich and R. H. Plasterk (2002). "Target-selected inactivation of the zebrafish rag1 gene." Science **297**(5578): 99-102.

Wu, Y., J. E. Ferguson, 3rd, H. Wang, R. Kelley, R. Ren, H. McDonough, J. Meeker, P. C. Charles and C. Patterson (2008). "PRDM6 is enriched in vascular precursors during development and inhibits endothelial cell proliferation, survival, and differentiation." J Mol Cell Cardiol **44**(1): 47-58.

Xiao, T., T. Roeser, W. Staub and H. Baier (2005). "A GFP-based genetic screen reveals mutations that disrupt the architecture of the zebrafish retinotectal projection." Development **132**(13): 2955-2967.

Yaksi, E., B. Judkewitz and R. W. Friedrich (2007). "Topological reorganization of odor representations in the olfactory bulb." PLoS biology **5**: e178.

Yang, C.-T., R. D. Sengemann and S. L. Johnson (2004). "Larval melanocyte regeneration following laser ablation in zebrafish." The Journal of investigative dermatology **123**: 924-929.

Yanik, M. F., H. Cinar, H. N. Cinar, A. D. Chisholm, Y. Jin and A. Ben-Yakar (2004). "Neurosurgery: functional regeneration after laser axotomy." Nature **432**(7019): 822.

Yanik, M. F., H. Cinar, H. N. Cinar, A. Gibby, A. D. Chisholm, Y. S. Jin and A. Ben-Yakar (2006). "Nerve regeneration in *Caenorhabditis elegans* after femtosecond laser axotomy." Ieee Journal of Selected Topics in Quantum Electronics **12**(6): 1283-1291.

Yashiro, K., X. Zhao, M. Uehara, K. Yamashita, M. Nishijima, J. Nishino, Y. Saijoh, Y. Sakai and H. Hamada (2004). "Regulation of retinoic acid distribution is required for proximodistal patterning and outgrowth of the developing mouse limb." Dev Cell **6**(3): 411-422.

Young, D. L., R. A. Schneider, D. Hu and J. A. Helms (2000). "Genetic and teratogenic approaches to craniofacial development." Crit Rev Oral Biol Med **11**(3): 304-317.

Zeng, F., C. B. Rohde and M. F. Yanik (2008). "Sub-cellular precision on-chip small-animal immobilization, multi-photon imaging and femtosecond-laser manipulation." Lab Chip **8**(5): 653-656.

Zhang, M., S. H. Chung, C. Fang-Yen, C. Craig, R. A. Kerr, H. Suzuki, A. D. Samuel, E. Mazur and W. R. Schafer (2008). "A self-regulating feed-forward circuit controlling *C. elegans* egg-laying behavior." Curr Biol **18**(19): 1445-1455.

Ziouzenkova, O. and J. Plutzky (2008). "Retinoid metabolism and nuclear receptor responses: New insights into coordinated regulation of the PPAR-RXR complex." FEBS Lett **582**(1): 32-38.

Zon, L. I. and R. T. Peterson (2005). "In vivo drug discovery in the zebrafish." Nat Rev Drug Discov **4**(1): 35-44.

Zottoli, S. J. and D. S. Faber (2000). "The Mauthner Cell : What Has It Taught Us?" The Neuroscientist **6**: 26-38.

Zumbusch, A., G. Holtom and X. Xie (1999). "Three-Dimensional Vibrational Imaging by Coherent Anti-Stokes Raman Scattering." Physical Review Letters **82**: 4142-4145.

zur Nieden, N. I., L. A. Davis and D. E. Rancourt (2010). "Comparing three novel endpoints for developmental osteotoxicity in the embryonic stem cell test." Toxicol Appl Pharmacol **247**(2): 91-97.